Regina Seidl, BSc

Specimen Preparation for Transmission Electron Microscopy by Focused Ion Beam: Refinement of Post-Treatment using Focused Low Energy Argon Ion Milling

MASTER'S THESIS

to achieve the university degree of

Diplom-Ingenieurin

Master's degree programme: Advanced Materials Science

submitted to

Graz University of Technology

Supervisor

Ao. Univ.-Prof. Dipl.-Ing. Dr. techn. Werner Grogger

Institute of Electron Microscopy and Nanoanalysis

Graz, September 2016

AFFIDAVIT

I declare that I have authored this thesis independently, that I have not used other than the declared sources/resources, and that I have explicitly indicated all material which has been quoted either literally or by content from the sources used. The text document uploaded to TUGRAZonline is identical to the present master's thesis.

Date

Signature

Abstract

For high resolution transmission electron microscopy (HRTEM) investigations a thin and defect-free sample is required. Therefore, to reach atomic resolution high demands are placed on the TEM lamella preparation. The NanoMill® by Fischione Instruments gives the opportunity of a fast post focused ion beam (FIB) treatment by low energy argon ion milling, in which the sample surface can be cleaned, the FIB induced preparation artefacts be removed to a large extent, and - for longer process times - the total sample thickness be reduced.

The main goal of this thesis is the determination of the sputter rate of two different materials. Another important aspect of the thesis is the consideration of the geometrical conditions in the NanoMill® and the optimization of the grid geometry and the lamella position on the grid.

To determine the milling rate of silicon carbide and lead zirconate titanate an iterative experiment of thinning the respective TEM lamellae in the NanoMill® and the determination of their relative thickness with the t/λ method in the TEM have been performed. From this relative decrease in thickness the sputter rate can be derived. The theoretical calculation of the mean free path of the material leads to absolute thickness values, which have been compared with the absolute thickness measurement of the double cross section of the samples. Thus, an experimental mean free path determination was performed to verify the theoretical results.

Based on to the findings of this work an optimized post-treatment for FIB lamellae with the NanoMill® is possible.

Acknowledgement

First of all I would like to thank Professor Ferdinand Hofer, head of our institute, for offering the possibility to write this thesis and the Austrian Research Promotion Agency FFG (project 850220) for funding.

I would also like to thank Professor Werner Grogger for being my supervisor, for his cooperation and his advices.

My deepest appreciation goes to Evelin Fisslthaler and Martina Dienstleder. Both of them were very committed to my work, but also supportive with personal discussions.

Besides that I would like to thank the whole FELMI-ZFE team for useful input for my work and their amusing distraction.

Last but not least, I would like to express my deep gratitude to my family. Their love and continuous encouragement make me into what I am.

Table of Contents

1. Introduction and Motivation 1
2. Fundamentals 2
   2.1. Transmission Electron Microscope (TEM) 2
   2.2. Sample Preparation 5
      2.2.1. Focused Ion Beam (FIB) 6
      2.2.2. Preparation steps TEM lamella 6
      2.2.3. Thinning with low voltage in the FIB Nova200 NanoLab and NanoMill® 7
   2.3. NanoMill® 9
   2.4. Sputtering 12
      2.4.1. Sputter conditions in NanoMill® 13
   2.5. Thickness measurement 14
      2.5.1. t/λ method 14
      2.5.2. Double Cross Section 19
3. Practical Work 21
   3.1. NanoMill® operation 22
      3.1.1. Load the sample 22
      3.1.2. Transferring the sample 23
      3.1.3. Tilt and Rotation 24
      3.1.4. Milling of the sample 25
      3.1.5. Astigmatism correction 27
      3.1.6. Assets and drawbacks 28
   3.2. Optimal Sample Position 32
   3.3. Backside milling 36
      3.3.1. Information related to lamella fixation for FIB backside milling 38
      3.3.2. Backside milling in NanoMill® 38
   3.4. Grid comparison 40
   3.5. Design of the optimal grid for a post-treatment with the NanoMill® 41
   3.6. CM20 operation 46

3.7. Analysis of the TEM images with Digital Micrograph 48
3.8. Materials 50
3.8.1. Silicon carbide 51
3.8.2. Lead zirconate titanate 68
4. Conclusion 75
Bibliography .... A

Abbreviations

CBED	convergent beam electron diffraction
CCD	charge-coupled device
DCS	double cross section
DM	Digital Micrograph
EELS	electron energy loss spectrum/spectroscopy
EFTEM	energy filtered TEM
keV	kilo electron volt
PZT	lead zirconate titanate
MFP	mean free path
ML	monolayer
mrad	milli radian
nm	nano meter
pA	pico ampere
PACBED	positioned averaged CBED
SED	secondary electron detector
TEM	transmission electron microscope/microscopy
VLM	visible-light microscope/microscopy

1. Introduction and Motivation

In materials science, the investigation with the TEM has become a standard method. However, the improvement of the used microscopes entails an improvement of the sample preparation. To reach atomic resolution the sample must not only be thin, but also free of any defects, this means that the sample is in such a pristine condition as possible. In the case of a FIB prepared TEM lamella the ion implantation and the amorphous layers are known artefacts. With an additional preparation step after the milling procedure in the FIB one can enhance the quality of the sample by using the NanoMill®. This equipment manufactured by Fischione Instruments uses low energy argon ions to clean the surface of the TEM lamella and to optimize sample thickness.

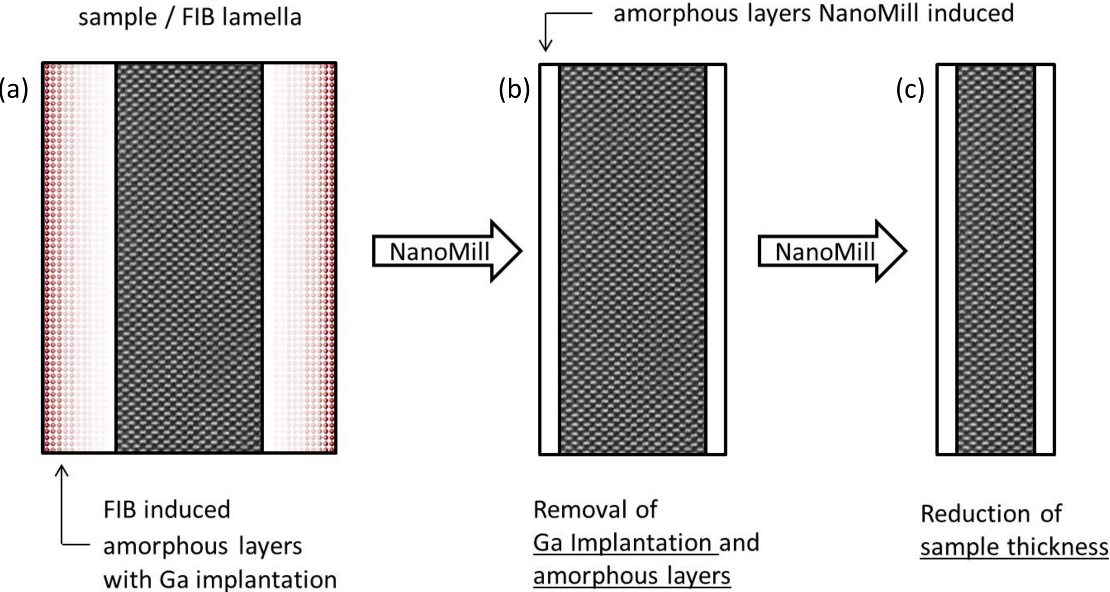

Figure 1-1: (a) shows the sketch of a FIB lamella with the known artefacts. By performing a post-treatment in the NanoMill® in the first step the Ga^+ implantation and the thickness of the amorphous layers can be reduced (b). Further milling, with low energy Ar^+ ions, will cause a thickness reduction of the sample. However, the FIB induced amorphous layers can be removed completely, if the sputter period is long enough, though by the sputter process in the NanoMill® new thinner amorphous layers are generated. This artefact will remain on both sides of the sample.

The aim of this work is to investigate the sputter behaviour of different materials, more precisely silicon carbide and lead zirconate titanate were examined. These materials are investigated within the Austrian Research Promotion Agency FFG (project 850220) and therefore to find a recipe for optimal TEM lamella post-treatments was the main goal of this thesis. This entails an iterative process of measuring the thickness of the samples and reducing the thickness in the NanoMill®. Furthermore, the optimal position of the lamella on the transfer grid as well as the best grid geometry were determined.

2. Fundamentals

2.1. Transmission Electron Microscope (TEM)

This chapter contains a brief summary of the fundamentals of TEM. In the following paragraphs an overview of the instrument, the microscope, as well as the technique and its advantages and limitations is given [1].

The historical reason for developing electron microscopy was the limitation in resolution of the visible-light microscope (VLM) by the wavelength of visible light (380 – 750 nm). By comparison, the used electrons have smaller wavelengths of about 0.001 - 0.004 nm, which lead to an enhancement of the resolution δ, which is defined as the smallest distance between two objects that can still be separated. The dependence of the wavelength on the resolution can be seen in the Raleigh-criterion for VLM [2, pp. 3–17]:

$$\delta = \frac{0.61\,\lambda}{\mu\ \sin\beta} \tag{2.1}$$

λ … wavelength
μ … refractive index
β … half angle of collection

In equation 2.1, λ is the wavelength of the radiation (photon, electron), μ is the refractive index of the medium, and β the half angle of collection. By using electrons, one can take advantage of the influence of the wavelength on the resolution and the subsequent benefit for microscopy. However, the half collection angle β will limit the resolution when employing electrons.

Transmission electron microscopy offers a broad range of characterization techniques, which allow the determination of the structure as well as the chemical composition of metals, alloys, ceramics, glasses, polymers, semiconductors, and combinations of these materials. To enable the examination, electron transparent samples must be extracted from the bulk material. How to prepare lamellae with thicknesses of a couple of hundred nanometres to tens of nanometres will be discussed in the next section. The examiner should keep in mind that very low sample thicknesses usually come along with difficulties. The sample is exposed to mechanical loads like the continual transfer into and out of the TEM or NanoMill® as well as internal stress, which can lead to bending or twisting of the sample and therefore causes a deviation from the ideal plane-parallel shape. This information can be crucial for the interpretation. Another factor, which can influence or even damage the sample is the electron beam itself. The investigation with the electron beam can lead to carbon contamination or for very sensitive samples it can completely destroy the original structure of the material. Beside the great variety of materials which can be examined, there are sensitive samples which must

undergo laborious preparation to fulfil the requirement of electron stability, or cannot be investigated in the TEM at all.

The interactions occurring between the electron beam and the material can be divided in elastic and inelastic processes. An overview can be seen in Figure 2-1 below.

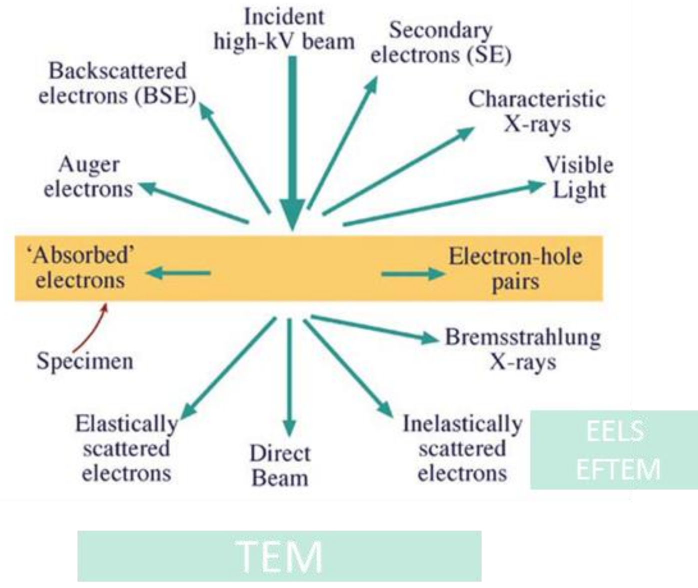

Figure 2-1: Signals generated by the interaction of electron beam and thin sample. Most of these signals can be detected in different operation modes of the TEM. The directions shown for each signal do not always represent the physical direction of the signal, but indicate, in a relative manner, where the signal is strongest or where it is detected. (modified from [2, p. 7])

Nearly all of these signals can be used for investigating the sample. Electron energy loss spectroscopy (EELS) and energy filtered transmission electron microscopy (EFTEM) are analytical methods used in this work.

An inelastic scattering event is accompanied by an energy loss of electrons. The amount of lost energy can be measured with an EEL spectrometer and shown in an EEL spectrum, which can be used for the analysis.

In EFTEM it is possible to use only electrons within a certain energy range for creating an image. Therefore, the electrons get split up according to their energies and an energy selecting slit is used to select the electrons with specific energy values. This method can be used to obtain a t/λ map as described in Chapter 2.5.1.

Though electron microscopy is based on the interaction of electrons with the FIB lamella also negative effects like dehydration, charge effects, destruction and contamination are possible. The nature of the sample, the acceleration voltage of the electron beam, as well as the size of the scanned window, respectively the amount of interacting electrons, influence the TEM observation induced artefacts. For each of these five artefact groups secondary thermal

damage can occur. Examples will be fusion, a change of solid-liquid physical state of a solid sample created by an increased temperature due to the electron bombardment, and amorphization, a partial or total degradation of chemical bonds of a crystalline sample.

2.2. Sample Preparation

The preparation of TEM samples is a complex and challenging field of work. The used procedures depend on the material properties, the available equipment, but also time constraints. In general, preliminary preparation techniques, ion based preparation techniques, mechanical preparation techniques and replica techniques can be distinguished. The intention of this chapter is to list some preparation methods with their respective artefacts and to describe the preparation technique used in the practical part of this work. Therefore, the lamella preparation by Focused Ion Beam technique in combination with a post-treatment by low energy argon ion milling will be described in detail.

It should be kept in mind that during every preparation procedure preparation induced defects [1, pp. 125–137] or sample damage can be generated on the sample surface due to mechanical, chemical, ionic and physical action. These imperfections result in observable artefacts in TEM images. A distinction between artefacts forming during the preliminary preparation or sample thinning step and those, which occur due to the observation with the electron beam, can be made. Mechanical preparation-induced artefacts like deformation, matter displacement, cracks and roughness arise due to sawing, mechanical grinding and polishing, dimpling and so on. Chemical preparation methods like electrolytic/chemical polishing and electrolytic/chemical thinning can lead to selective dissolution, composition change and structural change.

Since a distinction between original and preparation induced artefacts can be difficult, care must be taken to avoid the introduction of defects into the sample during the preparation process.

The use of ionic preparation, in particular the argon ion milling and FIB technique with gallium ions, can cause structural change, implantation and re-deposition. These artefacts will be a major issue of this work and discussed in detail in the following section.

The overall objective is to produce an electron transparent, plan parallel sample. Ideally the preparation damage should be kept to a minimum and the thickness of the amorphous material on both sides of the lamella should be vanishingly small. A summary of various artefacts formed by the preparation and during the TEM observation as well as secondary thermal damage can be seen in [1, p. 126] and in the Appendix.

2.2.1. Focused Ion Beam (FIB)

The focused ion beam technique [2, pp. 188–189],[3, pp. 135–151] has become a powerful method over the last years for producing sufficiently thin lamella. In this work the samples are prepared with a Nova 200 NanoLab by FEI. This instrument is equipped with a dual-beam system (shown in Figure 2-2) which combines an electron and an ion beam. The electron beam can be used for imaging. In the FIB column, which is installed at an angle of 38° relative to the SEM column, Ga^+ ions are generated and can be used for material removal as well as depositing different materials, using gas injection systems. Both the electron and the ion beam can be used to the observation of the preparation process. For the lamella preparation, the Nova 200 NanoLab is operated at energies from 30 keV down to 5 keV, which is the lowest possible energy. In state of the art FIB instruments a low voltage mode down to 500 V is a common equipment variant. Using low voltage cleaning leads to artefact minimization, in particular to thinner amorphous layers. However, because the minimal energy of the Nova 200 is 5keV, it is useful to perform an additional treatment with lower acceleration voltages using the NanoMill.

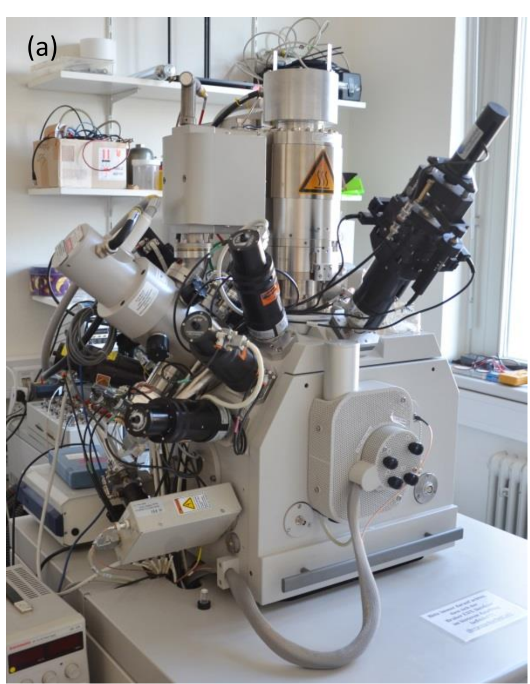

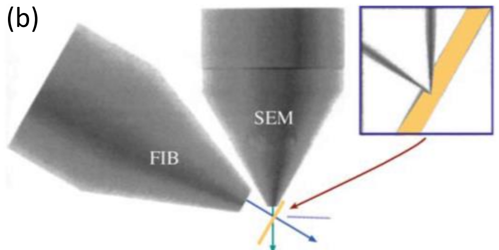

Figure 2-2: (a) Nova200 NanoLab at the Felmi. (b) Schematic of basic concept dual beam system (FIB and SEM). Image from [2, p. 188].

2.2.2. Preparation steps TEM lamella

In this section the steps (see Figure 2-3) of TEM lamella preparation are explained.

(a) Platinum is deposited either by ions or by electrons to protect the sample in the following process steps. Furthermore, it stabilizes the lamella and prevents it from bending or braking due to internal stress or mechanical loads like the transfer in and out the TEM or NanoMill®.

(b) In the next step two patterns for trench milling are placed at the desired locations. In the beginning a high voltage and a high current is used for a fast removal of material.

(c) To separate the lamella from the bulk material a so-called U-cut is necessary. Therefore, the sample must be tilted so that the sides and the bottom of the lamella can be cut free with the ion beam. Before the last intermediate piece is disconnected the micromanipulator is placed on the top of the lamella, and fixed by welding with platinum. The last connection can then be cut and the lamella lifted out (d), and transferred to the TEM lift-out grid and fixed with platinum on it (e). Now the micromanipulator is separated from the lamella. The last step (f) a low voltage and weak current cleaning step is used in order to flatten the lamella surface and to generate a lamella with 500-1000 nm thickness ready for the lift-out procedure. The lamella thinning to electron transparency is described in the next section in more detail.

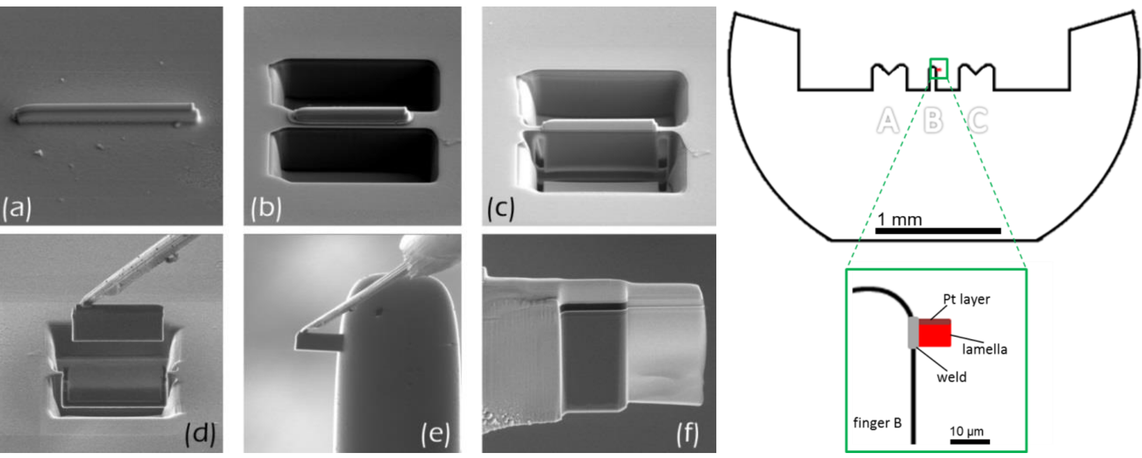

Figure 2-3: Preparation of TEM lamella by FIB milling. a) Pt protection layer, b) trench milling, c) U-cut: lamella separation from the bulk material, d) in-situ lift-out, e) fixation on the TEM transfer grid f) lamella after thinning to electron transparency.

Figure 2-4: This scheme shows a common TEM grid with a lamella in "flag-position".

2.2.3. Thinning with low voltage in the FIB Nova200 NanoLab and NanoMill®

The goal for HRTEM investigation is to produce a very thin lamella, ideally with constant thickness and in such a natural state as possible. After the standard preparation procedure, the last preparation step in the FIB is done with an acceleration voltage of 5 kV and a beam current of 70 pA and with a tilt angle of 5°. It should be noted, that the thinning process is influenced by the ion energy, angle of incidence, vacuum, initial surface topology, initial chemistry, initial orientation, initial crystallography of the surface, beam energy and beam profile [2, p. 179].

A disadvantage of this method is that ion milling with 'relatively' high (about 5 keV) acceleration voltage may cause structural changes including ion implantation, re-deposition and the formation of an amorphous layer.

The sample preparation concludes with the post-treatment in the NanoMill®. In this final thinning step (see Chapter 2.4.1), also referred to as 'cleaning', low energy (900 eV) Ar^+ ions are used for the milling process. This treatment can remove artefacts, or at least reduce them to create an enhanced sample quality for high-resolution investigations.

The already mentioned relation of the ion acceleration voltage on the depth of amorphization on the surface of the lamella can be seen in the diagram below.

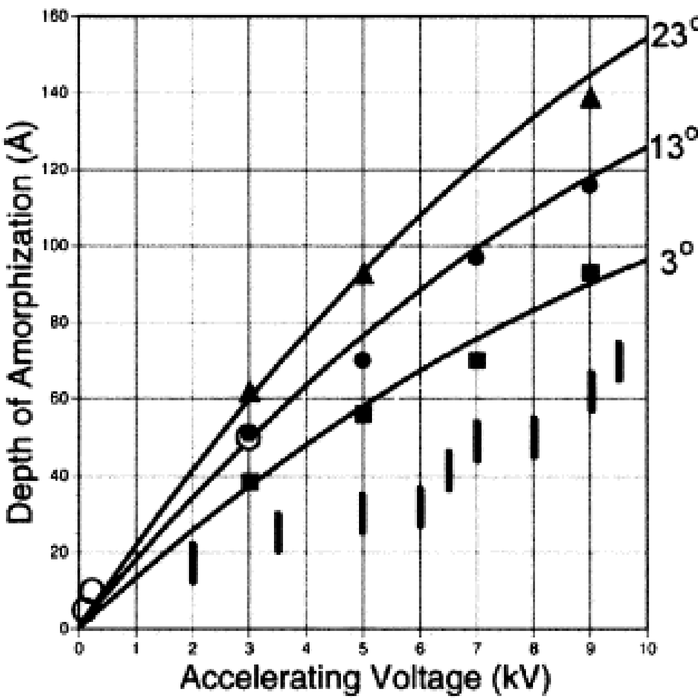

Figure 2-5: Experimental results of depth of amorphization in single-crystal silicon for different acceleration voltages of Ar^+ ions, at incident ion angles of 23°, 13 °, 3° from the surface, respectively. The related results are from [4] and the open circles are related results from [5]. Image from [6, p. 101]

2.3. NanoMill®

The used equipment for low voltage Ar^+ ion milling is the Model 1040 NanoMill® TEM lamella preparation system [7] by Fischione Instruments. It is designed for the post-treatment of FIB-prepared TEM samples supported on transfer grids with 3 mm diameter, which is compatible with all common TEM holders.

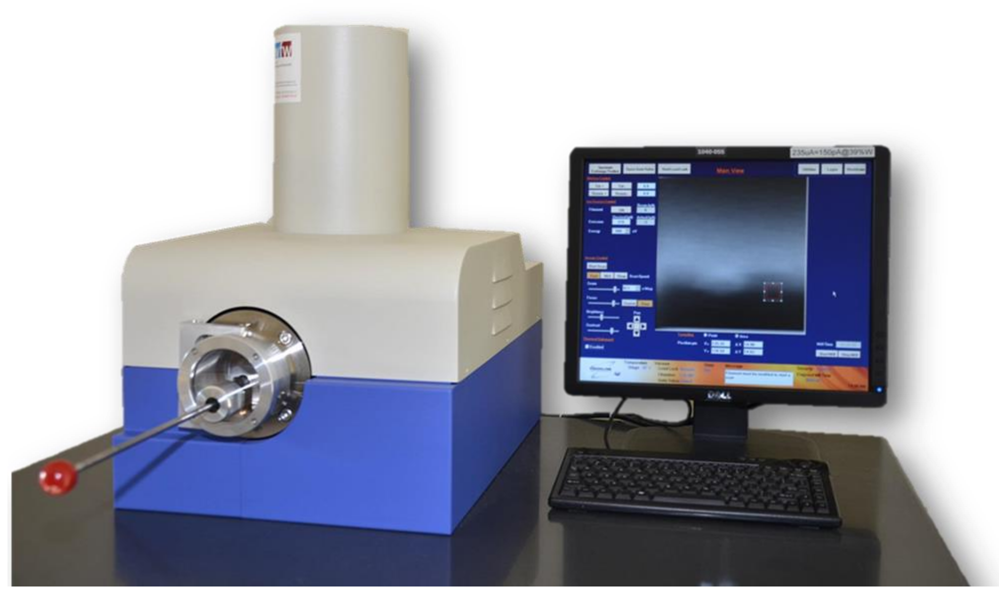

Figure 2-6: The NanoMill® and the computer screen with the interface for controlling the milling process.

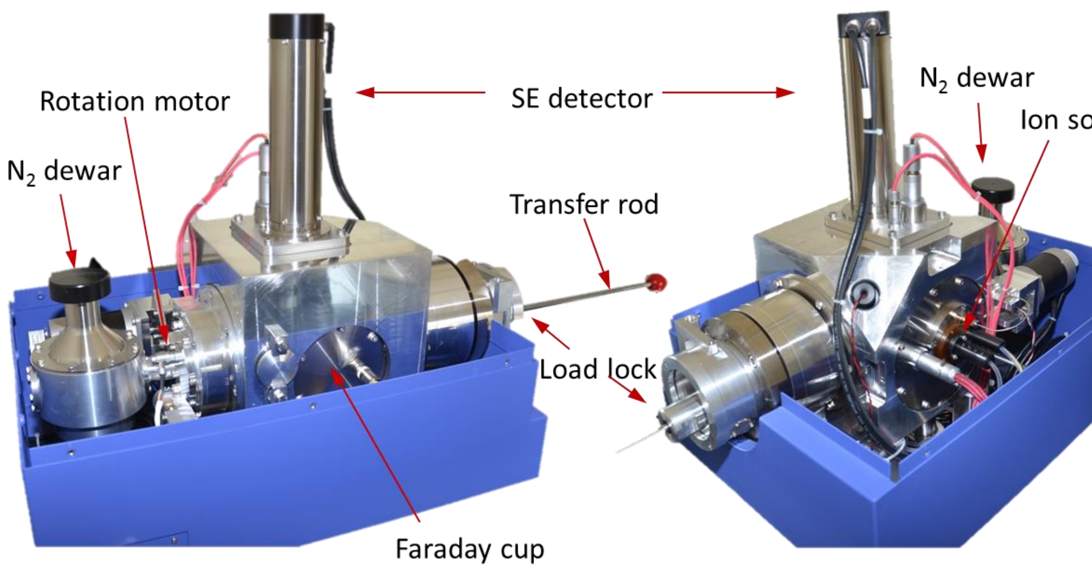

Figure 2-7: NanoMill® components in detail with opened cover.

The NanoMill® comprises the following essential parts:

- **Ion Beam Source**

The NanoMill® is equipped with an electron-impact device, which uses the ionization mechanism of electron bombardment on neutral argon gas. For the ionization, a certain threshold energy, called ionization potential, of the electron-ion interaction is needed. This corresponds to the energy of the outmost electron bond from the neutral ion, which needs to be disconnected [8, p. 22]. For creating a stable and uniform electron emission the NanoMill® is equipped with a yttria-coated iridium disc. This filament has the advantage of a low work function compared to commonly used refractory metals, which result in a higher electron yield [9]. As shown in Figure 2-8 neutral argon gas is inserted in the path of the electron beam and the excited ions are accelerated (in NanoMill® between 50 and 2000 V) and pulled out by the extraction plate. The Ar^+ beam is directed onto the lamella and is able to target either one spot for point milling or for area milling a target window can be selected. The impinging ions fulfil two functions: by hitting the surface of the sample secondary electrons are produced, which are used for imaging (secondary electron detector (SED)) and secondly for the purpose of removing surface atoms. This gentle sputter effect is used for polishing the sample surface, and for longer process times to reduce sample thickness. The low kinetic energy of the ions and the use of Ar^+ ions ensure that the milling is gentle and due to the focus of the beam of about 2 µm (at 900 eV ion energy) re-deposition is kept to a minimum.

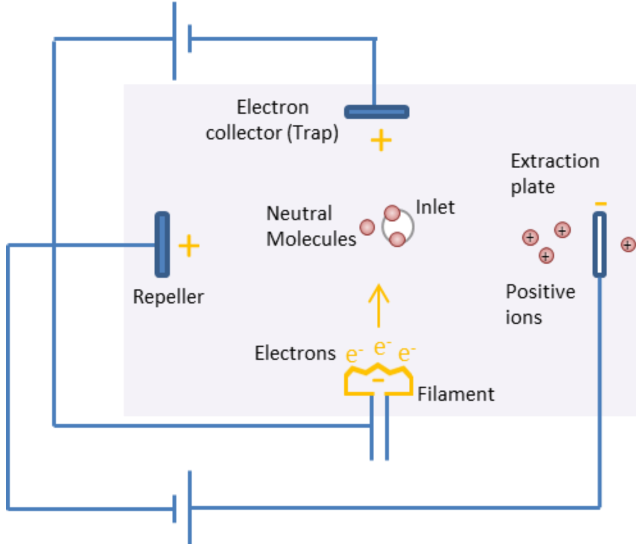

Figure 2-8: Scheme of basic principle of an electron impact device. (modified from [10, p. 4])

- **Vacuum Chamber / Pumps**

The vacuum is maintained with a turbo molecular drag pump (oil free) backed by an oil-free diaphragm pump. To measure the pressure in the vacuum, chamber a combination of a cold cathode and a Pirani gauge with a measuring range of atmospheric pressure down to 10^{-8} mbar is used. The system base vacuum is $3 \cdot 10^{-7}$ mbar.

- **Load Lock**

Via a load lock the sample can be inserted into the NanoMill® with a transfer rod. The prevacuum chamber is isolated from the main vacuum chamber by a gate valve. Due to the load lock there is no need to vent the main chamber for the sample transfer, resulting in very little waiting periods before the actual work with the NanoMill® can start. This time-saving component also favours the collaboration with the TEM examination due to the short sample turnover time of the NanoMill®.

- **Specimen Stage**

With the transfer rod the sample holder, containing the grid with the FIB lamella, can be transferred into the specimen stage. The specimen stage allows a 360° rotation of the sample holder and to tilt the sample in the range of -10° to +30°.

- **Cooling System**

During the milling operation, the stage can be cooled with liquid nitrogen (LN_2) to a temperature of -160 °C with a hold time up to 4 hours. All examinations of this thesis are performed at room temperature, but in the case of temperature sensitive samples the possibility of cooling during the milling process can be a great benefit.

- **Secondary Electron Detector**

An Everhart-Thornley detector collects secondary electrons, which are generated by the interaction of the ion beam and the sample, and thus creates an image of the sample. With 3 mm field of view an overview of the grid is easy to achieve. In the live view (scan mode: fast) the graphical user interface can be used to choose the settings of focus, contrast and brightness to get a clear view of the sample.

- **Faraday Cup**

With a faraday cup the ion beam current (1 – 2000 pA) can be measured.

2.4. Sputtering

Thickness reduction occurring during the FIB preparation and the process in the NanoMill® is based on the sputtering effect of impinging ions [11]. The sputter rate for a given material, i.e. how fast the surface atoms can be removed by ion bombardment, depends on the attractive surface binding energy of the atoms of the material, and parameters of the impinging ions: their incident angle, energy and mass. Rapid thinning can be realized by a high incident angle and high acceleration voltage. The number of atoms ejected from the surface per incident ion is called the sputter yield. Consequently, increased surface roughness and ion implantation can occur. At low incidence angles (<10°) a polishing effect can be reached with the result of a smooth surface, though the yield of sputtered atoms is smaller. The thickness of the amorphous material and the roughness of the surface have a huge impact on the achievable image quality during the TEM. However, a lower ion acceleration voltage leads to a thinner amorphous surface layer. The surface could be smoother [5, p. 161] though the occurrence of grooves in the direction of the ion impingement is possible. For interpretation and analysis, it is convenient to estimate at least the thickness of the ion induced amorphous layers. Further it is important to bear in mind that removed atoms can fall back on the sample surface and re-deposit or adsorb somewhere else in the system. Some materials show a higher affinity of the re-deposition of sputtered material than others. To minimize effects like ion implantation, amorphization of the top and bottom layer and both thermal and irradiation damage of the sample the angle of incidence ion and the acceleration voltage can be reduced. Consequently, for the same thickness reduction longer processing times are required. Further the cooling the sample is advisable for temperature sensitive samples.

As mentioned above, the removal of atoms near the surface happens, if the collision provides sufficient energy for overcoming the surface binding energy. The sputter events can be classified into 3 regimes according to the energy of the sputtered atom (after the collision) and on the spatial recoil density [12].

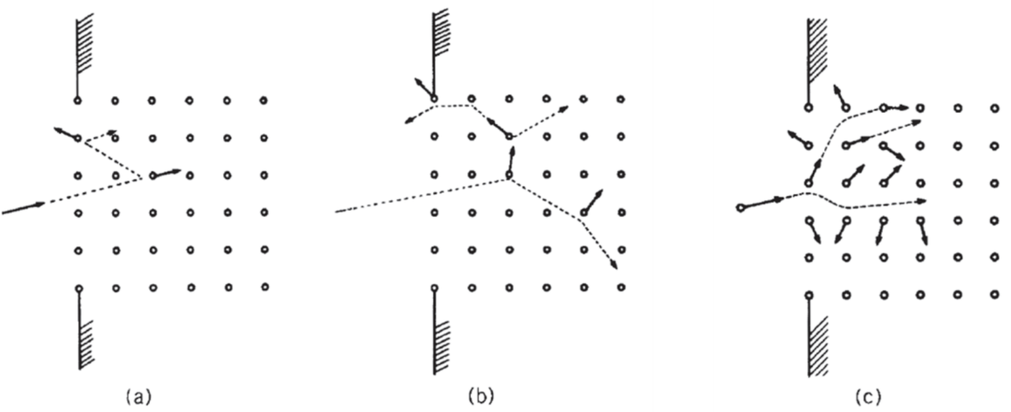

Figure 2-9: A schematic representation of sputtering by elastic collision: (a) Single knock-on regime. (b) Linear cascade regime. (c) Spike regime. Image from [13].

If the bombardment is very gentle (low energy or light projectile ions), like in the single knock-on regime, only a little amount of energy gets transferred to the surface atoms, which may escape into the vacuum due to the received energy. However, the energy is not high enough to generate a recoil cascade. In the linear-cascade regime a linear dependence of the sputter yield and the energy, which is transferred to the surface by the impact of the projectiles, is expected. During the collision, a large amount of energy is transferred to the surface atoms due to higher projectile masses with energies of a few hundred eV, which lead to collision cascades. In this cascade volume, only a few atoms are moving (see Figure 2-9 (b)) unlike the widespread movement in the spike regime, which is caused by projectiles with high atomic mass and sufficiently high energy. The sputter yield for this regime increases super-linearly with the energy deposited on the surface.

2.4.1. Sputter conditions in NanoMill®

In the NanoMill® Ar^+ ions with acceleration voltages between 50 and 2000 V can be used for the milling process. A schematic of a basic sputtering system can be seen in Figure 2-10 below. Milling at low voltages is primarily used to clean the sample surface, this enhancing the sample quality by reducing preparation artefacts. Higher acceleration voltages can be used to actually thin the sample to optimize its thickness and to remove FIB-induced amorphous layers. However, also ion milling with low voltages still may cause damage. The generation of amorphous layers and also structural changes depend on the material as well as the milling parameters. A linear dependence between incident angle and the thickness of amorphous material but also between the acceleration voltage and the amorphous layer thickness were found [14], [15, p. 388]. To examine the thickness of the generated layers a cross section of the lamella has to be prepared. More information of the so called double cross-section can be found in Chapter 2.5.2 (theory) and Chapters 3.8.1.4 and 3.8.2.4 (experiment).

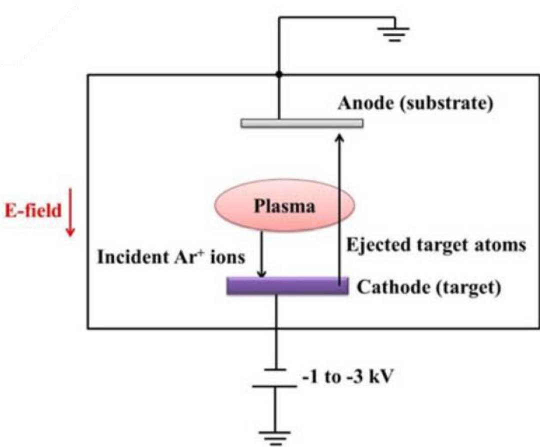

Figure 2-10: Schematic diagram of a basic sputtering system. Image from [16].

2.5. Thickness measurement

x-y mapping with high resolution can easily be performed with a transmission electron microscope, however measuring the thickness of the sample is difficult [17]. Nevertheless, accurate determination of the thickness of a sample is crucial for this work. To find out the sputter rate of a material, the thickness of the sample before and after the milling process must be known. Though there are many different methods for thickness determination the t/λ method is most popular in the material science sector due to its easy and quick realisation as well as the clear visual analysis of the relative thickness maps. The most accurate thickness detection is probably provided by positioned averaged convergent beam electron diffraction (PACBED), which is a derivative of convergent beam electron diffraction (CBED) [17, p. 231]. However, the latter method only provides thickness information about crystalline areas. Therefore, it underestimates the sample thickness by the extent of the amorphous layers. Respectively the artefact layers produced by FIB and NanoMill® cannot be detected. Another method is based on contamination particles positioned on top and bottom surface, which shows a lateral shift while tilting the sample. With this method, despite to CBED, the total thickness including amorphous outer layers can be detected, but it is with an accuracy of ±50 nm very imprecise and therefore not suitable for the examinations needed in this thesis. A destructive method is the preparation of a Double Cross Section (DCS), which means that the lamella is prepared perpendicular to the original cutting. This technique is linked with a time-consuming preparation, but provides detailed and accurate information about the sample structure.

2.5.1. t/λ method

The t/λ method is a popular way of determining the relative thickness of a sample. This procedure is based on the electron energy loss spectroscopy (EELS) log-ratio approach. It uses the concept of the mean free path (MFP) of inelastically scattered electrons. For this setup, the MFP is the average distance an electron would travel in the sample before a scattering event takes place. Inelastic scattering, which is connected to an energy loss of the electron, is more likely to happen for materials with smaller MFP. Also for thicker sample regions there is a higher probability that an electron passing through the sample will lose energy during an interaction. The scattering probability can be described with the Poisson statistics [18]. The probabilities of n-fold scattering (equation 2.2) and no scattering (equation 2.3) can be seen below [19, p. 4].

$$P_n = \left(\frac{t}{\lambda}\right)^n \frac{1}{n!} e^{\left(-\frac{t}{\lambda}\right)} \qquad 2.2$$

$$P_0 = e^{\left(-\frac{t}{\lambda}\right)} = \frac{I_0}{I} \qquad 2.3$$

$$\frac{t}{\lambda} = ln\left(\frac{I}{I_0}\right) \qquad 2.4$$

t ... sample thickness
λ ... mean free path
I ... integral under total spectrum / intensity of BF image
I_0 ... integral under zero-loss peak / intensity of ZL filtered image
e ... Euler's number
$n!$ ... is the factorial of n with $n = 0,1,2...$

$t/\lambda > 0$ is the expected value and at the same time the variance of the Poisson distribution. e is Euler's number. n is a non-negative integer and n! is the factorial of n.

From the Poisson distribution for the case of no scattering the equation for relative thickness t/λ (equation 2.4) can be deduced.

According to equation 2.3 for the t/λ method it is necessary to measure the total electron intensity I_t and the number of elastically scattered electrons I_0. By using an imaging filter an image can be created with these electrons: The image created with only elastically scattered electrons is called zero loss filtered image (ZL). In addition, an unfiltered bright field image (BF) is generated by electrons from the whole EEL spectrum. Between the acquisition of the BF and the ZL image as little time as possible should elapse to ensure the sample drift is small.

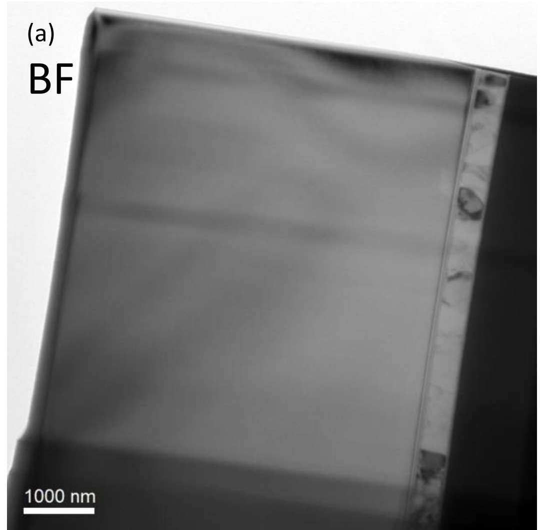

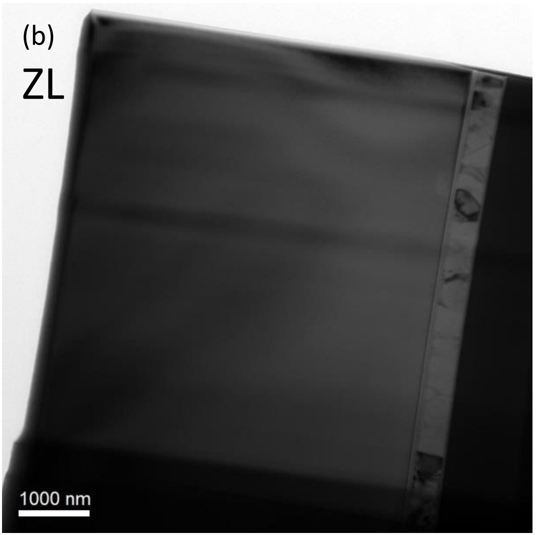

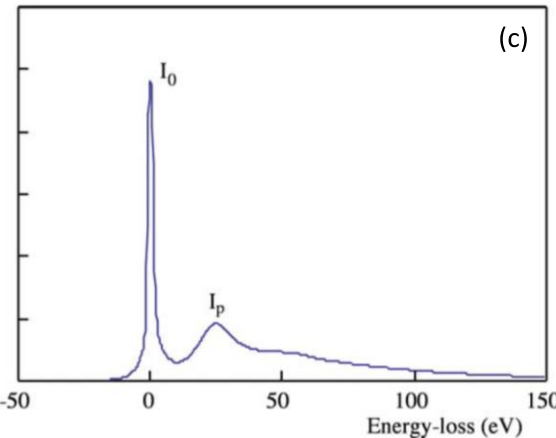

Figure 2-11: (a) Bright field image of FIB lamella. (b) Zero loss filtered image. Both pictures are recorded with the TEM CM20. (c) Typical electron energy loss spectrum with an intense ZLP (I_0) and the plasmon peak in the low loss region (I_P). [2, p. 701]

Gatan's Digital Micrograph (DM) [20, pp. 3-18-3–21] is a software for visualization and analysis of the TEM images. DM gives the opportunity to calculate relative thickness map (see Figure 2-12) with the t/λ method using the BF and the ZL image. To correct a possible sample movement between BF and ZL image DM makes a drift correction between the two images, therefore the exact same areas from both images are combined to a relative thickness map. The exact procedure can be seen in Chapter 3.6.

In Figure 2-12 the resulting relative thickness map of the BF and ZL images shown in Figure 2-11 can be seen.

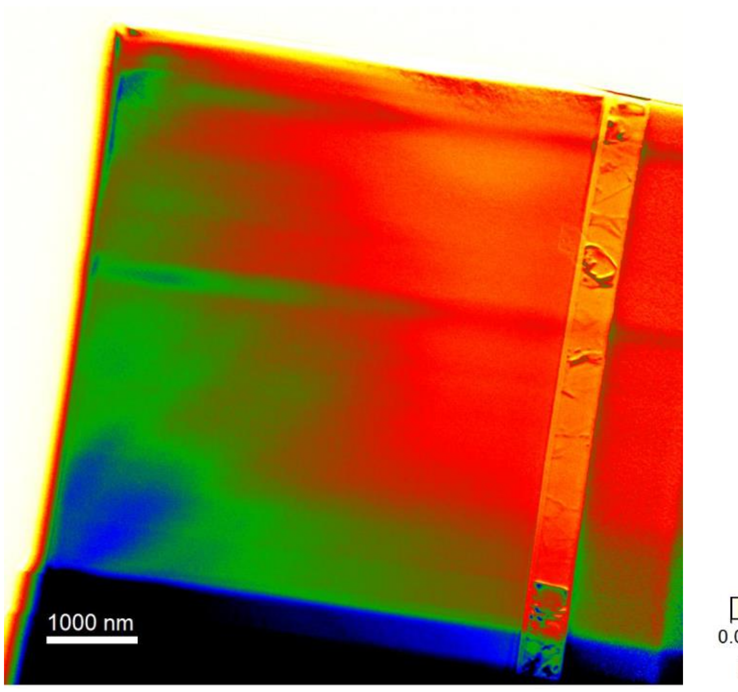

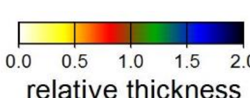

Figure 2-12: Relative thickness map of a TEM lamella with a contrast limit of 0.0 – 2.0.

For the determination of the absolute thickness of a sample the MFP (λ) of the material must be known. Then equation 2.4 can be rewritten as: $t = \lambda \cdot \ln(I/I_0)$. In the range of $0.2 < t/\lambda < 5$ this linear relationship is valid within an accuracy of ±10% [21].

To ensure that the calculated total thickness is correct it is crucial to find an accurate value of the mean free path for the investigated material. For pure elements, like Si, literature research will lead to good results, but for compounds, like the semiconductor SiC or a ceramic (lead zirconate titanate), which are of interest for this work, only little information can be found in literature. A comparison of the theoretical information found by online MFP calculators to experimental data shows, that the calculated results should be treated with caution. The experimental and theoretical determination is explained in the following subchapters.

2.5.1.1. Theoretical MFP determination

The MFP depends on the material the electron has to pass as well as on microscope parameters like the acceleration voltage E_0 and the EELS collection semi-angle β. The following approach can be used to calculate the MFP [21, p. 232].

Parameterised form of the MFP is used to calculate the MFP of the materials listed below in Table 2-1.

$$\lambda(nm) = \frac{106 \cdot F\ (E_0/E_m)}{ln(2E_0\beta/E_m)} \qquad 2.5$$

$$with\ relaticistic\ factor\ \mathrm{F} = \frac{1 + E_0/E_m}{(1 + E_0/511)^2}\ and\ E_m = 7.6\ Z^{0.36}$$

λ ... mean free path
E_0 ... incident energy in keV
β ... collection semi angle in mrad
Z ... atomic number

By knowing the chemical composition of a material, the mean free path can be calculated with an accuracy of ±20% [21].

Table 2-1: List of calculated MFP values only valid for the CM20 microscope parameters (200 keV, β = 3.63 mrad).

Material	λ/nm
Silicon carbide	167.7
Lead zirconate titanate	154.9

A transmitted electron does not only loose energy while traveling through the sample, but also at the entry/exit at the two surfaces. Therefore, the single scattering distribution S(E) = S_V(E) + S_S(E) [21, p. 232] contains a term for surface-mode scattering loss S_S(E) and a volume-loss component S_V(E). Parameters like the surface roughness and degree of oxidation or amorphous layers would influence the surface-loss contribution. However, because most influence of the surface is expected for very thin samples and an energy region of 0 – 10 eV it was not taken into account for the calculations in this thesis. This enhances the accuracy of the thickness determination.

2.5.1.2. Experimental MFP determination

To confirm the theoretical calculation of the MFP an experiment for the determination of the mean free path was performed. If the thickness of a sample is known one rewrites equation 2.4 for the relative thickness to $\lambda = t/ln\left(\frac{I}{I_0}\right)$ and calculates the MFP. For the realisation of this approach an object with special symmetry, which is accompanied with known thickness (e.g. a needle with known diameter, which is used in this work) needs to be prepared followed by a relative thickness measurement with the t/λ method. From this data and the known thickness, the MFP can be calculated. However, also systems with other known symmetry like a cube, where the absolute thickness can be measured by the 2D projection image, would be possible test objects. The advantage of this approach is that no information of the microscope parameters is needed. If the MFP can be determined precisely an accuracy of the thickness of ±10% can be reached [19]. In Section 3.8.1.5 of the practical part the experimental MFP determination of a SiC needle is described.

2.5.2. Double Cross Section

The following images show the preparation steps for a Double Cross Section (DCS), which is a cross section of the cross section, i.e. a FIB lamella. They were recorded from the DCS performed on SiC and a ceramic sample. The detailed description of the experiment and the results can be seen in the experimental part in Section 3.8.1.4 and 3.8.2.4 [22].

Before the Pt protection layer (it also serves for the stabilization of the lamella) is deposited on the lamella, the operator should determine the area of interest very precisely. This can be understood if looking at the end of the preparation (see Figure 2-17). Due to the nature of the method only a very thin section of the sample will remain for the examination. After locating the area of interest the Pt can be deposited on both sides of the lamella (seeFigure 2-13 and Figure 2-14) to protect it from damage in the next preparation steps [23].

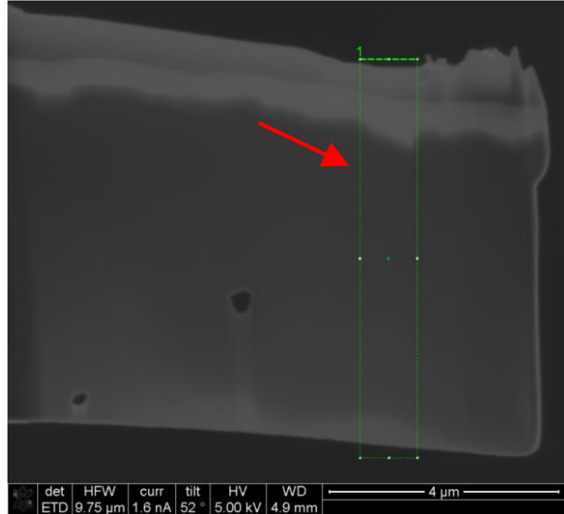

Figure 2-13: FIB lamella. The rectangle indicates the location for Pt deposition (front view).

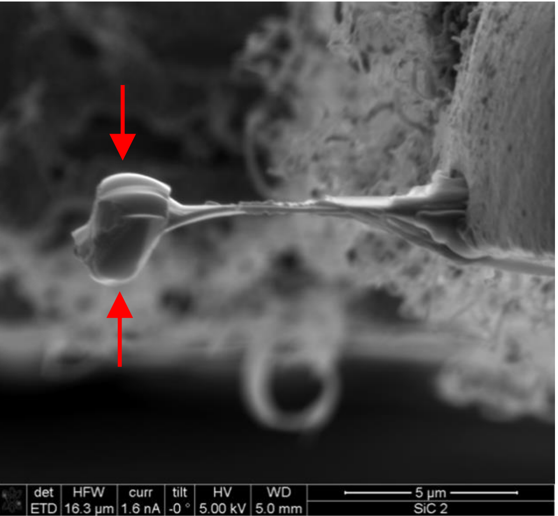

Figure 2-14: Pt deposition to protect FIB lamella (top view).

The fixation of the FIB lamella on the micromanipulator ensures a safe transport of the front section (A), which is detached from the remaining lamella (see Figure 2-15.), to the final position. In order to ensure that the section plane of A is facing the examiner during the TEM investigation, it must be fixed sideways (see Figure 2-16) in top position (vertically) on the finger of the grid. This procedure is known as “upside down” preparation.

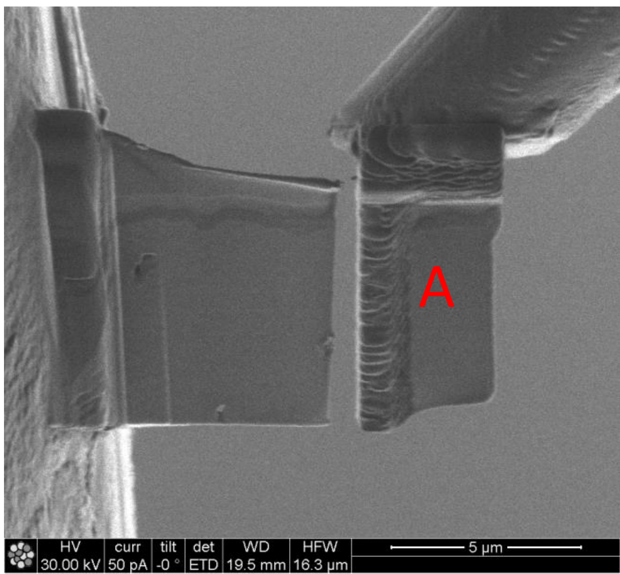

Figure 2-15: After fixing the micromanipulator to the sample the front section (A) of the lamella can be cut.

To examine the cross section of the lamella in the TEM it must be thinned to electron transparency. The thickness decrease can be seen in the figures below. In Figure 2-17 the lamella can be seen clearly as the brightest elongated shape feature in the centre marked with the red arrow. The sample is surrounded by the electron- (lighter grey) and ion beam (darker grey) deposited Pt.

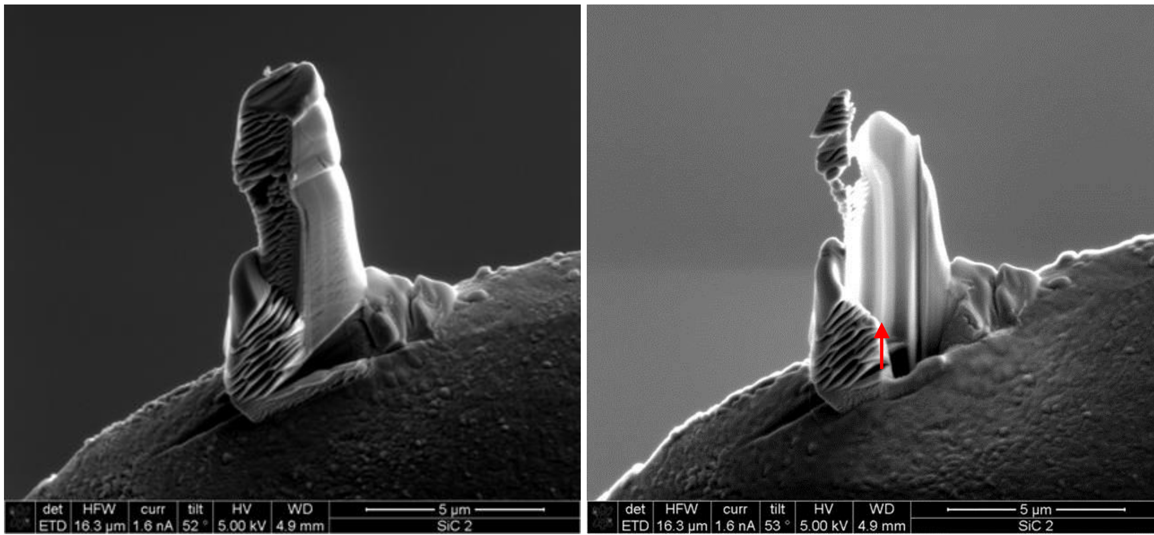

Figure 2-16: For the TEM investigation the sample must be thinned to electron transparency.

Figure 2-17: The original lamella can be seen in the centre as the brightest elongated feature marked with the red arrow.

3. Practical Work

In the following chapter the instrument handling as well as the experiments in the TEM CM20 and the NanoMill® and the obtained results will be described. Figure 3-1 gives an overview of the work process. To find out the sputter rate in this work an iterative approach of thinning the sample with the NanoMill® and measuring the relative thickness via t/λ method in the TEM CM20 is performed. It is crucial to point out, that this procedure must be repeated for every set of parameters and every material to get a consistent characterisation. Further investigations of the two examined materials to verify the real lamella thickness and to determine the preparation induced amorphous layer sitting on both sides of the sample are performed with a Double Cross Section of the lamellae.

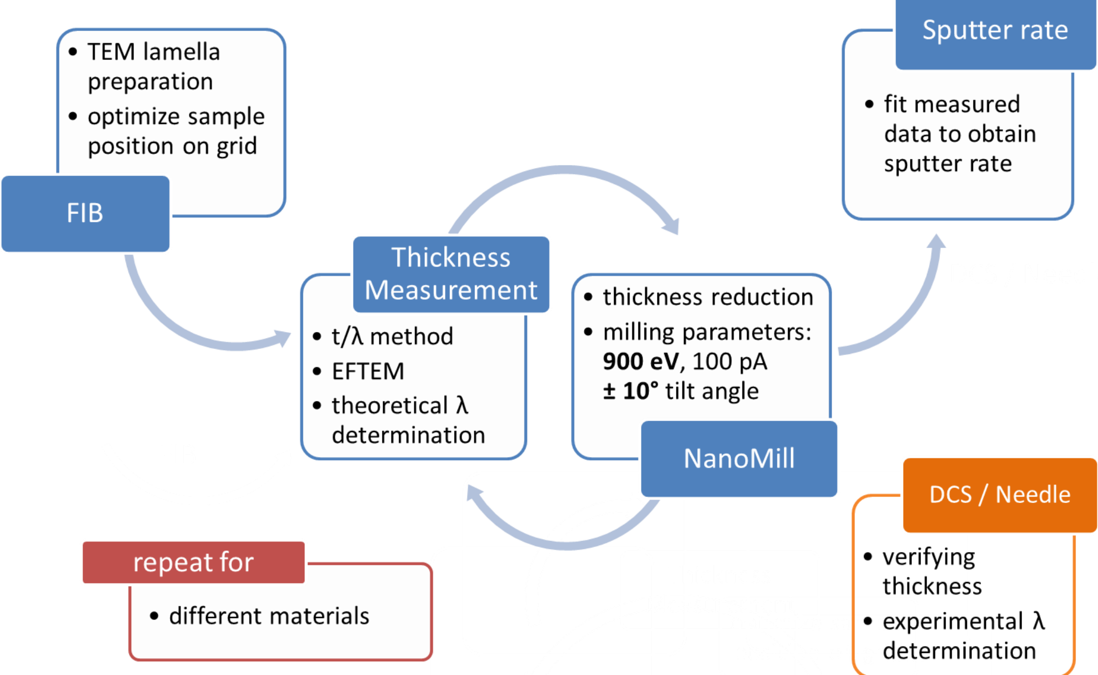

Figure 3-1: Overview of work process starting with the TEM lamella preparation followed by the alternating milling and thickness measurement with the aim to determine the sputter rate (blue). Additionally, an experimental approach to determine the mean free path is indicated (orange). For every set of parameters and for each material the procedure must be repeated. To verify the thickness and to distinguish the amorphous and crystalline part of the lamella a Double Cross Section (DCS) is examined. To determine the mean free path via an experiment a needle prepared with the FIB is investigated.

3.1. NanoMill® operation

3.1.1. Load the sample

This section contains a step per step description of the adequate way to load the grid in the sample holder and should draw attention to requirements needed for a successful post-treatment. Wearing gloves and a cautious handling of the sample is crucial for the loading procedure.

Because of the small size of the sample holder the loading station as seen in Figure 3-2 (c) facilitates the loading/unloading procedure of the sample [7, p. 63].

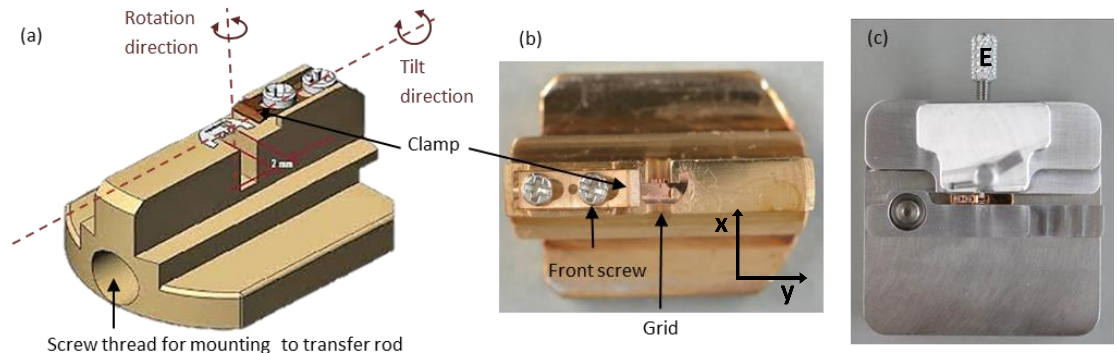

Figure 3-2: Brass sample holder with sample-support grid. In (a) the red dashed lines indicate the direction of the rotation and the tilt of the stage. Image modified from [24, p. 4]. (b) Photography of the sample holder. (c) Loading station.

1. Place the sample holder (see Figure 3-2 (c)) in the loading station.
2. To open the clamp, the front screw, which fixes the sample, needs to be loosened.
3. To insert the grid, the use of vacuum tweezers is advisable. Attention should be paid to an **even position of the grid**, which means that the finger with the sample should be located in the centre which corresponds to the intersection of the tilt and the rotation axis.
4. To eject the sample holder from the loading station it is equipped with an ejector knob (E).

Unloading the sample

The sample can be removed from the holder with vacuum tweezers after loosening the front screw. If the sample is known for an affinity of interacting with oxygen, the sample holder with the sample can be transferred from the NanoMill® directly into a Plasma Cleaner. A minimum exposure to air ensures less oxidation.

3.1.2. Transferring the sample

After the loading procedure, the sample holder should be inserted into the protective box (see Figure 3-3). This cover ensures a save transport to the NanoMill® and an easier fixation of the sample holder on the transfer rod.

The following list gives a step per step description for the sample transfer into the NanoMill® [7, p. 67]:

1. Slide the protective box over the sample holder.

Figure 3-3: Protective box with sample holder and transfer rod.

2. To open the load lock the operator has to use the software M1040 and click 'vent load lock' in the main view (see Figure 3-6).

3. Screw the holder on the transfer rod, remove the protective box, close the load lock and pump the pre-chamber with 'pump load lock' (see Figure 3-6).

4. As soon as a pressure of about 0.1 torr on the load lock is reached the gate valve can be opened with the corresponding button. This is the only waiting period of the whole transfer process.

5. Slowly push the transfer rod till the sample holder slides into the stage and reaches the end position. Rotate the transfer rod counterclockwise and retract it with care to loosen it. This is a critical step because the sample holder could fall into the vacuum chamber, if the sample holder is not completely separated from the transfer rod.

6. Make sure the transfer rod is pulled back to the outmost position before the gate valve is closed.

After the gate valve is closed the filament und the imaging can be started. With practice the loading of the sample and the transfer into the NanoMill® can be done in less than 3 minutes.

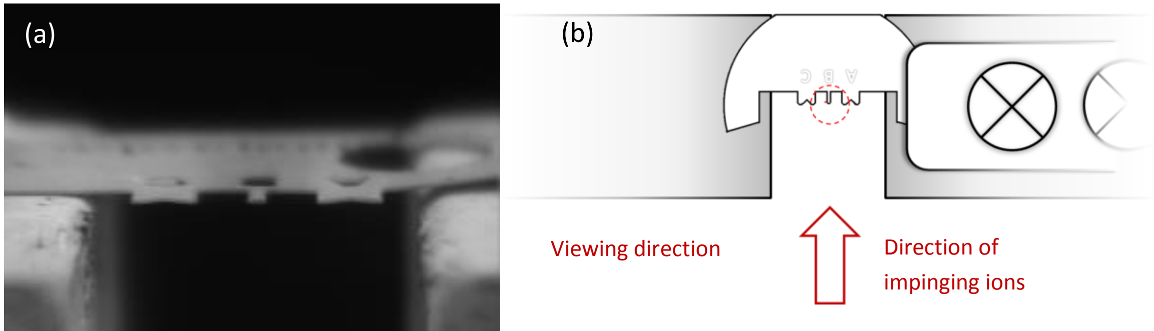

Figure 3-4: View in the NanoMill® on the sample, with a minimal tilt, to demonstrate the direction of impinging ions, which is also the viewing direction. (b) Corresponding scheme.

Transferring out

For transferring the sample holder out of the NanoMill® the above described procedure is performed in reverse.

3.1.3. Tilt and Rotation

The stage gives the opportunity of a 360° rotation and a stage tilt of -10 to +30°. The tilt axis and the rotation axis of the sample holder can be seen in Figure 3-2 (a). The finger containing the sample should be positioned right in the centre of the holder.

The rotation function is used to get a clear view on the lamella. The even positioning of the sample in the holder, as described in Section 3.1.1, should be performed as well as possible. However, deviations from the parallel position can be adjusted via a rotation of the grid. The adequate finger position can be seen in Figure 3-5.

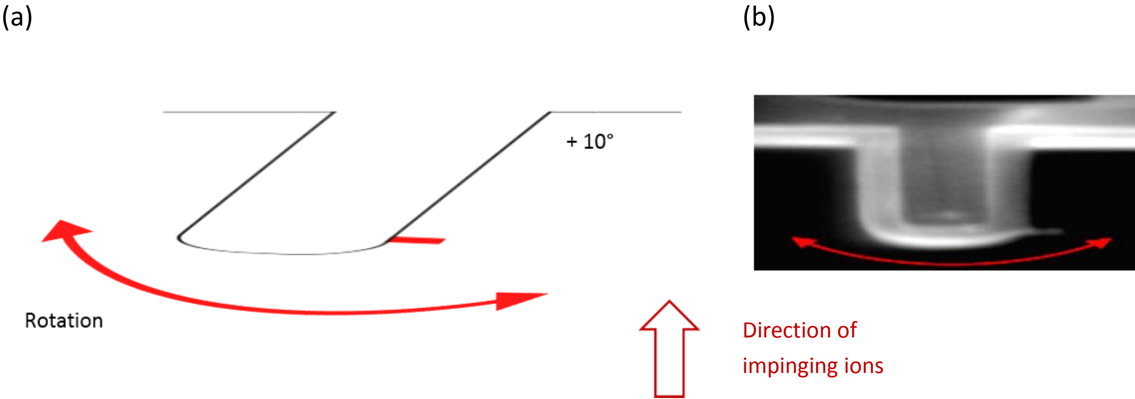

Figure 3-5: (a) Scheme of lamella on finger in a rotated position, in which it is not possible to perform the milling. The red arrow indicates the direction of the rotation. (b) NanoMill® image of desired alignment: The finger is aligned parallel to the impinging ions.

Depending on the geometry of the grid and the position of the sample on the finger a certain tilt angle is necessary to get a clear view on the lamella, which is a necessity for the milling process. The tilt angle can be adjusted by inserting the desired value in the software, the motor of the stage will immediately execute the command and the motion can be observed by a life view. In this work, all tilt angles are noted with respect to the direction parallel to the surface of the 0° position.

3.1.4. Milling of the sample

Before the milling process can be started a clear view on the lamella is required. Therefore, focus, brightness and contrast can be adjusted with the slide bars of the imaging section at the NanoMill® user interface M1040 shown in Figure 3-6.

In this thesis, all materials are examined with the same set of parameters, which are listed below and can be adjusted in the software.

Milling Parameters

Source Energy	900 eV
Source Emission / Beam Current	200 µA / 100 pA
Tilt	± 10°
Magnification	911x

Figure 3-6 shows a screen shot of the interface called 'Main View' containing different sections for controlling the milling process. The buttons 'Vent' and 'Open' are for the transfer of the sample into the NanoMill®. In the second section the desired tilt and rotation can be applied. By pushing the 'Exchange' button the zero position can be reached with one click. In the section 'Ion Source' the energy and emission can be set and the filament can be started or stopped.

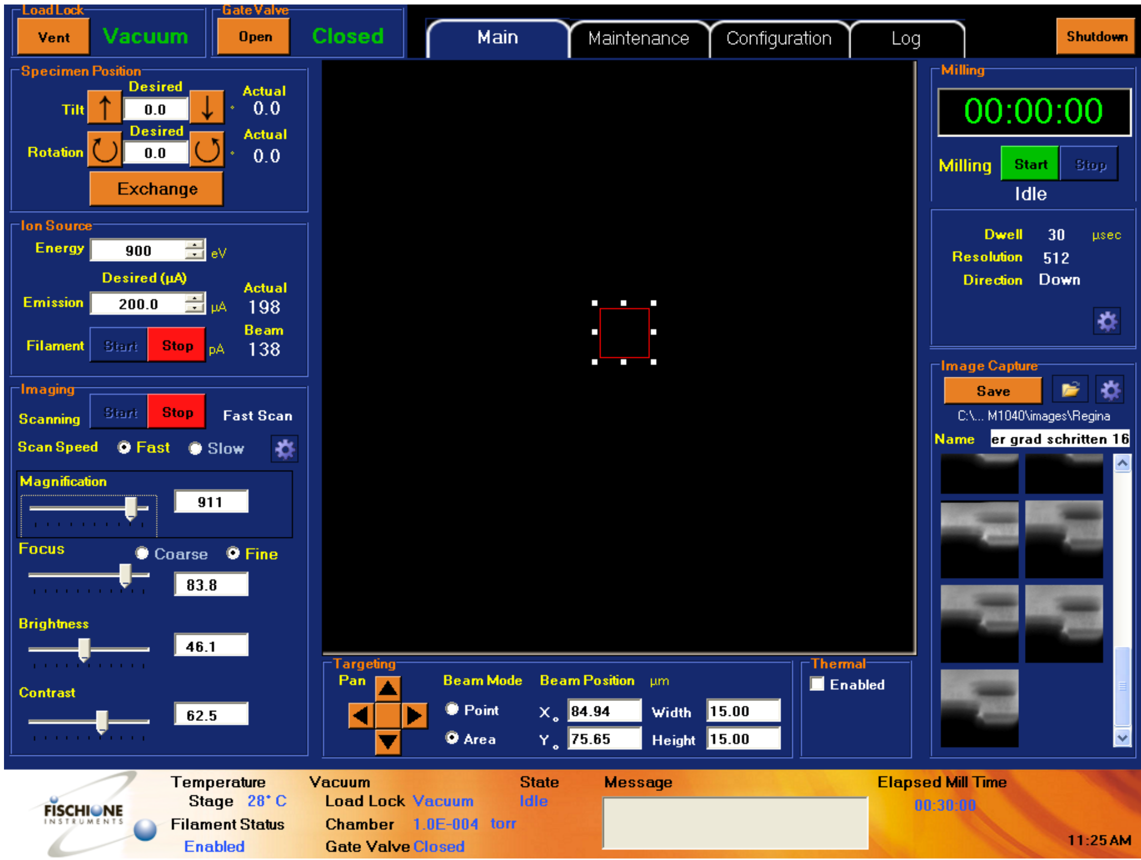

Figure 3-6: 'Main View' of the interface of the application software M1040.

For getting a clear view on the lamella in the user interface the focus, brightness and contrast can be adjusted with the slide bars of the 'Imaging' section. A clear picture of the lamella is a requirement for an appropriate milling - on the one hand to be sure to hit the sample uniformly and on the other hand due to geometrical restrictions. The target window must be set in a position that the ions are only impinging the sample and not the grid, otherwise re-deposition of the sputtered material occurs. This constraint can only be met if the distance of the lamella to the grid is big enough (see Figure 3-7). This issue will be discussed in chapter 3.2 'Optimal Sample Position' in more detail.

Figure 3-7 shows a view on the FIB grid with a target window (a) and some geometrical considerations for the milling pattern placement (b, c).

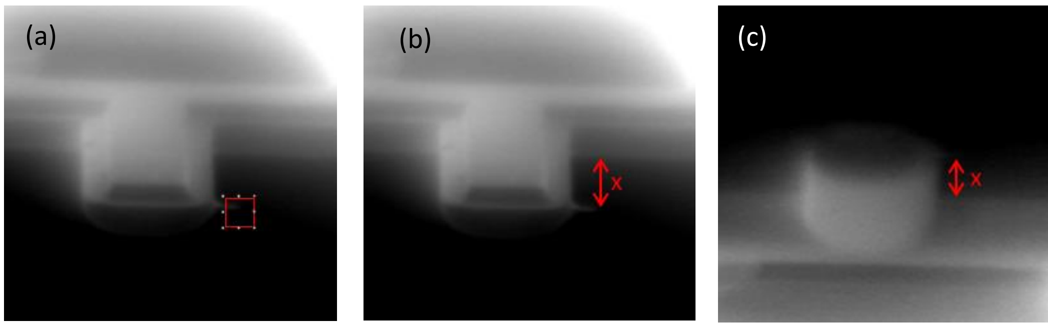

Figure 3-7: Images from NanoMill® with a tilt angle ±10°. In (a) the lamella with the target window can be seen. The red rectangle corresponds to the milling area. In (b) and (c) the arrow indicates the distance between the lamella and the grid. (c) shows a tilt angle of -10°. The lamella is hardly visible.

In this work a target pattern with the size of 15x15 µm is used. The desirable position of the pattern can be seen in Figure 3-7 (a). The target window should cover 1/2 - 2/3 of the lamella area, but in the same time a sufficient distance from the grid is a necessity to avoid contamination from sputtered grid atoms. To fulfil this restriction the distance x, see Figure 3-7 (b) and (c) must be big enough. The clear distance difference can be explained by the geometry of the grid and will be discussed in Chapter 3.2.

As stated above re-deposition is undesirable. In order to avoid this contamination in addition to the right position of the milling area also the scan direction should be chosen in a particular way. The possibilities can be seen in the figure below. It is advisable to choose the milling process direction which ends in the vacuum.

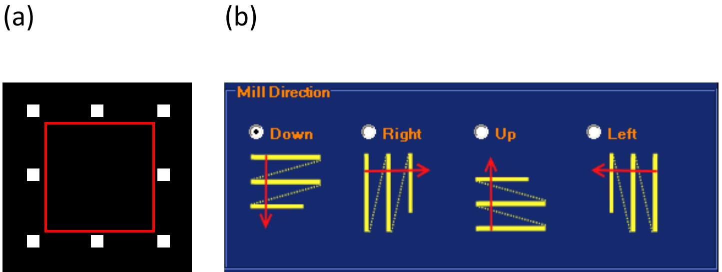

Figure 3-8: (a) Target window and (b) choice of possible milling directions in the interface of M1040.

3.1.5. Astigmatism correction

For the best possible milling performance, it is necessary to correct the astigmatism of the NanoMill® imaging system. This correction can be done manually via two very sensitive screws, therefore minimal turns with the screwdriver lead to a great impact. The screws are marked in Figure 3-9 with X-Shaft and Y- Shaft. By turning an alignment of the ion source with respect to the focusing lens can be done. A misalignment is noticeable by a movement of the image in the live view while changing the focus. The aim is to minimize the movement of the image while changing the focus to check the progress. With the X-Shaft the horizontal movement of

the image can be changed and with the Y-Shaft the motion in vertical direction. This should be repeated alternately till a minimum of motion is obtained.

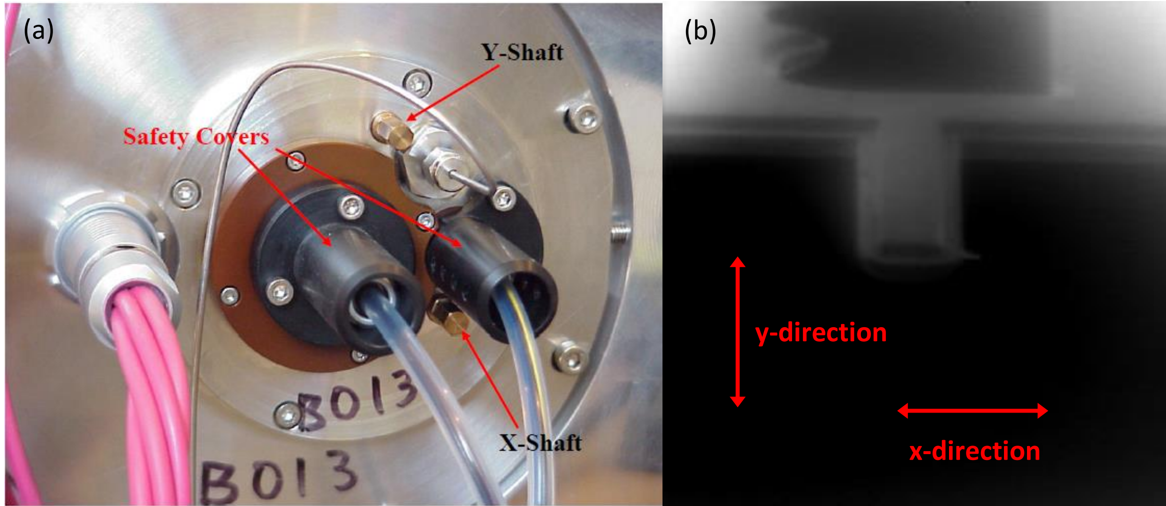

Figure 3-9: (a) If the cover of the NanoMill® is open, you can see the backside of the ion source. The two brass imbus screws are marked with X-Shaft and Y-Shaft [7, p. 90]. The arrows in Figure (b) show the directions which can be corrected by rotating the X-Shaft and Y-Shaft clockwise/counter clockwise.

It is advised from the manufacturer to make the alignment at a tilt angle of -30°, energy of 500 eV and emission of 200 µA and adjusting brightness and contrast for the best possible image. However, the alignment setting is a function of the energy, therefore the alignment should be performed at the intended milling energy.

A possible disadvantage is that the set values for the X-Shift and Y-Shift cannot be read off. As mentioned the correction depends on the energy, therefore it would be handy to have a listed value for common energies and a possibility to set it via the software instead of the very sensitive manual adjustment with the screwdriver.

3.1.6. Assets and drawbacks

In this section the advantages and disadvantages of the NanoMill® and its handling are described. Especially characteristics, which are found during the practical work of this thesis, are pointed out.

+ **Post-treatment with NanoMill®**

The NanoMill® gives the opportunity of targeted low energy Ar^+ ion milling. The focused milling helps to minimize re-deposition. FIB induced artefacts can be removed and for longer process times also the sample thickness can be reduced. The use of low energies ensures the generation of small amorphous layers. Another benefit, which should be noted, is the use of light Ar^+ ions, which are by far not as influential as the heavy Ga^+ ions used in the FIB. Ar^+ ion implantation is very unlikely and therefore can be neglected regarding the interpretation. To

sum up, the reduction of the lamella thickness and the small amount of defects which are created with the NanoMill® treatment enhance sample quality.

+ **Load lock**

The main advantages of the prevacuum chamber (see Figure 3-11) are the protection of the main chamber from contamination and the time saving. It makes the transfer simple and fast. Further the periods, to reach the operating vacuum for starting the filament, are very short. These assets favour the collaboration with TEM operators.

+ **Cooling**

The cooling system with liquid nitrogen was not needed for this work, however for the milling of sensitive samples a cooled stage could be an important advantage. Temperatures down to -160°C for a hold time up to 6 hours are possible. To avoid drift of the sample holder and to ensure a stable temperature a waiting period of 30 min is advisable.

– **Drawback of unsymmetrical tilt angle**

The unsymmetrical tilt angle range of -10° to +30° is unfavourable. The sample can be clamped upside down (see Figure 3-10) to circumvent this limitation, which is connected with an additional transfer. If the milling process requires a tilt angle > ±10° the milling has to be separated in two steps. First a milling on the front side with a tilt in the positive direction has to be performed, then the sample need to be unloaded, turned to the backside and be transferred into the NanoMill® to perform the milling process on the second side (again with the tilt in the positive direction). With practice and due to the load lock the loading and the transfer of the sample is a not very time consuming procedure, nevertheless the unsymmetrical tilt angle range is unfavourable.

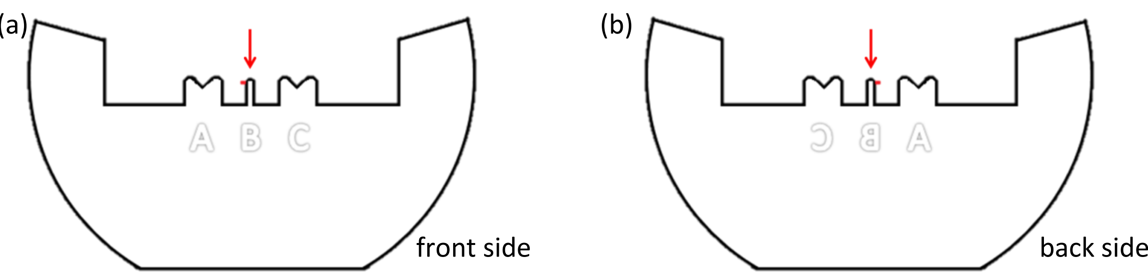

Figure 3-10: Scheme of the front and back side of a common TEM grid with a sample fixed in flag-position.

Figure 3-11 demonstrates the very small distance between the sample holder and the ion source, which could be the geometric reason for the asymmetric tilt angle range of -10° to + 30°.

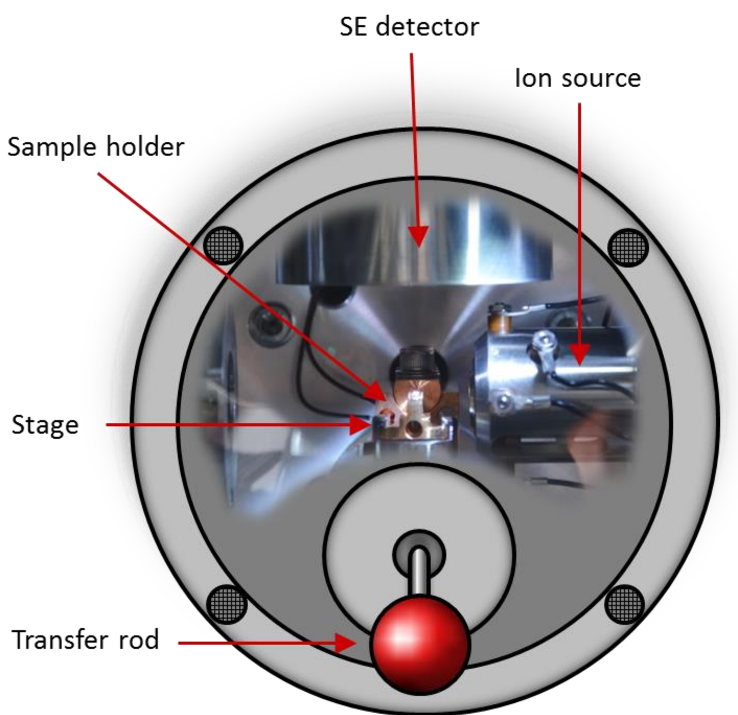

Figure 3-11: This scheme shows the view through the load lock window inside the NanoMill®. The stage with the sample holder in the centre, the ion source on the right-hand side and the SE detector above the sample can be seen.

– **Free positioning the grid in sample holder**

For choosing tilt angles of ±10° or even smaller, the fixing position of the lamella on the grid becomes crucial due to geometrical constrains. This is also influenced by the position of the grid in the sample holder. There are no end stop concerning the location of the sample in the holder, which means that the position, also if loaded with care, will differ for every milling pass.

The impact of the misalignment of the grid in the sample holder (see examples in Figure 3-12), must be considered in the milling process. It has no influence on the tilt angle but on the milling quality, because the astigmatism is only corrected for a certain area (approx. red circle). A different focus setting is accompanied with different milling conditions. The displacement, seen in Figure 3-12 (d), can be easily corrected by the rotation of the stage. Nevertheless, it is unclear how well the astigmatisms are corrected for this position. For the optimal milling conditions, the astigmatisms should be checked and adjusted before every milling process.

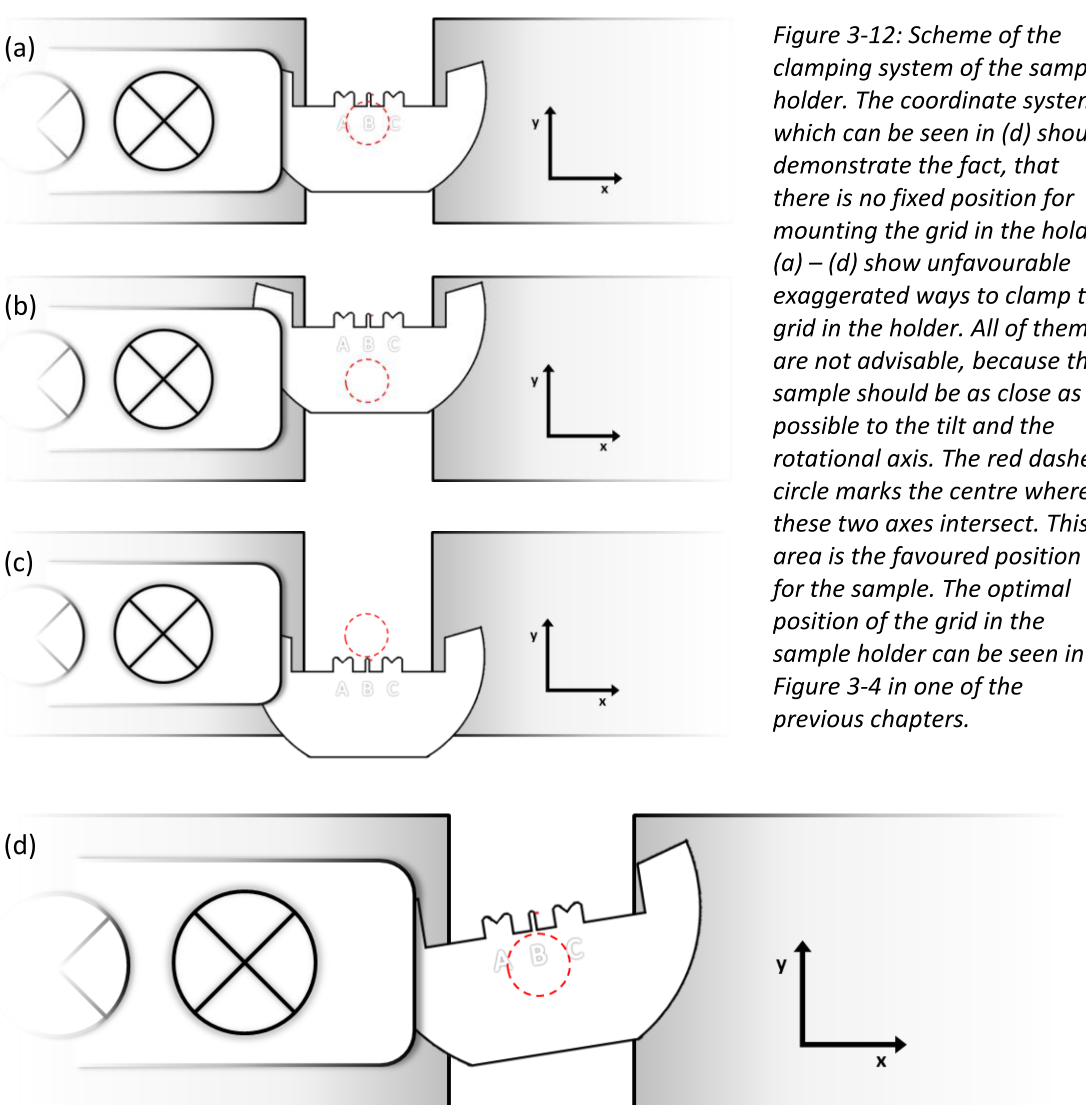

Figure 3-12: Scheme of the clamping system of the sample holder. The coordinate system, which can be seen in (d) should demonstrate the fact, that there is no fixed position for mounting the grid in the holder. (a) – (d) show unfavourable exaggerated ways to clamp the grid in the holder. All of them are not advisable, because the sample should be as close as possible to the tilt and the rotational axis. The red dashed circle marks the centre where these two axes intersect. This area is the favoured position for the sample. The optimal position of the grid in the sample holder can be seen in Figure 3-4 in one of the previous chapters.

± **Freedom of positioning the lamella on the grid**

The position of the lamella on the grid is of prime importance if the milling is performed at low angles due to the already mentioned restriction that the target window must be chosen in a way, that the ions which are not impinging the lamella are shot in the vacuum, otherwise re-deposition occurs. By knowing that low milling angles are used, one can adapt the position of the lamella on the grid. Further the shape of the grid is of great importance (see Chapter 3.4). A detailed description of the related problems is given in the next section.

3.2. Optimal Sample Position

As already mentioned in the previous chapters the position of the sample on the grid is of great importance. The way the lamella is fixed on the finger becomes important for the whole milling process. It even turns out, that a few positions make a post-treatment with the NanoMill® impossible due to geometrical reasons. The chapter is sectioned in 3 parts: the common way of lamella fixation is portrayed, followed by the obstacles which can occur with this configuration, and by an implementation concept. All investigations of this chapter are conducted with an Omniprobe grid. This is worth mentioning because it turned out that geometrical restrictions are highly influenced by the geometry of the grid. A comparison to other commercially available grids is given in Section 3.4.

In a first step one must abandon the general idea of a flat TEM grid. At a closer view, shown in Figure 3-13, it is clearly visible, that the grid possesses a flat front side and a curved back side and that it is far thicker than the lamella.

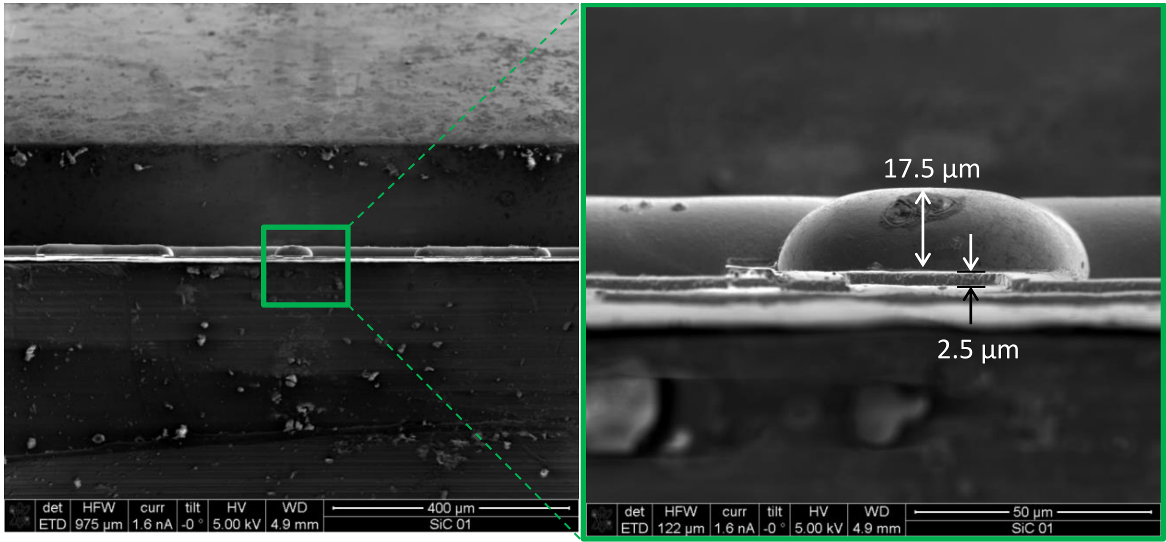

Figure 3-13: This images show a common Omniprobe TEM grid at a tilt angle of 0°. The curved side has a maximum thickness of 17.5 µm and the flat layer on the bottom is 2.5 µm thick which add up to a total thickness of 20 µm.

Over the last years a routine concerning the lamella fixation has been established. This common way of fixing a lamella on the grid can be seen in Figure 3-14 (a) below. Next to it examples for unfavourable positioning are illustrated: a tilt of the lamella, top position and a fixation to close to the main body of the grid.

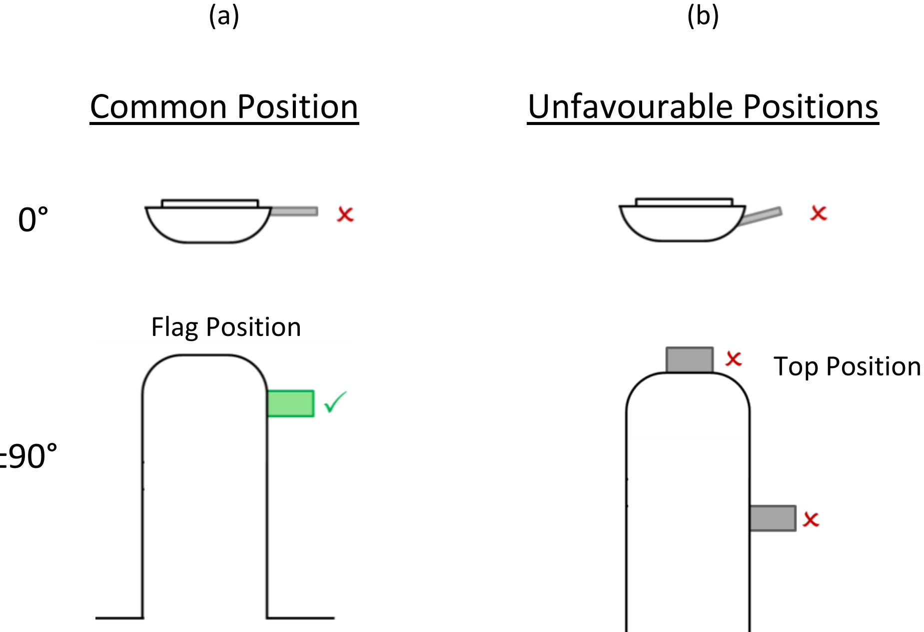

Figure 3-14: (a) Common way of fixing a lamella on the finger. In (b) unfavourable positions of the lamella on the grid can be seen.

A tilted fixation can lead to wrong thickness estimation due to the longer path the electrons have to travel in the material (see Chapter 46). Why the top position and the low flag position of the lamellae in Figure 3-14 (b) are not advisable for the NanoMill® post-treatment can easily be demonstrated in the following image:

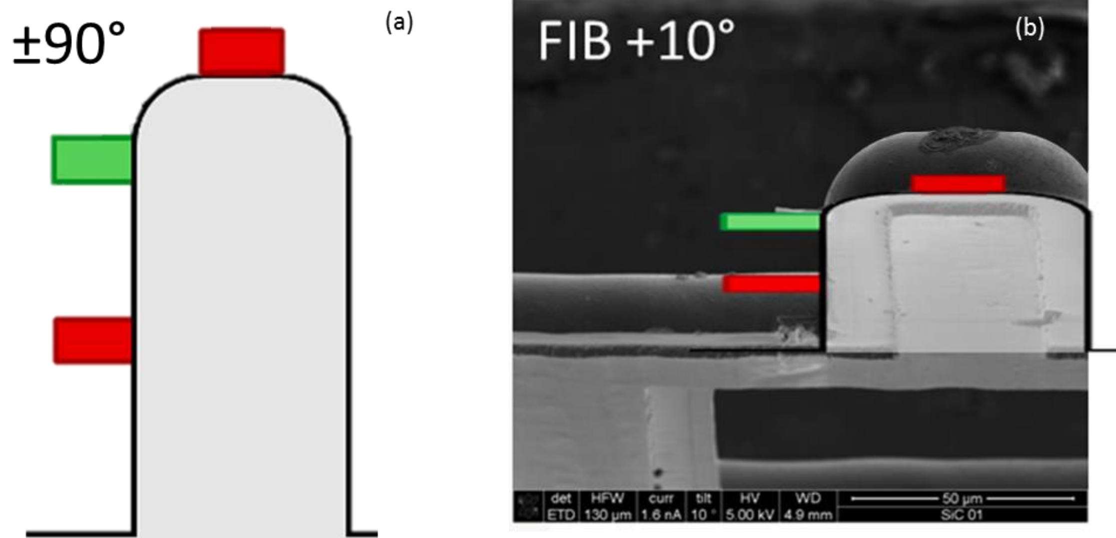

Figure 3-15: In (a) a scheme of the finger with samples on different fixation positions can be seen at a tilt of ±90°. (b) shows a FIB image with a tilt of ±10° overlapped by the scheme from (a) with the same tilt.

Figure 3-15 shows a scheme of the finger with different positions of the lamella at +90° and next to it a FIB image with a semi-transparent overlap by the same scheme for a tilt of +10° can be seen. The background of lamellae coloured in red the grid is in the path of the Ar^+ ions. Therefore, the restriction of setting the target window in a way that the ions, which miss the

sample, are shot in vacuum and not on the grid cannot be fulfilled. The situation of the green lamella is compatible with the requirements. However, the distance difference between the lamella and the grid for a ±10° tilt (see Figure 3-7) can significantly be reduced with a fixation of the lamella in the middle of the grid, as demonstrated in the scheme in figure Figure 3-16 (a) below.

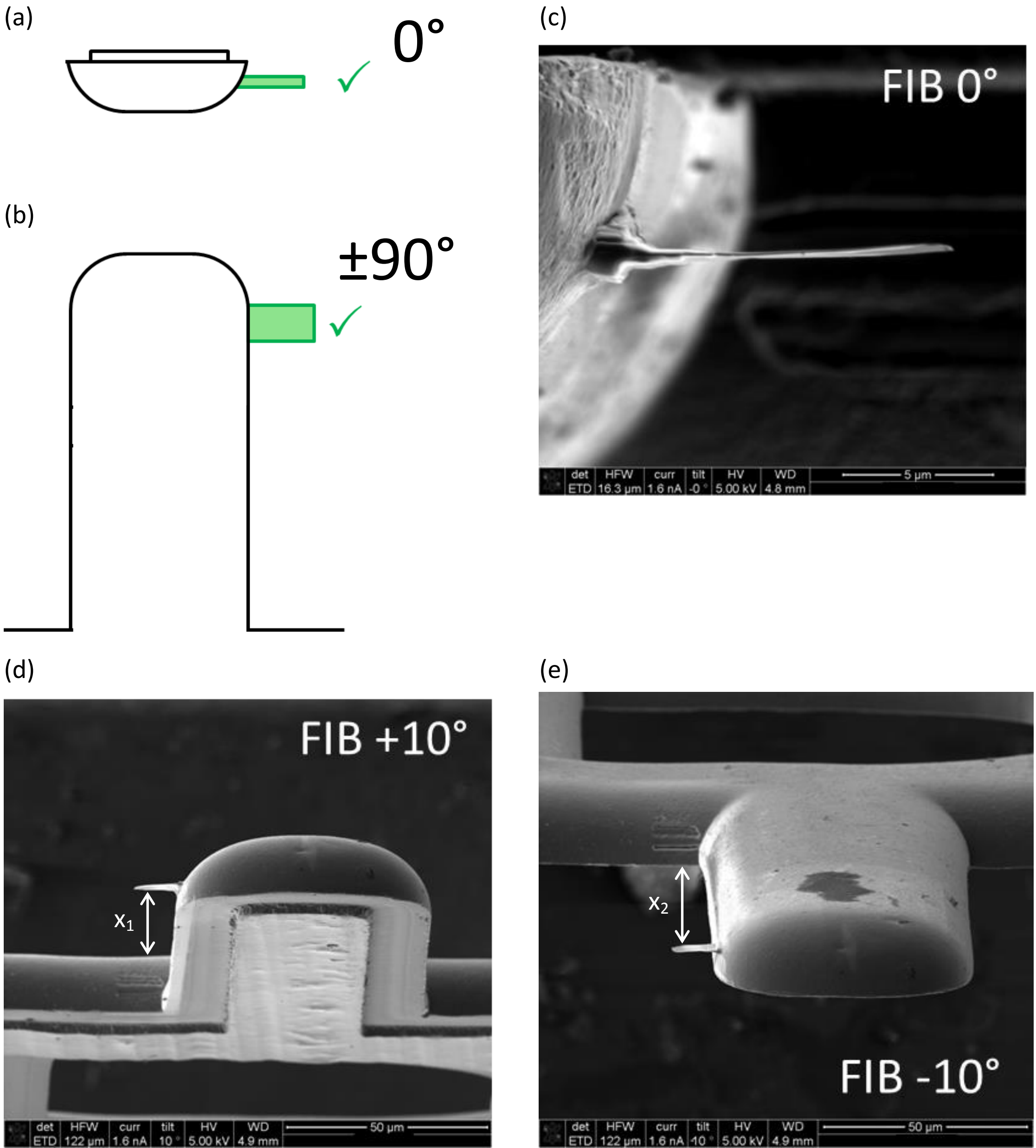

Figure 3-16: (a) and (b) show schemes for optimal lamella fixation. (c) FIB image of optimum position at 0°. (d) and (e) FIB images at ± tilt to demonstrate the enhanced distance difference between lamella and grid $x_1 \approx x_2$.

The image pair in Figure 3-7 has demonstrated the distance difference between lamella and grid (NanoMill® image) for a ±10° tilt and the **common fixation** (see Figure 3-14 (a)). For the ideal milling procedure, the sample should be milled on both sides without a transfer in between. However, for the common fixation the restriction for the position of the target

window cannot be fulfilled due to geometrical reasons and the blurriness of the NanoMill® image. The clear view on the lamella cannot be assured, therefore the sample must be unloaded, dismounted from the holder, turned upside down and clamped and transferred in again before milling the second side. This procedure is not only time-consuming, but also a damage-risk due to the additional mechanical claim during the loading process.

With the **adjusted configuration** in Figure 3-16 (FIB images) above the milling can be performed at a +10° and -10° without an additional transfer.

The top most position has proven to work very well, however the adjusted fixation in the middle of the finger is advisable (see Figure 3-16 (a) and (b)), because based on the similar distance of the lamella to the grid ($x_1 \approx x_2$) both sides can be milled without unloading and turning the sample.

3.3. Backside milling

The incoming flux of ions can be directed onto the FIB lamella via the Pt side, which is the conventional way of ion milling, or like illustrated in Figure 3-17 (b) from the other side, called backside milling. This approach can either be realised in the FIB, with certain adaptions of the lamella fixation and the clamping direction of the grid in the FIB holder or, with less effort, in the NanoMill®. In both cases the benefits, or more precisely the avoided disadvantages, are the same.

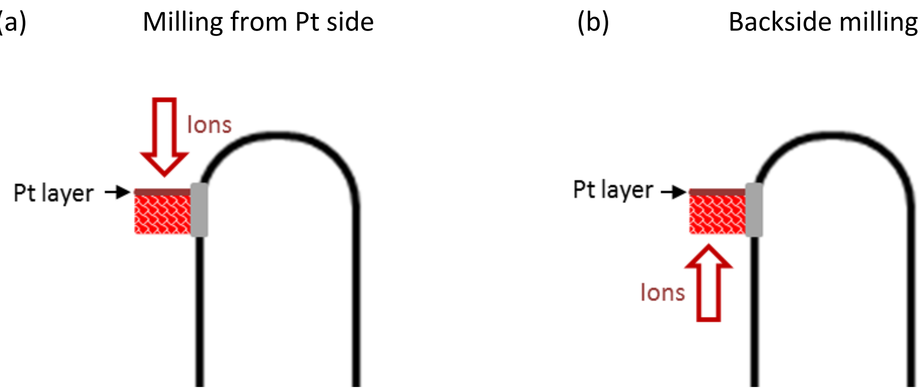

Figure 3-17: Scheme of (a) conventional milling and (b) backside milling.

Certain materials show an affinity for the re-deposition of sputtered Pt atoms. In such a case, backside milling would be advisable.

Further, any material transport in the direction of the ion beam can impede a clear view on an interface between two materials (see interface between A and B in Figure 3-18), and complicate the analysis, because it looks like diffusion of material A into material B, though it is a preparation artefact (smearing effect). Milling from the opposite side offers an efficient solution, because the material will be transported in the direction of the milling and therefore away from the interface of interest.

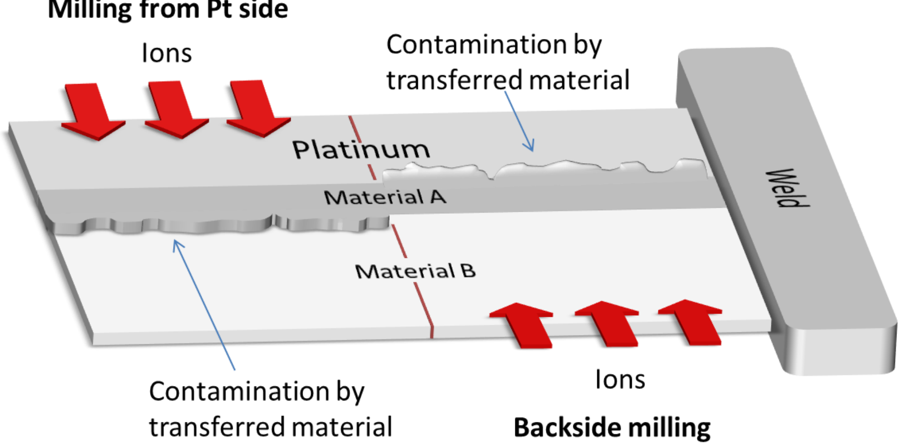

Figure 3-18: Schematic diagram showing the interface contamination of material A and B by material transfer.

Another effect occurring on the interface between materials with different chemical composition is preferential milling. Materials with low sputter rate, like material A in Figure 3-19, e.g. tungsten, are hardly milled and at the same time the neighbouring or surrounding material is removed rapidly by sputtering, which leads to a sample with an uneven surface/thickness. This is called curtaining effect and in contrast to most sputter artefacts it can even be worse at low kV. To avoid this effect, the milling direction of the FIB lamella should be revised [25].

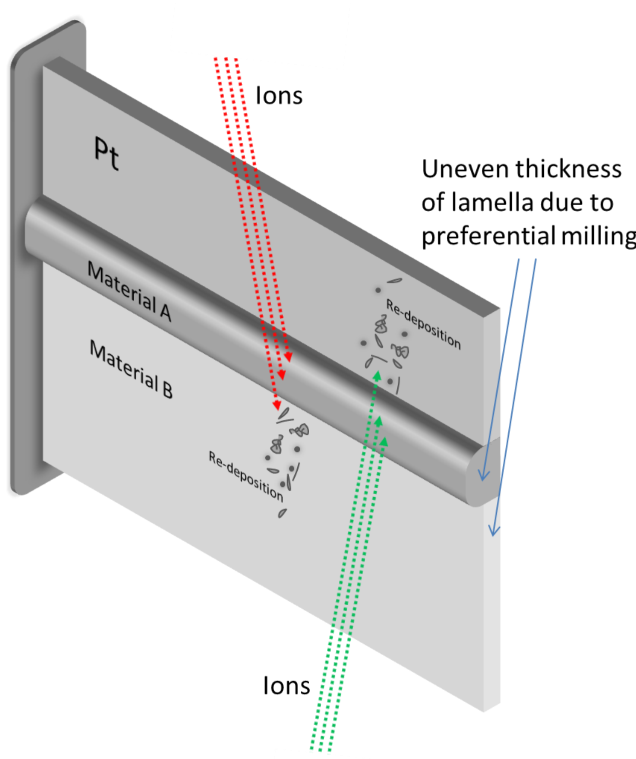

Figure 3-19: Scheme of preferential milling and re-deposition.

3.3.1. Information related to lamella fixation for FIB backside milling

The sample preparation in the FIB underlies the geometrical restrictions of the flange-mounted equipment (see Figure 2-2 (a)), which can be individual for every microscope. For backside milling with the Nova 200 NanoLab at the FELMI the FIB lamella needs to be fixed in top position, which has consequences on the post-treatment in the NanoMill®.

Requirement for milling in the FIB

Due to the mentioned geometry conditions the transfer grid needs to be modified to ensure an obstacle free path for the ions bombardment. The removal of the disturbing parts, indicated by the shaded areas in Figure 3-20 below, is a necessary procedure.

Requirement for post-treatment in the NanoMill® of backside milled FIB lamella

If the lamella is fixed in top position a cleaning in the NanoMill® is possible, if the grid is not clamped in the common way, but 90° rotated as demonstrated in Figure 3-20.

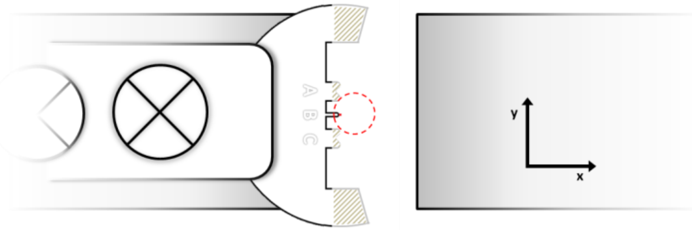

Figure 3-20: Position of modified grid in NanoMill® sample holder.

3.3.2. Backside milling in NanoMill®

For a commonly prepared FIB lamella a backside milling in the NanoMill® is possible, too, by an alternative grid positioning in the sample holder, called backside position. A scheme of backside milling can be seen in Figure 3-21 below.

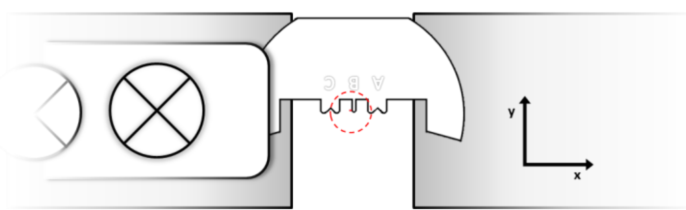

Figure 3-21: Scheme for backside milling.

Because of this alternative grid positioning the work and time consuming sample preparation for backside milling in the FIB is no longer necessary.

Requirement for FIB lamella preparation

A common way to stabilize the lamella is that not all of the material is removed during the rapid thinning step in the FIB as seen in the Figure 3-22 below. However, for a back side cleaning procedure in the NanoMill® with low voltage and an ion incident angle of 10° the plan-parallelism of the FIB lamella is a requirement, because the stabilizing material would be a barrier or at least an unwanted influence for the impinging ions.

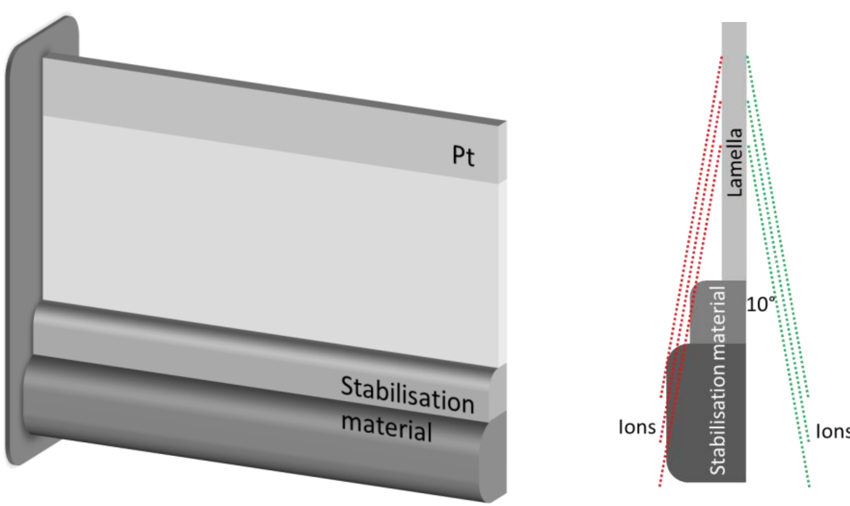

Figure 3-22: Schematic diagram of lamella with ions bombardment at an incident angle of 10°.

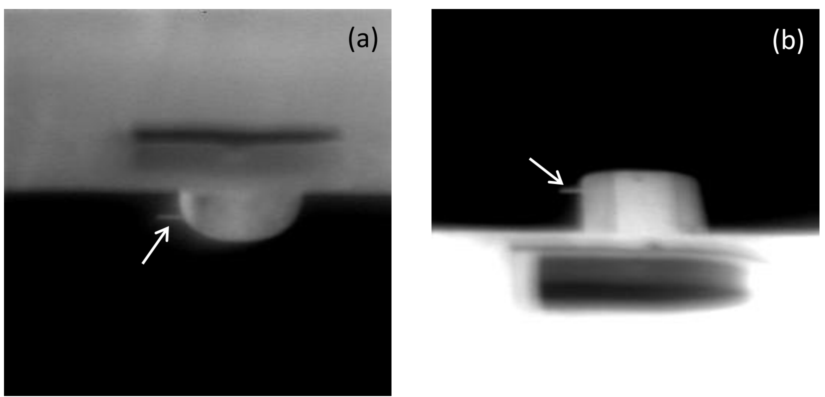

Figure 3-23: Images from the NanoMill® of backside clamped Omniprobe grid at (a) -10° and (b) +10° tilt angles. The white arrow indicates the position of the lamella.

3.4. Grid comparison

As mentioned above, milling the sample without hitting the grid is essential. To fulfil this requirement, the geometry of the grid is important. To a large extent Omniprobe Copper grids were used for the examination of this thesis. However, another grid type was used for sample preparation, which made the milling procedure at ±10° nearly impossible. Hence a detailed optical investigation concentrating on the grid differences was performed and is demonstrated in the following figures. Besides the Omniprobe Copper grid and an Omniprobe Molybdenum grid two EM-Tec grids (copper), one with 3 and another with 5 fingers were examined.

Table 3-1: Grid comparison in terms of the grid dimensions.

	Cu Omniprobe	Mo Omniprobe	Cu 3 EM-Tec	Cu 5 EM-Tec
grid size	3 mm	3 mm	3 mm	3 mm
overview				
fingers	2 wide M-shaped fingers 1 narrow finger	2 wide M-shaped fingers 1 narrow finger	2 wide M-shaped fingers (125 µm) 1 narrow finger (80 µm)	5 narrow fingers (70 µm)
length	190 µm	180 µm	200 µm	190 µm
thickness	25-30 µm	30 µm	30-40 µm	30-40 µm

As described in Section 3.2 the lamella should be fixed at the top most straight spot on the finger in “Flag” position. Compared to Omniprobe the EM-Tec fingers are thicker and show a bigger rounding, therefore the lamella is fixed further down which corresponds to a smaller distance to the grid and makes it harder to fulfil the milling constraints.

3.5. Design of the optimal grid for a post-treatment with the NanoMill®

Due to the problems encountered during the NanoMill® thinning and our experience gained from the practical tests, we were able to construct an optimal grid that meets the requirements during the FIB preparation and subsequent NanoMill® thinning (see Figure 3-24).

For the optimal grid design, the major requirement to fulfil is an adequate distance between sample and grid for a tilt of ±10° (or even below), which leads to a minimum value for the ratio between grid thickness and finger length, or more precisely the distance from the position of the sample on the finger to the bottom of the finger.

The sample should be within the red circle (see Figure 3-24 (a)), because for this section the conditions for NanoMill® milling and imaging is favourable. On the two fingers two samples per grid can be fixed. This can be useful for the TEM investigation of two samples without a transfer in between and furthermore preparation in the FIB and/or the NanoMill® can be conducted under identical condition.

The fingers should be in appropriate distance to ensure that the poor image quality in the NanoMill® would not deteriorate a clear view on the lamella on the neighbouring finger, but still within the red area due to the situation described above.

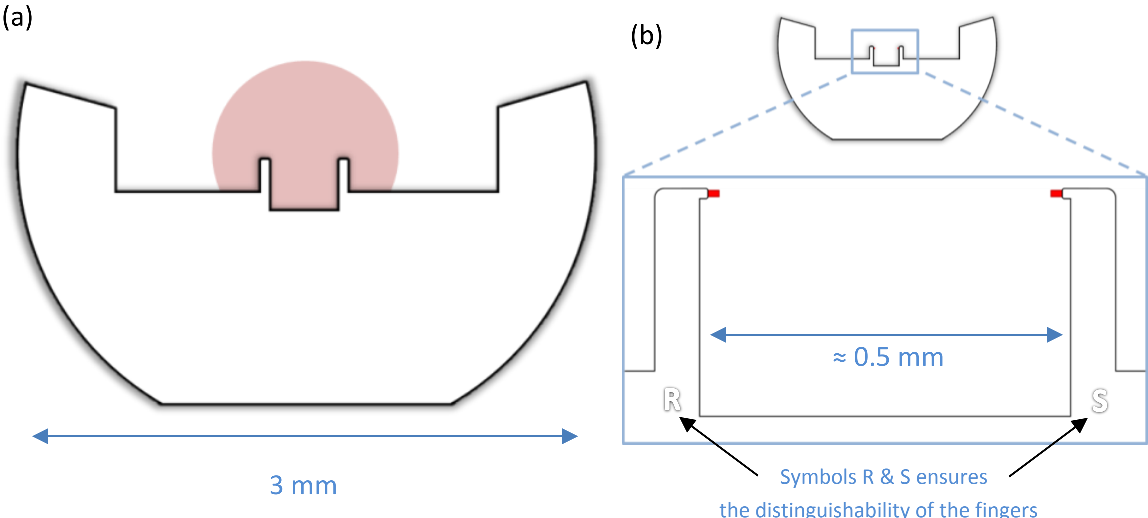

Figure 3-24: Schemes of the optimal grid for the milling process in the NanoMill®. (a) shows the whole grid. For the optimum milling and imaging the sample should be located within the red area. In (b) a magnification of the fingers can be seen.

The impact of the finger length on the distance between sample and grid can be seen in the schemes below. Though these sketches are two dimensional and therefore show no depth an obvious limitation by the length of the finger is recognisable. To even extend the distance and therefore ensure the space in between is big enough, a small adaption of the grid shape, more precisely an additional trench between the fingers, is advisable (see Figure 3-25 (c)).

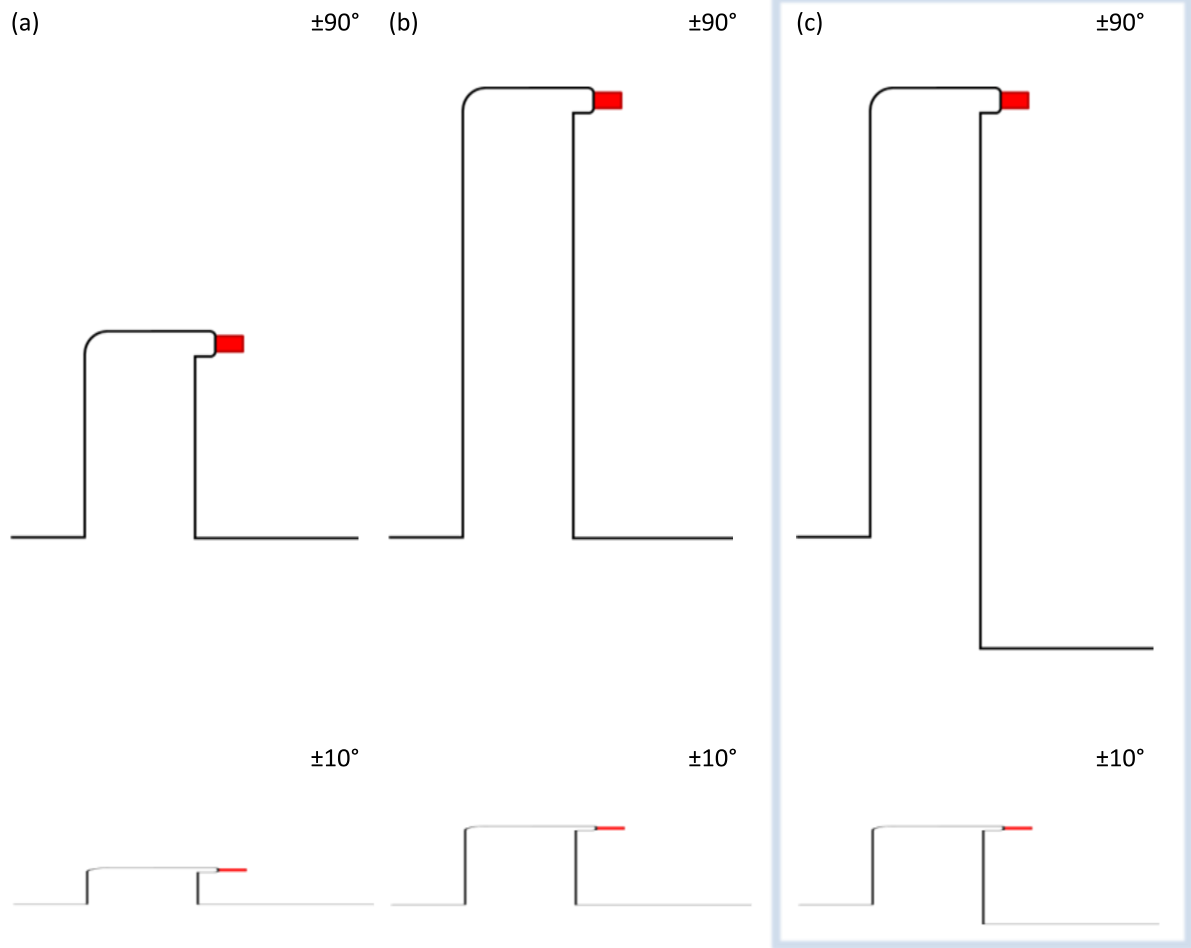

Figure 3-25: Fingers with different lengths and the resulting effect on the distance between lamella and grid. (a) Exaggerated short finger, which would not be possible for the NanoMill® procedure if it has actual thickness. (b) Regular length finger. (c) Additional trench for enhancing the milling by facilitating the milling conditions.

From the experience gained during the work on this thesis the recommended thickness-to-length ratio is about 6.5. However, the additional 'nose' on the top of the finger could have a positive influence on the milling performance, though it should not exceed a size of about 10 µm (see Figure 3-27 (a)). This size limitation results from the fact, that the signal from the grid could impair the sight on the lamella. By creating space, it should be easier to find and focus on the lamella.

With the considerations demonstrated in Figure 3-26 the geometrical requirements for the ideal milling process in the NanoMill® can be calculated with equation 3.1. The finger thickness d and the tilt angle α are assumed to be fixed. Ideally the distance g – between lamella and grid - should be at least 20 µm. The variable position of the lamella on the finger is indicated by the red point. It is crucial that the sample is located in the middle of the finger – at d/2 – to ensure the preservation of the symmetry for a tilt in ±α.

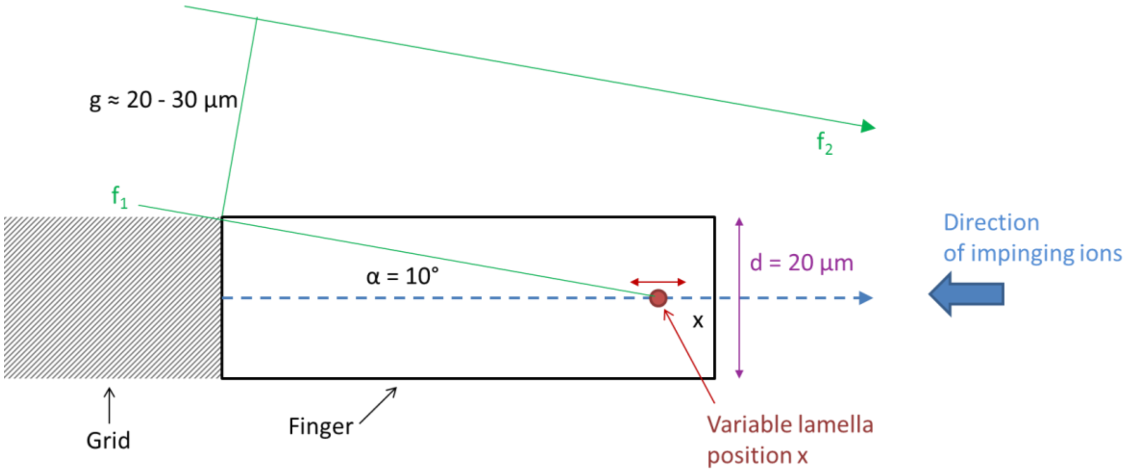

Figure 3-26: Scheme to find the minimum distance between lamella and grid at which milling is possible for a tilt angle of 10°.

From the figure above to following equation can by deduced:

$$x = \frac{d}{2 \cdot \tan \alpha} + \frac{g}{\sin \alpha} \tag{3.1}$$

d … thickness of the finger
α … tilt angle
g … distance between lamella and grid

Determination of distance x = 195 µm, which is at least required to fulfill the geometrical restriction. This length corresponds to the intersection of f2 with x in Figure 3-26.

Parameter	Value
d =	20 µm
α =	10°
g =	24 µm
x =	**195 µm**

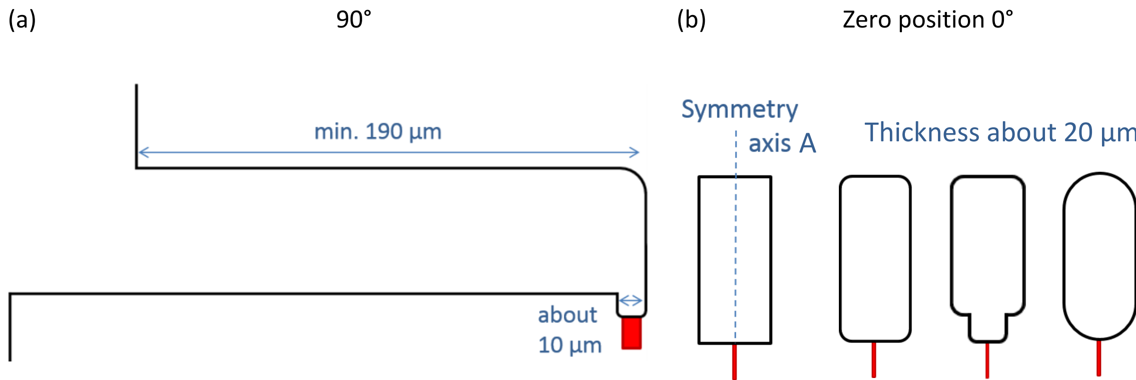

Figure 3-27: Schemes of the optimal grid for the milling process in the NanoMill®. (a) should demonstrate the dimensions of the finger. (b) Examples for the recommended shapes of the cross section.

Concerning the cross section of the grid there is one major point to consider. As found out during this work, it is favourable to fix the lamella in the middle of the finger, because this ensures, that the distance between lamella and grid is the same for a tilt in the positive and the negative direction. Therefore, the shape is secondary, but the symmetry around the axis A shown in the figure above is essential.

3.6. CM20 operation

A transmission electron microscope, a Philips CM20 equipped with a Gatan 678 Imaging Filter (GIF) filter and the software Gatan Digital Micrograph, is used for visual inspection of the sample and to measure the thickness at the samples.

A GIF is used for the acquisition of EELS and energy-filtered images. It is located below the TEM column after the fluorescence screen (see Figure 3-28), which must be lifted up, so that the electrons can enter the GIF. It consists of a magnetic prism, which disperses the electrons with respect to their energy to obtain an EEL spectrum, and of an optical column, which can be used to select an energy range by inserting a slit at the dispersion plane. Only electrons with certain energy values can pass the slit and are used for creating the image recorded with a CCD camera located at the end of the GIF [2, p. 681].

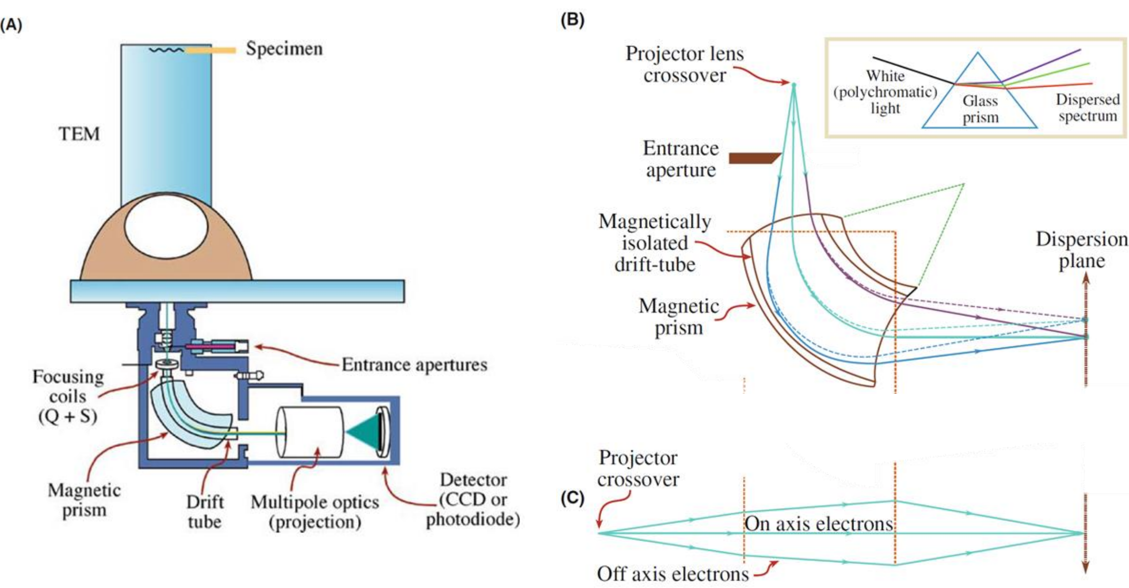

Figure 3-28: (a) Scheme of GIF located below the viewing screen. (b) Ray path through magnetic prism spectrometer showing the different dispersion and focusing of the zero-loss and energy-loss electrons in the image (dispersion) plane of the spectrometer. The inset shows the analogy with the dispersion of white light by a glass prism. (c) The lens action in the plane normal to the spectrometer. Image from [2, p. 682].

During the work with the CM20, characteristics of the double tilt sample holder come up, which are important for the iterative sputter rate determination: The position of the transfer grid in the sample holder of the CM20 is not fixed. For standard investigations, it generally does not matter that the lamella orientation differs from the previous examination, but due to the repetitive thickness measurements and the visual inspections of the lamella after every milling step the shift between the resulting image series are connected with a time-consuming image alignment. This drift correction is a mandatory condition for the analysis and will be described in the following chapter.

The α- and β-tilt of the CM20 double tilt holder gives the opportunity of orientating the sample. Why the alignment of the sample if of such a great importance can be derived from the following figure.

Figure 3-29: Double tilt sample holder of CM20.

Due to imaging conditions of the GIF it is not possible to fit the whole lamella on the CCD. As a consequence, BF and ZL images must be recorded in a two-step image series as demonstrated in Figure 3-30 below in order to be able to image the whole lamella.

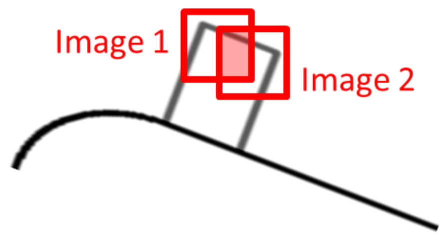

Figure 3-30: Schematic diagram of image acquisition in TEM CM20.

All images recorded with the CM20 are acquired with the following parameters.

Imaging Parameters of TEM CM20

Acceleration voltage	200 keV
C2 aperture	200 µm diameter
Objective aperture	20 µm diameter collection angle β: 3.63 mrad
Slit size (EFTEM)	10 eV

As mentioned the grids were positioned as similar as possible for every recording. Further, the silicon carbide samples were orientated in a zone axis. Lead zirconate titanate examinations were performed at the zero position.

3.7. Analysis of the TEM images with Digital Micrograph

The analysis is performed with the software Digital Micrograph provided by Gatan. As mentioned the iterative sputter rate determination of measuring thickness and milling leads to a series of images. These have to be converted into t/λ maps (see Chapter 2.5.1), which show the relative thickness and must be aligned, before a thickness comparison of a certain area at different sputter times can be done. Only small regions of the lamella can be compared, because diffraction contours appear as the thickness of the sample decreases.

t/λ map

In Digital Micrograph, relative thickness maps are created from a BF and a ZL-filtered TEM image (see Chapter 2.5.1) with the tool 'Compute Thickness Map'.

Alignment

The aim of measuring the decrease in thickness at exactly the same position after every milling step is impossible without an alignment of the image series. The misalignment occurs due the flaw of an uncertain sample position in the TEM holder which results in a rotation between images of different sputter time. Furthermore, a shift in x- and y-direction, due to different stage positions, is noticeable. Therefore, it is a necessity to correct the varying alignment of the images. The alignment procedure starts with a manual correction of the rotation followed by an x- and y-shift correction. The automatic alignment for the x- and y-shift works well, if the pictures show characteristic details. However, by reducing the sample thickness more and more thickness fringes occur, which make an automatic alignment impossible. Therefore, also a manual alignment of the x- and y-shift is advisable. The function 'Image Alignment' is employed to manually correct the x- and y-shift and creates a new image showing the overlap. The work steps of the alignment can be seen in the Figure below.

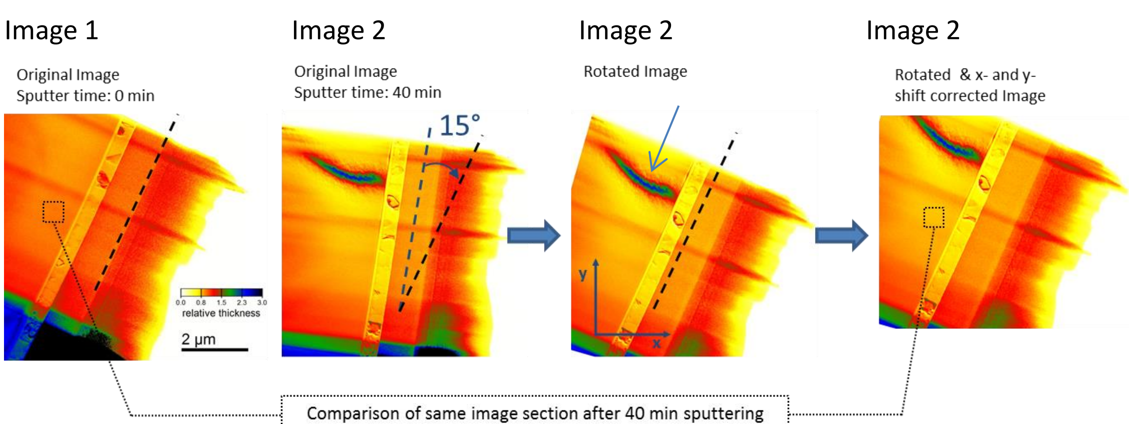

Figure 3-31: Demonstration of image alignment steps. A series of all aligned images of SiC can be seen in in .

It is crucial to perform this alignment, because small local deviations in the t/λ map have a big influence on the result.

After the alignment of the relative thickness map series a homogenously looking area, which can be found in all of these images, can be chosen to measure the thickness decrease with increasing sputter time. For example, the elongated spot in Figure 3-31 (40 min sputter time, arrow) above or thickness fringes make it impossible to use this region for consecutive thickness measurements. Crystalline samples, like seen in the image above, show large areas of uniform thickness. Therefore, large regions can be used for the thickness determination. By contrast, the grain structure of polycrystalline material (see Figure 3-50) leads to an inhomogeneously looking t/λ map, which makes it difficult to find adequate areas, especially for an increasing number of images. A more precise description of the measurement areas, including size differences and accurate position, will be discussed in the associated section below.

3.8. Materials

In this chapter the exact conduct of the examination and procedure of two materials, silicon carbide (SiC) and lead zirconate titanate (in the following chapters also referred to as PZT or 'ceramic' due to the nature of the sample) will be described. These materials are part of the Austrian Research Promotion Agency FFG (project 850220). The sections contain all investigations of the respective materials and will be opened with some basic information followed by the iterative thickness reduction and the resulting milling rate. Furthermore, a thickness determination via a Double Cross Section is performed for both materials. Additionally, for silicon carbide the MFP is determined by an experiment with a needle shaped TEM sample.

The lamellae as well as the Double Cross Section are prepared with the FIB as described in the theory part of this thesis (see Chapter 2.2). The imaging parameters, for the transmission electron microscope CM20, are listed on page 47 and the milling parameters of the NanoMill® on page 25. All examinations were conducted with these settings.

Literature research

To get a feeling for milling parameters and sputter rates a literature research was a starting point. However, for the materials and the parameters (Ar^+, 900 eV, ±10°) used in this thesis any systematic studies for sputter rates exist. For SiC data for different parameters are found and listed below. For PZT no milling information could be found.

The information about the commonly used standard material in material science, namely crystalline Si[1] is given by the manufacturer of the NanoMill® and further data from literature about Si and SiC can be seen in Table 3-1 below. However, crucial information like the incident angle is missing in the literature or the sputter rate determination has been performed at an incident angle of 90°, which is often used as standard condition, but is not appropriate for the post-treatment with the NanoMill®. Due to the difference in the milling parameters of the research data, respectively the varying acceleration voltage of the Ar^+ ions as well as the incident angle of the projectiles, a comparison is hardly possible.

Table 3-1: Sputter rates from literature

Material	Ion type	Sputter rate Å/min	Incident angle	Ion energy	Source
Si[1]	Ar^+	10	30°	900 eV	[7, p. 9]
Si	Ar^+	4800	-	600 eV	[26]
SiC	Ar^+	3000	-	600 eV	[26]
SiC	Ar^+	320	90°	500 eV	[27, p. 6]

[1] Additional information concerning the milling condition: 10 x 10 µm² target window size, room temperature, 200 pA ion beam current.

3.8.1. Silicon carbide

General information

Silicon carbide is a compound of silicon and carbon. It naturally occurs in meteorites to a very small extend and was accidently synthesized in 1890 by Edward G. Acheson, who sent current through a mixture of clay and carbon, with the intension to synthesize diamonds. For SiC numerous polytypes exist, although only a few occur frequently. All structures can be built up by stacking layers of Si and C as demonstrated for 2H, 3C, 4H and 6H in Figure 3-32 (a) below. In every stacking configuration, the Si atoms are linked covalently to four C atoms. Therefore, the structures can also be achieved by packing silicon-carbon tetrahedrons as demonstrated in Figure 3-32 (b). 6H-SiC, one of the most common polytypes, will be investigated in this work.

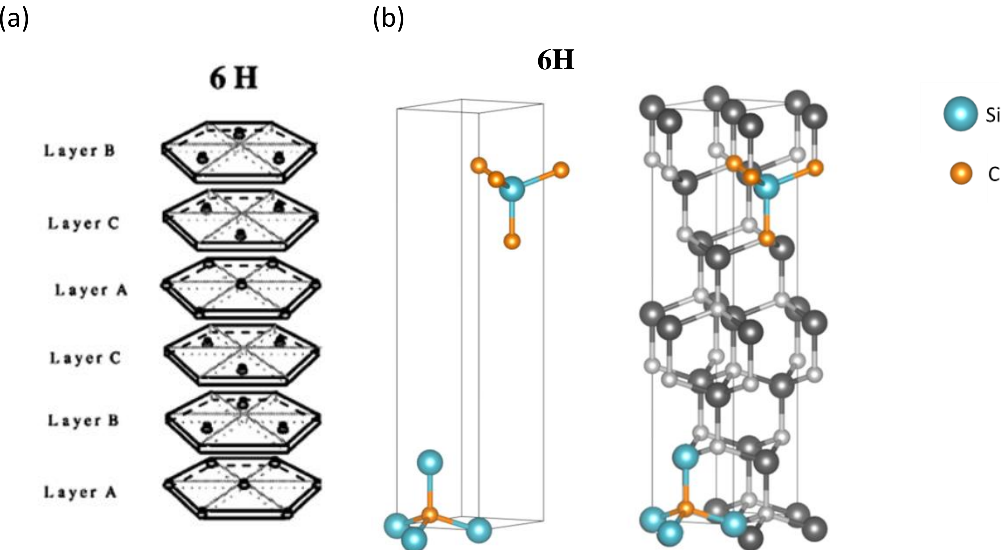

Figure 3-32: (a) Illustration of the stacking of successive layers of Si and C to represent the polytype 6H of SiC. Image modified from [28]. (b) VESTA unit cell structure models.

Lamella position for sputter rate determination
Two SiC FIB lamellae are fixed on separate grids in flag-position.

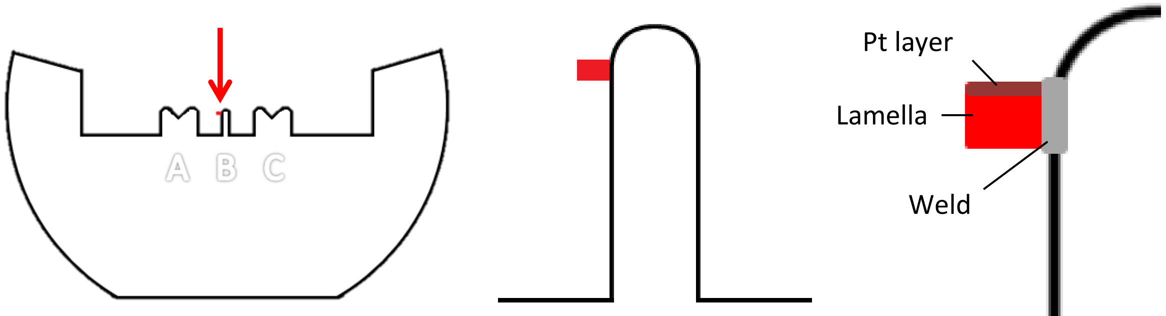

Figure 3-33: Schemes to demonstrate the position of the lamella on the grid and the position of the lamella on the finger. The red arrow indicates the position of the lamella.

Examination after FIB preparation to specify the start condition for the NanoMill® post-treatment
The starting thicknesses of the two lamellae slightly differ after the procedure in the FIB. The first SiC sample, hereinafter referred to by the abbreviation SiC 1, has a relative starting thickness of about 0.89 MFP. This t/λ value corresponds to an absolute thickness of about 150 nm. The MFP calculation, to convert relative to absolute thickness values, was performed as described on Page 17. The second sample, referred to as SiC 2, has a starting thickness of about 0.57 MFP, which is equivalent to about 95 nm. Due to different initial sample thicknesses varying post-treatments are executed.

	SiC 1	**SiC 2**
Relative starting thickness	0.89 MFP	0.57 MFP
Absolute starting thickness[2]	150 nm	95 nm

3.8.1.1. Repetitive thinning with NanoMill® and monitoring with TEM CM20

The sputter behaviour at SiC can be found by an iterative process of measuring the thickness of the sample in the TEM CM20 and reducing the sample thickness in the NanoMill®. The milling is performed at a source energy of 900 eV, a beam current of 100 pA and a tilt of ±10°. By plotting the thickness against the sputter time the sputter rate can be determined.

[2] λ_{sic} = 167.7 nm. CM20 (E_0= 200 keV, β = 3.63 mrad)

For SiC 1 five iterations of thickness measurements and milling are performed. Therefore, the SiC lamella has been transferred into the NanoMill® four times (for 20 min, 10 min, 10 min and 10 min per side), which sum up to a total milling time of 100 min.

Due to the smaller initial thickness and an unclear view of the lamella for a tilt of -10° during the second milling step, SiC 2 is only thinned two times (for 10 min per side, 10 min only +10° side), which results in 30 min total sputtering time. A possible reason for the uncertain image in the NanoMill® is found during the thickness determination in the CM20 and later monitored in the FIB (see Figure 3-34). On the fluorescence screen at the CM20 a flexible piece attached to the lamella can be seen as it flutters in the illumination of the electron beam till it moves under the finger and sticks there. This may be an artefact of the NanoMill® though it did not occur a second time.

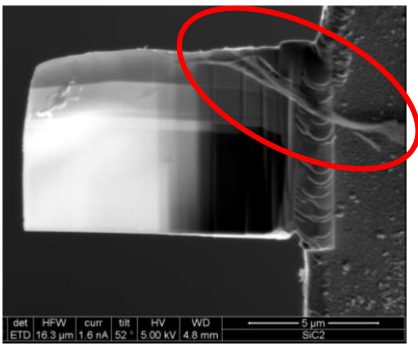

Figure 3-34: FIB image of scraps on SiC 2 after TEM investigation.

The half sputtering time of SiC 2 allows to conclude, that the thickness reduction is half as much as for SiC 1.

	SiC 1	SiC 2
Iterations	5	3
Total milling time	100 min	30 min

The presentation of the acquired data (Table 3-1) and the image analysis follows separately for SiC 1 and SiC 2 in the respective chapters. However, the visual progress of the thickness decrease in the t/λ maps will only be shown once.

Representative for all milling series, the complete t/λ map series of the 4 thinning steps of SiC 1 with a total sputter time of 100 min can be seen in Figure 3-35 below. The t/λ maps are created from a BF and a ZL-filtered TEM image as described in Chapter 2.5.1 and show the left and right section of one lamella. The limit should be selected in a way that the decreasing thickness is visible with the naked eye.

Because of the random appearance of diffraction contours the t/λ map series should be completed before the decision on the measurement area is made.

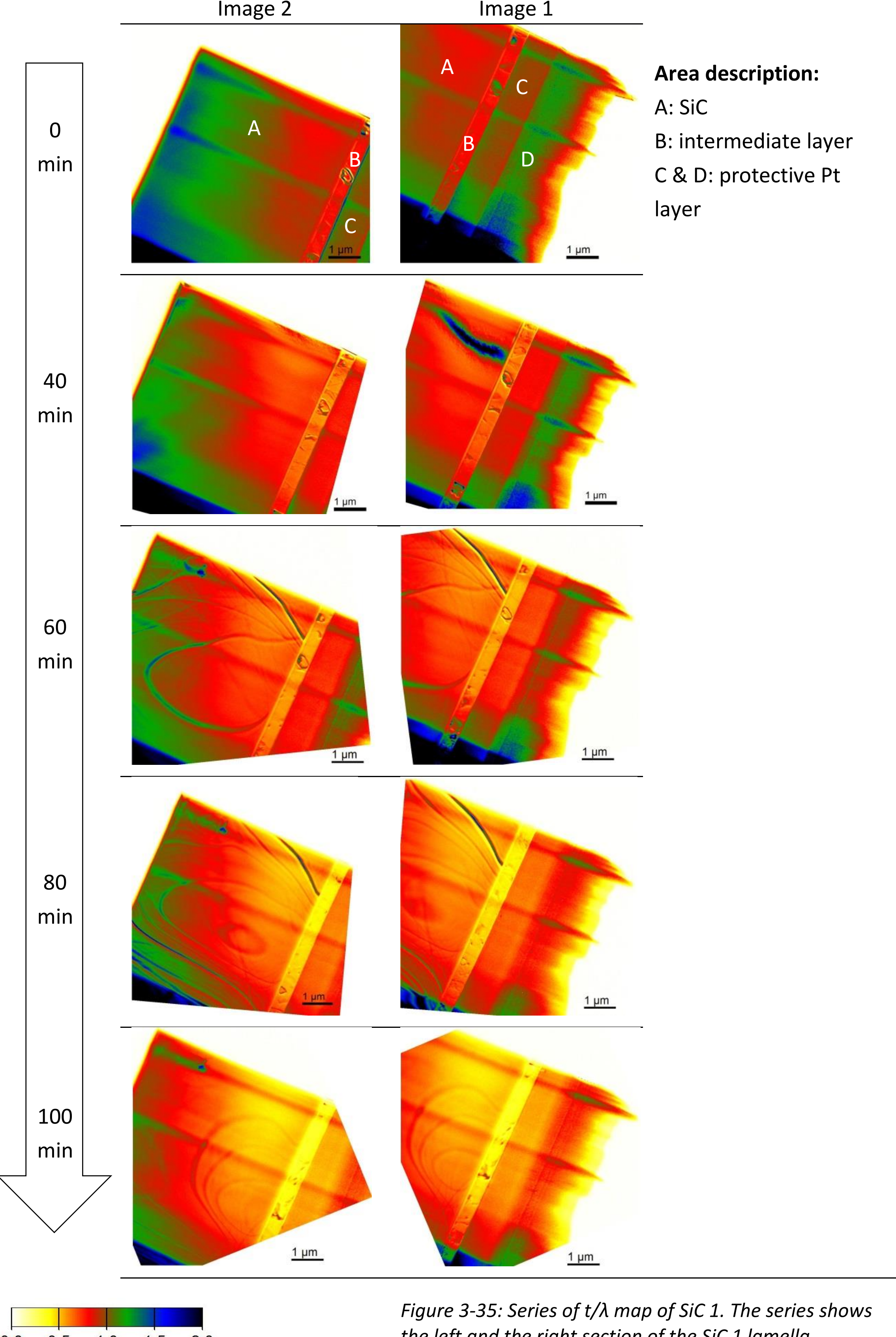

Area description:
A: SiC
B: intermediate layer
C & D: protective Pt layer

Figure 3-35: Series of t/λ map of SiC 1. The series shows the left and the right section of the SiC 1 lamella.

3.8.1.2. Thickness analysis with Digital Micrograph

After the acquisition and the alignment of the whole t/λ map series the mean value of the relative thickness can be measured in certain areas. Consequently, striation from the curtaining effect and regions with fringes, which appear as the sample gets thinner, should be avoided.

For every sputter step four TEM images are acquired and two t/λ maps are calculated. The areas for the relative thickness measurement are chosen in the overlapping section.

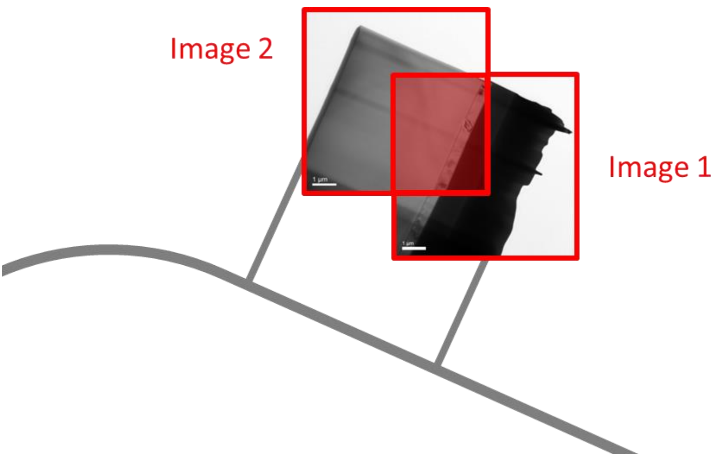

Figure 3-36: Demonstration of image acquisition in TEM CM20.

SiC 1

In Area 1 and Area 2, which both have the size of 0.47 x 0.47 μm^2 for each sputter step, a formation of the mean relative thickness value has been performed for increasing sputter times. These measurement areas can be seen in Figure 3-37 below and the data is listed in Table 3-1. Because it is necessary to position the measurement window on a sample area were no diffraction contours - which randomly appear - are present, they were chosen after looking at the t/λ map series in Figure 3-35.

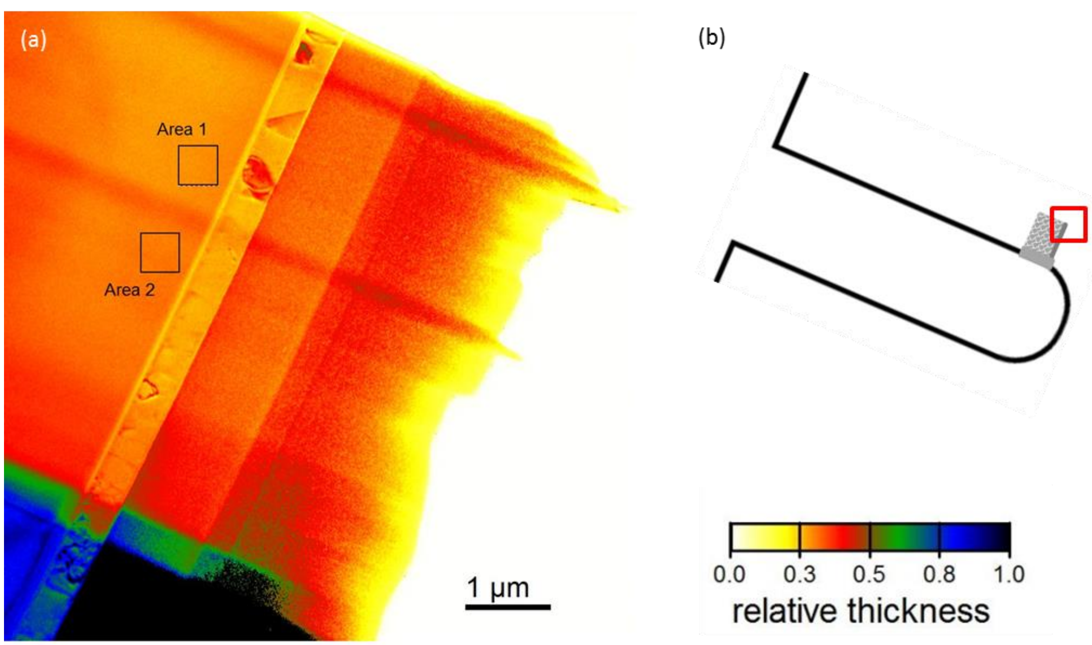

Figure 3-37: (a) shows a t/λ thickness map (SiC 1, 0 min sputter time). (b) Overview of finger with lamella. The red marker indicates the section of the lamella seen in (a).

Relative and absolute thickness

Area 1

Table 3-1: relative and absolute[3] thickness of SiC 1 Area 1 for increasing sputter times. The error in this and following tables is given by the standard deviation.
s… sputter time
r… relative thickness / MFP
t… absolute thickness / nm

	Image 1	**Image 2**	**Image 1**	**Image 2**
s/min	r/MFP	r/MFP	t/nm	t/nm
0	0.86 ± 0.02	0.87 ± 0.02	145 ± 3	145 ± 3
40	0.68 ± 0.02	0.70 ± 0.01	115 ± 3	118 ± 2
60	0.64 ± 0.02	0.66 ± 0.01	107 ± 3	110 ± 2
80	0.56 ± 0.02	0.56 ± 0.02	94 ± 3	94 ± 3
100	0.50 ± 0.01	0.50 ± 0.01	84 ± 2	84 ± 2

[3] λ_{SiC} = 167.7 nm. CM20 (E_0= 200 keV, β = 3.63 mrad)

Area 2

Table 3-2: Relative and absolute[4] thickness of SiC 1 Area 2 for increasing sputter times.
s… sputter time
r… relative thickness / MFP
t… absolute thickness / nm

	Image 1	**Image 2**	**Image 1**	**Image 2**
s/min	r/MFP	r/MFP	t/nm	t/nm
0	0.92 ± 0.02	0.90 ± 0.02	154 ± 3	151 ± 3
40	0.74 ± 0.01	0.76 ± 0.01	124 ± 2	127 ± 2
60	0.68 ± 0.01	0.71 ± 0.01	115 ± 2	119 ± 2
80	0.61 ± 0.01	0.61 ± 0.01	103 ± 2	102 ± 2
100	0.56 ± 0.02	0.56 ± 0.02	94 ± 3	94 ± 3

In Figure 3-38 the relative thickness data from Table 3-1 and Table 3-2 is plotted against the sputter time.

[4] λ_{sic} = 167.7 nm. CM20 (E_0= 200 keV, β = 3.63 mrad)

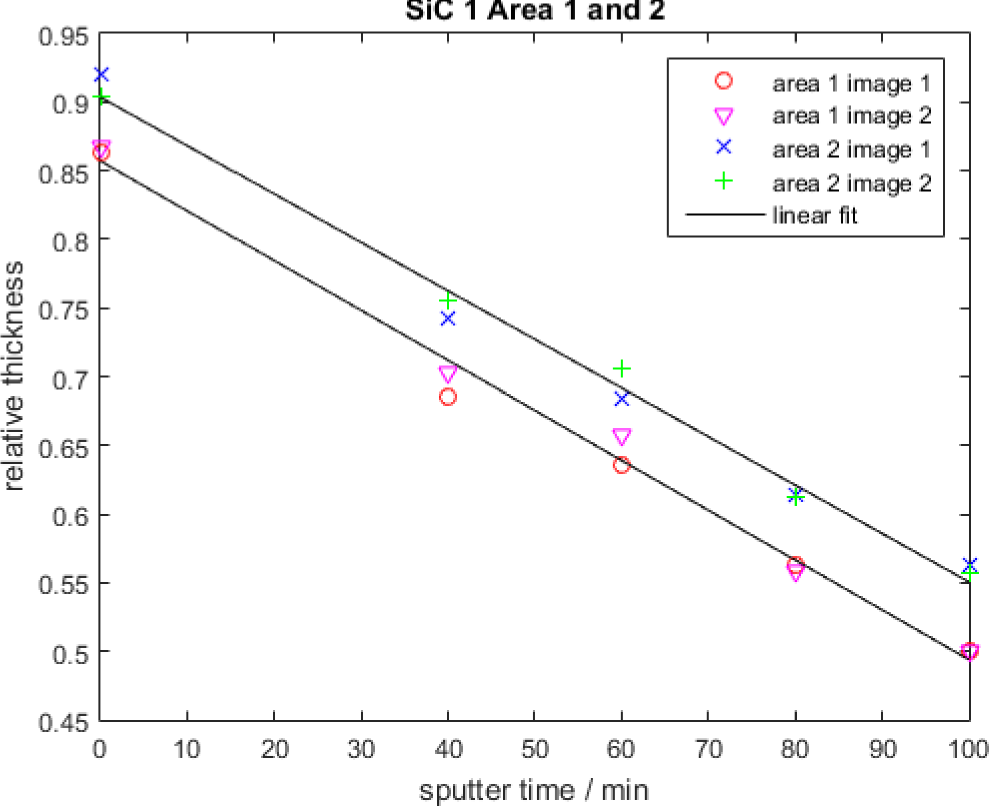

Figure 3-38: Relative thickness reduction vs. milling time of SiC 1.

SiC 2

In Area 1 (0.47 x 0.47 μm^2) and Area 2 the relative thickness is averaged for increasing sputter times. These measurement areas can be seen in Figure 3-39 below and the data is listed in Table 3-3. To convert the measured t/λ values in absolute thickness the theoretical MFP values from Table 2-1 are used.

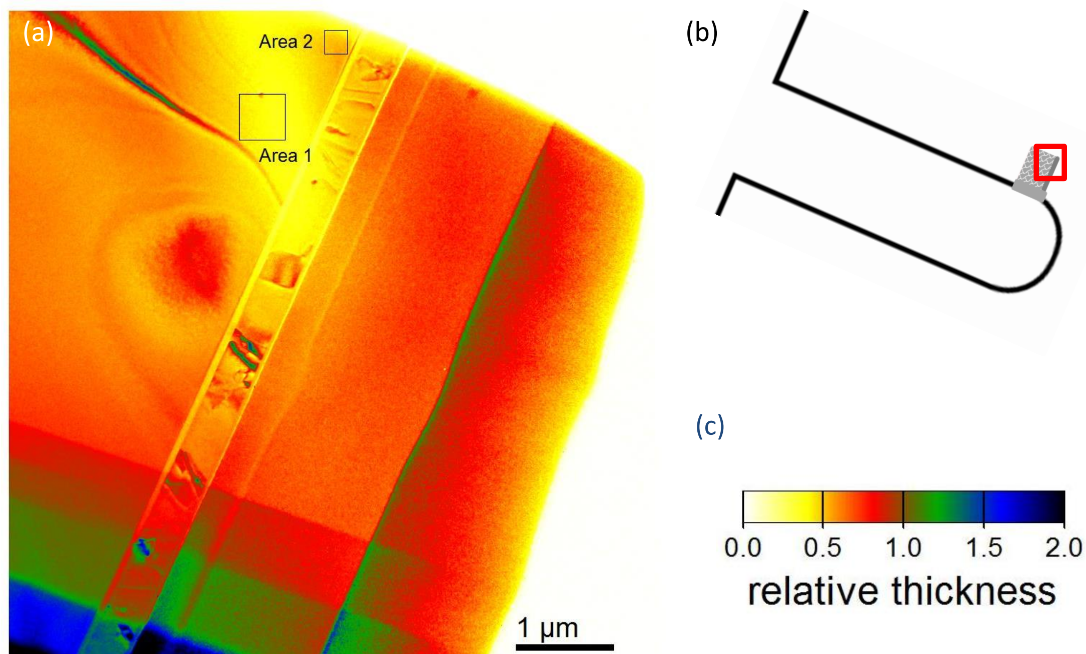

Figure 3-39: (a) shows a detail of a t/λ thickness map of SiC 2. (b) Overview of finger with lamella. The red marker indicates the section of the lamella seen in (a). (c) Contrast limit.

Relative and absolute thickness

Area 1

Table 3-3: Relative and absolute[5] thickness of SiC 2 lamella for increasing sputter times.

s… sputter time

r… relative thickness / MFP

t… absolute thickness / nm

	Image 1	Image 2	Image 1	Image 2
s/min	r/MFP	r/MFP	t/nm	t/nm
0	0.48 ± 0.06	0.50 ± 0.04	81 ± 10	84 ± 7
20	0.40 ± 0.03	0.41 ± 0.03	67 ± 5	68 ± 5
30	0.36 ± 0.03	0.34 ± 0.03	58 ± 5	61 ± 5

[5] λ_{SiC} = 167.7 nm. CM20 (E_0= 200 keV, β = 3.63 mrad)

Area 2

Table 3-4: Relative and absolute[6] thickness of SiC 2 lamella for increasing sputter times.
s… sputter time
r… relative thickness / MFP
t… absolute thickness / nm

	Image 1	Image 2	Image 1	Image 2
s/min	r/MFP	r/MFP	t /nm	t /nm
0	0.65 ± 0.02	0.67 ± 0.02	109 ± 3	112 ± 3
20	0.59 ± 0.01	0.60 ± 0.02	99 ± 2	101 ± 3
30	0.52 ± 0.02	0.56 ± 0.02	95 ± 3	94 ± 3

In Figure 3-40 the relative thickness data from Table 3-3 and Table 3-4 is plotted against the sputter time.

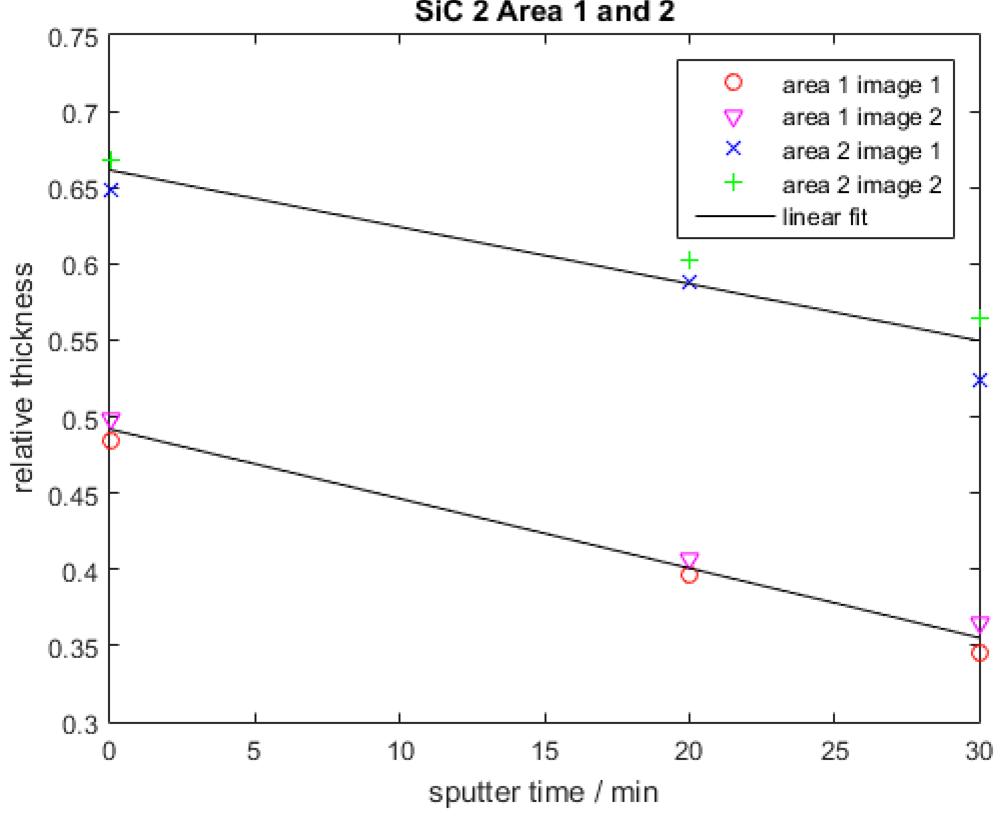

Figure 3-40: Relative thickness reduction vs. milling time of SiC 2.

[6] λ_{SiC} = 167.7 nm. CM20 (E_0= 200 keV, β = 3.63 mrad)

3.8.1.3. Sputter rate determination

To acquire the sputter rate of SiC the data points of both samples need to be linearly fitted as already seen for SiC 1 and SiC 2 above, though for reasons of easier comparison the information of both samples is plotted side by side in Figure 3-41.

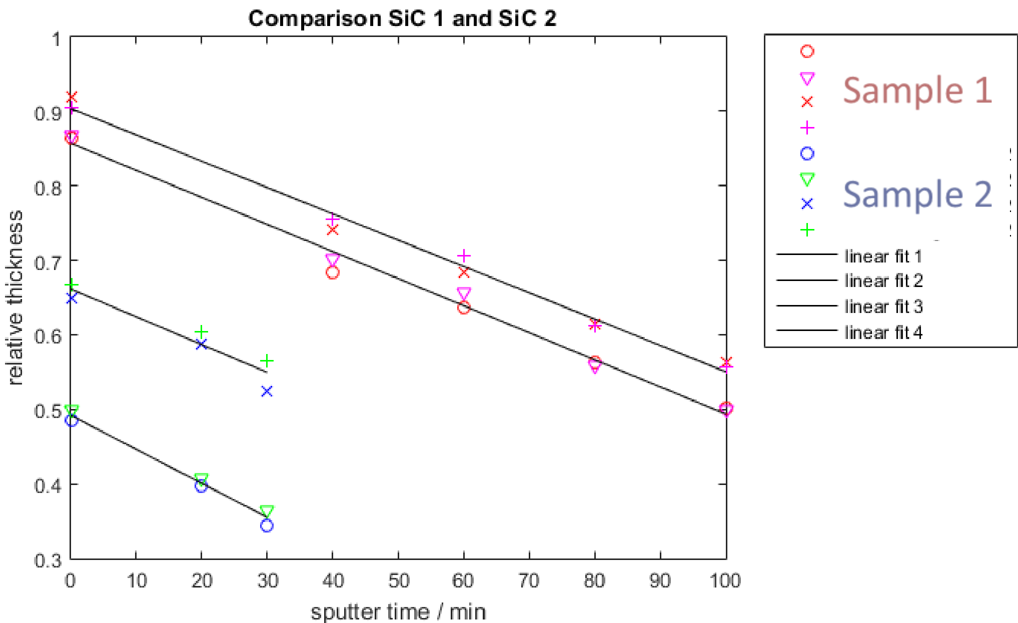

Figure 3-41: Comparison of relative thickness reduction of SiC 1 and SiC 2.

From the slope of the four fits a mean sputter rate can be calculated.

Table 3-5: Sputter rate of SiC 1 and SiC 2

	Sputter rate MFP/min	**Sputter rate Å/min**
Fit 1	$(3.52 \pm 0.15)\ 10^{-3}$	5.9 ± 0.3
Fit 2	$(3.63 \pm 0.13)\ 10^{-3}$	6.1 ± 0.2
Fit 3	$(3.72 \pm 0.04)\ 10^{-3}$	6.2 ± 0.1
Fit 4	$(4.55 \pm 0.14)\ 10^{-3}$	7.7 ± 0.2

Table 3-6: Mean sputter rate

Mean sputter rate	
$(3.9 \pm 0.2)\ 10^{-3}$	MFP/min
6.5 ± 0.3	Å/min
39 ± 2	nm/h

RThe sputter rate calculated from fit 4 differs from the other 3 results. A explanation for this deviation can be, that the measurement are was too close to a diffraction contour.

3.8.1.4. Double Cross Section of SiC 2

To determined thickness of SiC 2 a DCS is performed. With this thickness and the t/λ map information of the same region the MFP can be calculated. In Figure 3-42 the lamella SiC 2 can be seen after the repetitive thinning. Furthermore, this figure demonstrates that the slice of

the DCS should be within one of the areas in which the relative thickness was measured. Only when this condition is fulfilled a direct comparison with the t/λ method is possible. Because measurement area 2 is too close to the edge of the lamella for a DCS preparation, the plane through area 1 is selected. Figure 3-44 (b) show images from the FIB preparation.

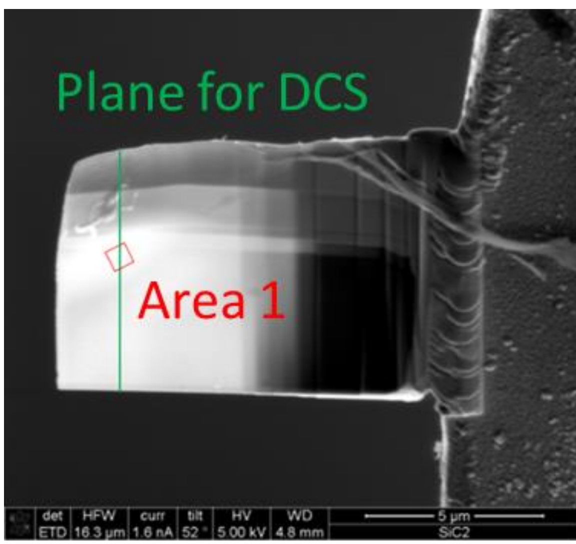

Figure 3-42: FIB image of DCS preparation showing the intact lamella.

To analyse the DCS thickness of SiC 2 TEM images (TF20, see Figure 3-43 (a)) and ADF images (Titan, see Figure 3-43 (b)) are recorded of the area of interest. The TEM image certifies the size of the crystalline part and reveals two amorphous layers on each side. However, in the ADF image an additional layer is disclosed, which lead to an elemental investigation with spectrum images.

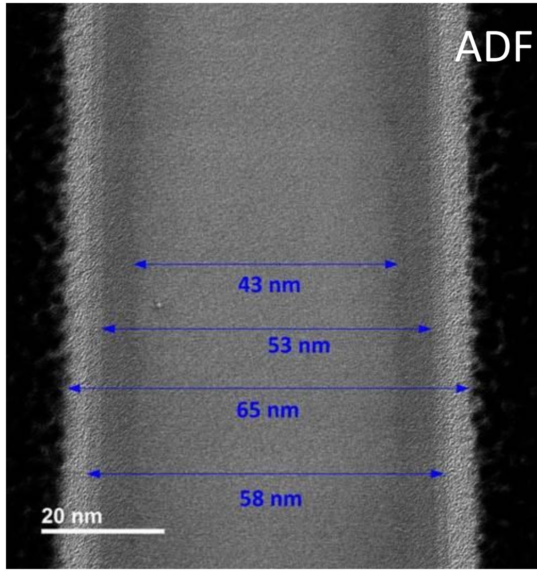

Figure 3-43: TEM image (b) The ADF image of the DCS of SiC sample 2.

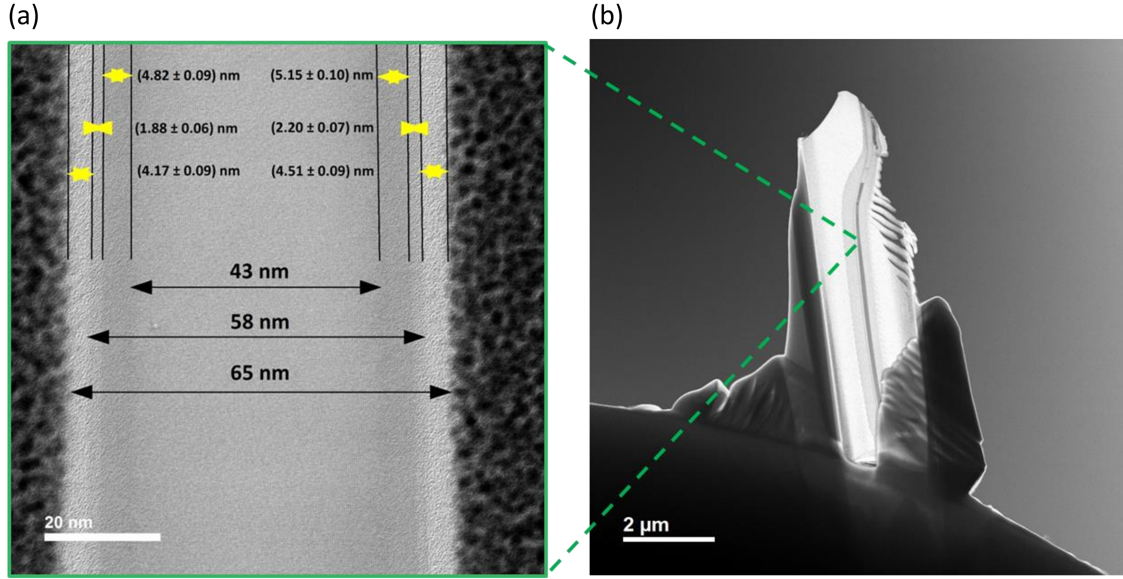

Figure 3-44: (a) Detailed thickness determination of DCS. (BF image) (b) Overview of DCS thinned to electron transparency.

It turns out, that the crystalline part has a thickness of 43 nm. However, in the t/λ method the whole sample, including the amorphous outer layers of the lamella, contribute to the thickness measurement. Consequently, an examination of these layers is required, to clarify, if they have to be taken into account in the comparison with the t/λ method achieved thickness or if they are caused by the DCS preparation.

Examination of outer layers

By revealing the chemical composition of the layers their origin can be examined. Hence spectrum images from layer system are acquired with special interest on the silicon, oxygen and carbon content. In the figure below the results from the left layer system of the DCS are presented.

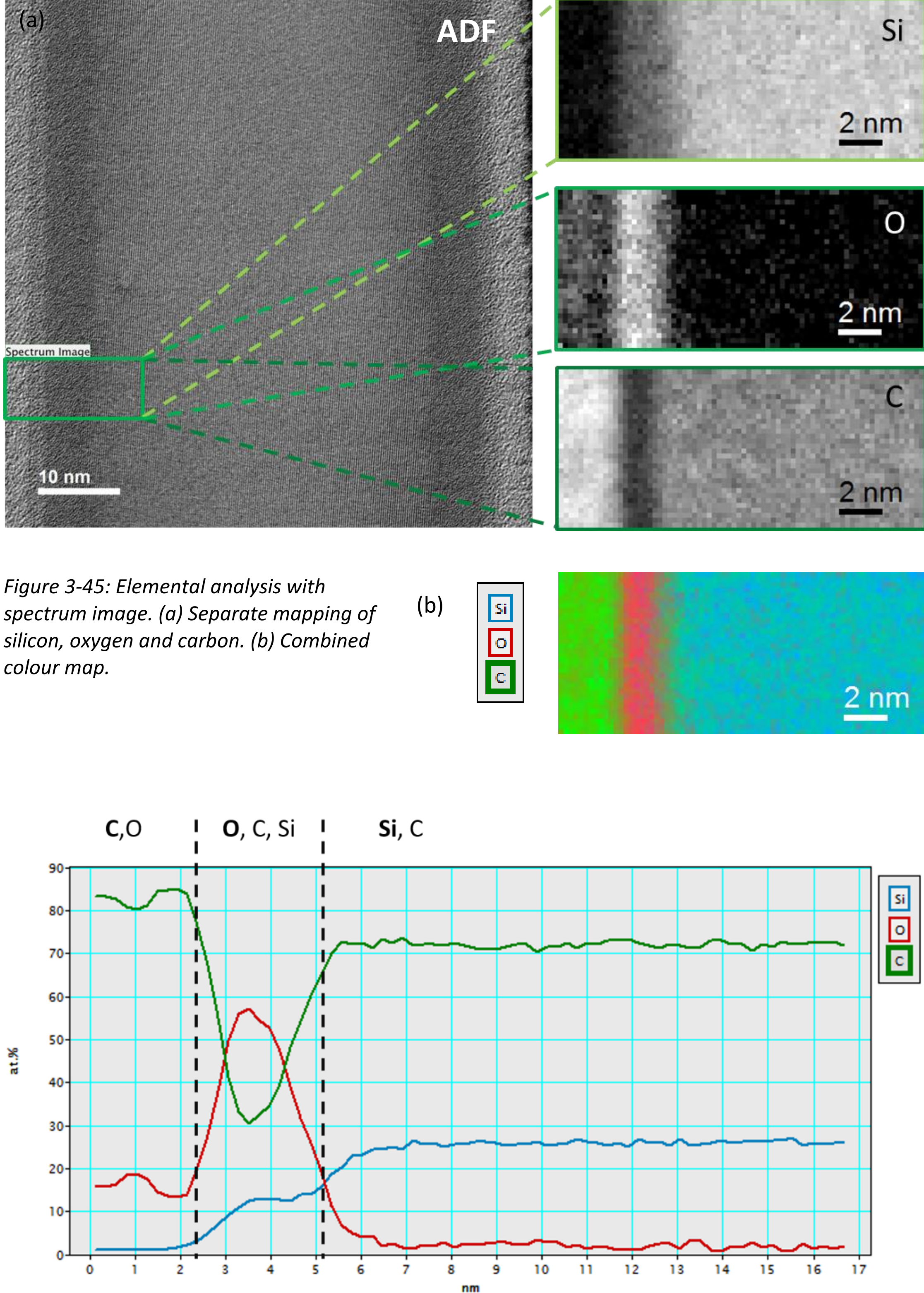

Figure 3-45: Elemental analysis with spectrum image. (a) Separate mapping of silicon, oxygen and carbon. (b) Combined colour map.

Figure 3-46: Quantified profile of elemental content in outer layers.

The outermost layer, with a thickness of about 4.5 nm mainly consists of C, traces of O but no Si, which implies a formation in the FIB during the DCS preparation. The 2 nm middle layer

shows all 3 elements. Because the oxygen content is highest it is likely that this layer forms due to oxidation, which likely occurs when the sample is exposed to air. The layer adjacent to the crystalline section has a size of 5 nm and contains only Si and C. Therefore, this amorphous layer is most likely generated by the milling process.

Experimental λ determination

With the obtained final thickness of 58 nm, the relative thickness value (0.35 MFP) from the SiC 2 lamella investigation and equation $\lambda = t/ln\left(\frac{I}{I_0}\right)$ a mean free path of λ_{sic} = 165.7 nm. This experimental value differs less than 2 % from the theoretical MFP.

3.8.1.5. Experimental MFP determination with SiC needle

As described in the theoretical part (see Section 2.5.1.2) the MFP can be determined with an experiment with a sample of known thickness. It is important to point out again, that the mean free path depends not only on the material, but also on the used microscope parameters. All following measurement are performed in the Titan with an acceleration voltage of 300 keV and a collection angle β = 25 mrad.

Imaging Parameters of TEM Titan

Acceleration voltage E_0	300 keV
Collection semi angle β	25 mrad
C2 aperture	200 µm
Theoretical MFP of SiC	136.7 nm

Experiment

An EELS spectrum image of a needle, i.e. a circular symmetric TEM sample, consisting of polycrystalline silicon (1), silicon oxide (2) and silicon carbide (3) (Figure 3-47 (a)) is recorded and used to create a t/ λ map. This relative thickness map (Figure 3-47 (b)) needs to be aligned (c) and cut (d) for the reconstruction (see Figure 3-48). It is important to point out, that only the SiC data (darker, right side) of the map is considered for the relative thickness determination.

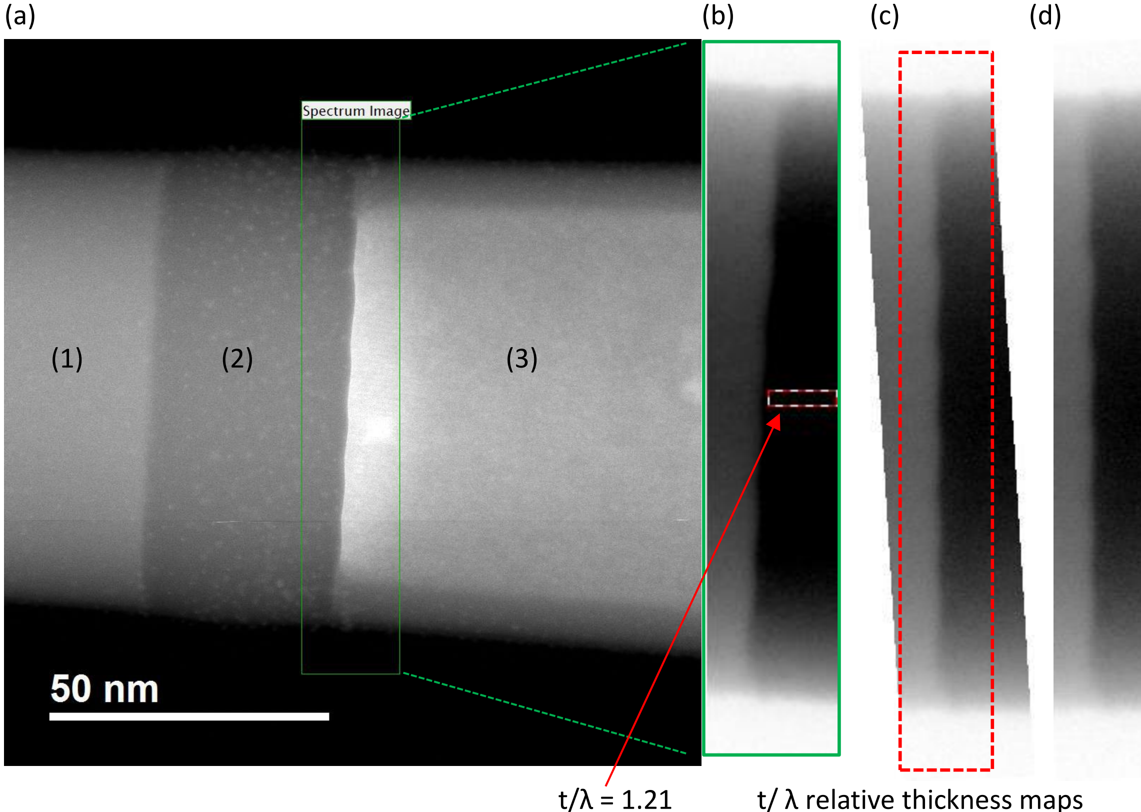

Figure 3-47: (a) Shows a needle consisting of polycrystalline silicon (1), silicon oxide SiO (2) and SiC (3), which is the material of interest. (b)-(d) t/λ relative thickness maps.

Analysis

In Figure 3-47 (a) the width of the needle can be measured, which corresponds to the diameter of the needle (about 170 nm). From that a first estimation of the MFP can be done, with the relative thickness value t/λ = 1.21 obtained from the selected area shown in Figure 3-47 (b). The measurement area is placed in the centre of the needle where the thickness is supposed to be 170 nm. The MFP can be calculated in accordance with: $\lambda = t/ln\left(\frac{I}{I_0}\right) = 170/1.21 = 140.5\ nm.$

A tomographic reconstruction from HAADF STEM images (Fig. 3-49) confirms that the SiC needle is in fact circular symmetric. Therefore, a reconstruction of the t/λ map (see Figure 3-47 (d)) can be done from a single map and can be used to acquire details about the radial distribution of t/λ of a sample. Normally for a tomographic reconstruction, a tilt series is required. However, the projection of the needle at every tilt angle looks the same due to the circular symmetry. With this simplification, a reconstruction from only one t/λ map is possible. The reconstructed needle corresponds to an image stack, in which every voxel (volume pixel) contains a t/λ value. In Figure 3-49 one slice through the reconstruction of the SiC section can be seen.

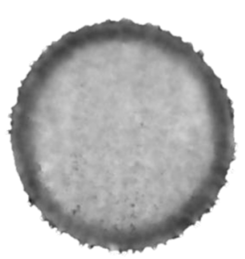

Figure 3-48: Reconstruction of cross section of the SiC needle.

In comparison to the previous approach, where the measured diameter was used to calculate the mean free path, this approach has the advantage that only a specific region of the reconstruction can be used as measurement area, as for the MFP measurements only crystalline regions should be considered. However, during the FIB preparation an amorphous layer and gallium implantation on the needle surface forms. In the HAADF STEM reconstruction in Figure 3-48 and in the MFP reconstruction (Figure 3-49) the brighter crystalline centre can clearly be distinguished from the about 16 nm thick darker amorphous outer shell. The bumps on the outmost surface are likely to be gallium ion implantation.

The peak in the centre and the ring structure in the crystalline part are artefacts from the reconstruction, which occurs because only one t/λ map is used.

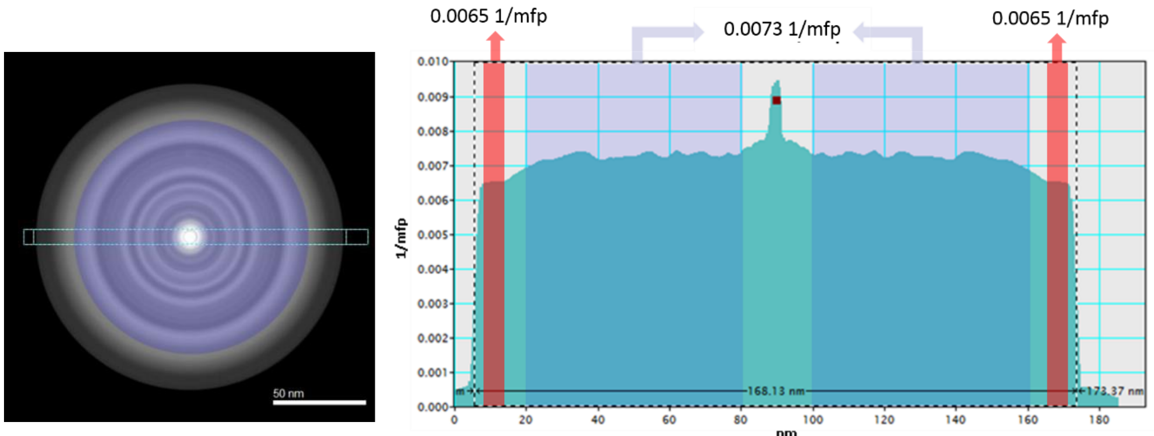

Figure 3-49: (a) Slice of reconstruction of t/λ map showing the relative thickness in the unit 1/MFP. (b) The profile through the needle (measuring window seen in (a)) in the unit 1/MFP. The blue area is used for the crystalline, the red for the amorphous mean free path calculation.

With the value 0.0073 1/MFP achieved from the crystalline section of the reconstruction above a MFP of 137 nm can be calculated. This experimental MFP is consistent with the theory, which results in λ^{7}_{sic}= 136.7 nm.

Furthermore the mean free path of the outer amourphous layer (1/MFP = 0.0065) can be determined: $\lambda_{sic,a}$= 154 nm. The MFP of the crystalline and the amorphous section of SiC differ about 11%. Due to the much thinner amorphous layers of the incestigated lamellae the difference in the mean free path can be neglected.

[7] λ_{sic} = 136.7 nm. Titan (E_0= 300 keV, β = 25 mrad)

3.8.2. Lead zirconate titanate

General information

The elements Pb, Zr, Ti and O are the compounds of lead zirconate titanate (PZT). This ceramic shows piezo-, pyro- and ferroelectric properties, which are required in micromechanics. Therefore, PZT is implemented in sensors, actuators and other electronic devices [29]. The crystal structure is a modified face-centred cubic (fcc) lattice. The oxygen atoms are positioned in the faces of the cubic system while the lead atoms are situated at the corner sites. In the centre of the unit cell an additional site occupied either by titan or zirconium occurs [30].

Lamella position for sputter rate determination

In the first approach 2 samples are prepared. However, due to the brittle behaviour of the ceramic, the first one broke during the first milling step, which makes an analysis impossible. The second lamella broke during the sputter rate determination procedure. Therefore, a third lamella is used for thickness verification via DCS.

All samples are fixed on separate grids in flag-position as already demonstrated for SiC in Figure 3-33.

Examination after FIB preparation to specify the starting condition for the NanoMill® post-treatment

The three samples hereinafter referred to by the abbreviations PTZ 1, PTZ 2 and PTZ 3 show different starting thicknesses as listed below.

	PZT 1	PZT 2	PZT 3
Relative starting thickness	0.46 MFP	0.65 MFP	0.9 MFP

3.8.2.1. Repetitive thinning with NanoMill® and monitoring with TEM CM20

During the first milling step **PZT 1** lamella broke right after the weld and therefore could not be used for the sputter rate determination. Consequently, **PZT 2** is used for the sputter rate determination and furthermore, **PZT 3** is employed to verify this results.

With **PZT 2** 6 iterations of thickness reduction in the NanoMill® (5 x 10 min per side, 1 x 10 min one side) and consecutive thickness determination with the CM20 are performed. During the 6th milling step the lamella is not visible any more in the NanoMill® live view. Investigation in the CM20 confirms that the lamella of PZT 2 broke during the last sputter treatment.

PZT 3 is employed the verify the sputter rate (obtained with PZT2) by a single milling step. Therefore, the thickness at the begining is measured with the CM20 and by just one sputter treatment in the NanoMill® a specified end thickness should be achieved.

	PZT 1	PZT 2	PZT 3
Iterations	1	6	1
Total milling time	20 min	110 min	240 min

Measuring thickness at certain areas of PZT 2

The areas 1 to 3 (see Figure 3-50) are utilized for the sputter rate determination measurement. The two smaller measurement windows (Area 1 and 2) have a size of 0.23 x 0.23 μm^2. The rectangular measurement widow (Area 3) is 0.31 x 1.43 μm^2 big.

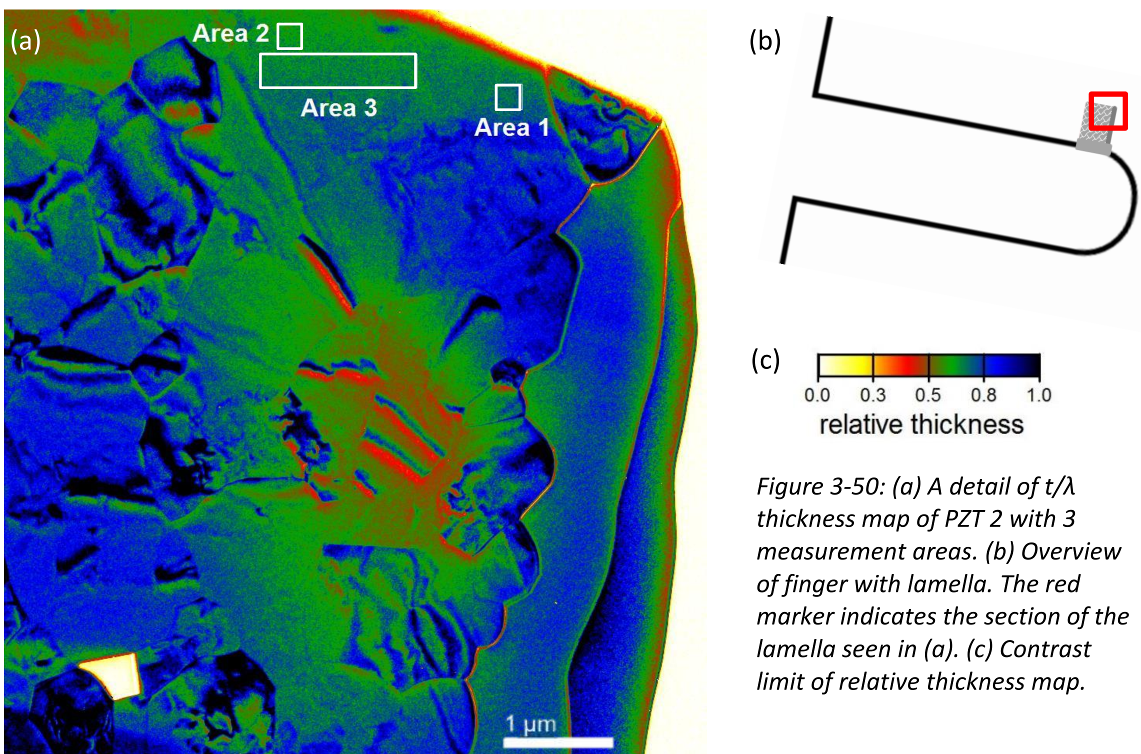

Figure 3-50: (a) A detail of t/λ thickness map of PZT 2 with 3 measurement areas. (b) Overview of finger with lamella. The red marker indicates the section of the lamella seen in (a). (c) Contrast limit of relative thickness map.

Though 6 iterations are performed with PZT 2 it is not possible to find areas without diffraction contours, with minimum size, in all of them. Therefore, the thickness of area 1 to 3 is only determined in t/λ maps of three sputter steps. The acquired relative and absolute thickness values are listed in the tables below.

Relative and absolute thickness

Table 3-7: Relative and absolute[8] thickness of PZT 2 Area 1, 2 and 3.

s… sputter time / min

r… relative thickness / MFP

t… absolute thickness / nm

	Area 1	Area 2	Area 3	Area 1	Area 2	Area 3
s/min	r/MFP	r/MFP	r/MFP	t/nm	t/nm	t/nm
0	0.67 ± 0.03	0.62 ± 0.03	0.65 ± 0.03	84 ± 3	77 ± 3	81 ± 4
20	0.66 ± 0.02	0.61 ± 0.02	0.63 ± 0.02	83 ± 2	76 ± 2	78 ± 2
60	0.56 ± 0.02	0.52 ± 0.02	0.54 ± 0.02	70 ± 2	65 ± 2	68 ±3

3.8.2.2. Sputter rate determination

The thickness data in Table 3-7 above can be plotted against the milling time (see Figure 3-51) to obtain the sputter rate of lead zirconate titanate.

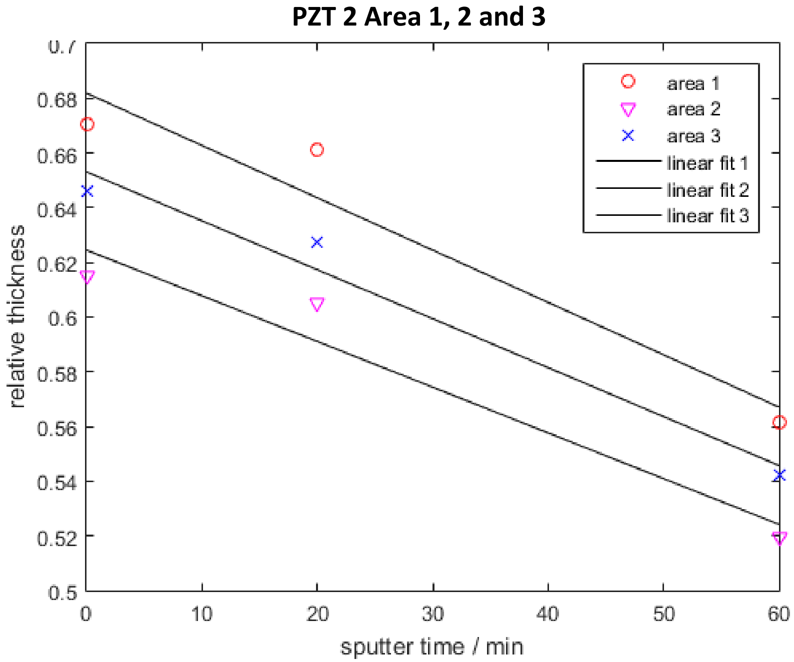

Figure 3-51: Relative thickness reduction vs. milling time of PZT 2.

Again, the mean sputter rate is given in the three most common units (see Table 3-9).

[8] λ_{PZT} = 125 nm CM20 (E_0= 200 keV, β = 3.63 mrad)

Table 3-8: Sputter rate of Area 1,2 and 3 of PZT 2

Area	Sputter rate MFP/min	Sputter rate Å/min
1	$(1.9 \pm 0.5)\ 10^{-3}$	2.4 ± 0.1
2	$(1.7 \pm 0.3)\ 10^{-3}$	2.1 ± 0.1
3	$(1.8 \pm 0.2)\ 10^{-3}$	2.3 ± 0.1

Table 3-9: Mean sputter rate

Mean sputter rate	
$(1.7 \pm 0.5)\ 10^{-3}$	MFP/min
2.3 ± 0.1	Å/min
14 ± 1	nm/h

3.8.2.3. Confirmation of sputter rate

To test the obtained sputter rate of lead zirconate titanate a lamella with known starting thickness is milled to a relative thickness of 0.5 MFP in one milling step. According to the results of PZT 2 for the same milling conditions, a total milling time of 240 min (120 min per side) is necessary to receive a thickness reduction from 0.9 to 0.5 MFP.

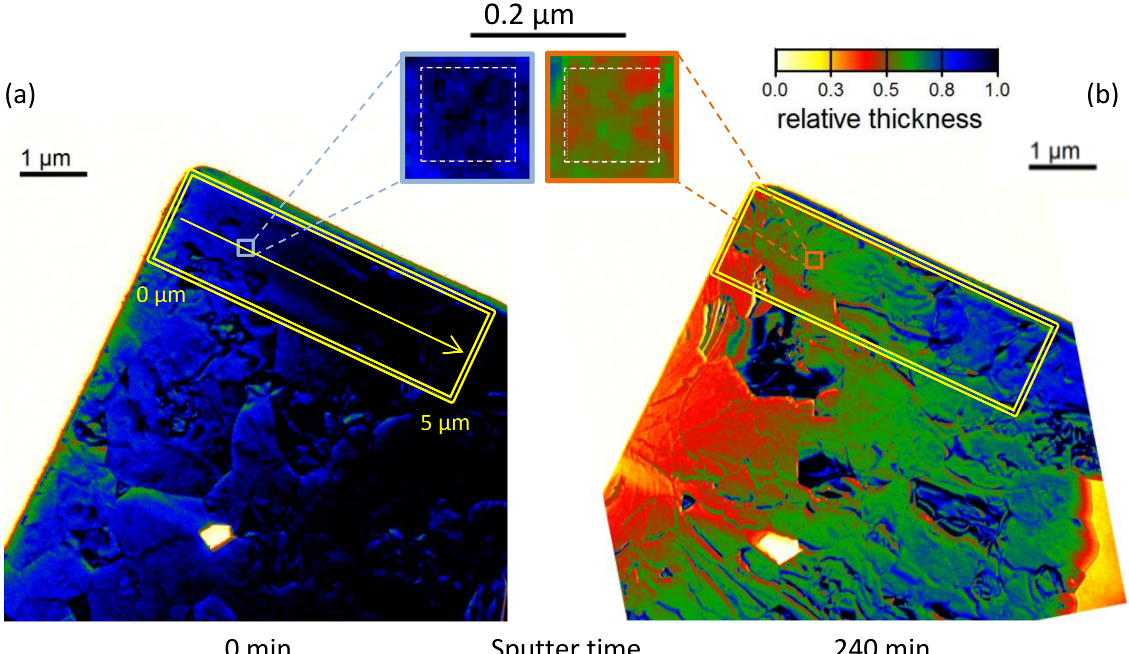

Figure 3-52: t/λ maps of PZT 3 (a) After FIB (0 min sputter time in NanoMill®). (b) After 240 min in the NanoMill®.

The inserts (blue, orange) in the figure above show the measurement windows for the sputter rate confirmation. The data can be seen in the tables below. The line profile (combined with a averaging of about 1 µm vertical to the line profile) is marked with the yellow double line (direction of the profile is indicated by yellow arrow) and can be seen in Figure 3-53 below.

Table 3-10: Relative and absolute thickness of PZT 3
s… sputter time
r… relative thickness / MFP
t… absolute thickness / nm
σ… standard deviation / MFP respectively nm

	Relative thickness	**Absolute thickness**[9]
s/min	r/MFP	t/nm
0	0.92 ± 0.03	115 ± 4
240	0.51 ± 0.03	64 ± 4

Table 3-11: Sputter rate

Sputter rate	
$(1.7 \pm 0,1)\ 10^{-3}$	MFP/min
2.1 ± 0.1	Å/min
13 ± 1	nm/h

Figure 3-53 shows the relative thickness reduction for a larger area of PZT 3. The thickness reduction distributes evenly over the measurement area.

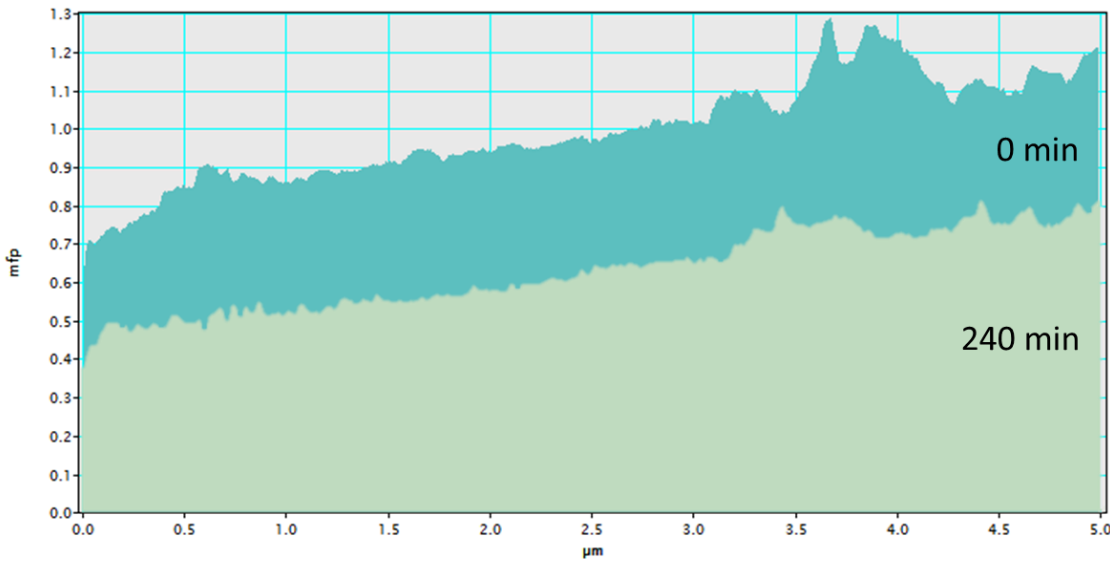

Figure 3-53: Profiles from two rectangle (yellow) measurement areas in Figure 3-52.

By subtracting the two profiles and dividing by the total sputter time of 240 min the sputter rate of $(1.5 \pm 0.2)\ 10^{-3}$ MFP per minute can be calculated. Considering the standard deviation this result, shown in Figure 3-54, match the sputter rate of the small measurement area listed in Table 3-11.

[9] λ_{PZT} = 125 nm CM20 (E_0= 200 keV, β = 3.63 mrad)

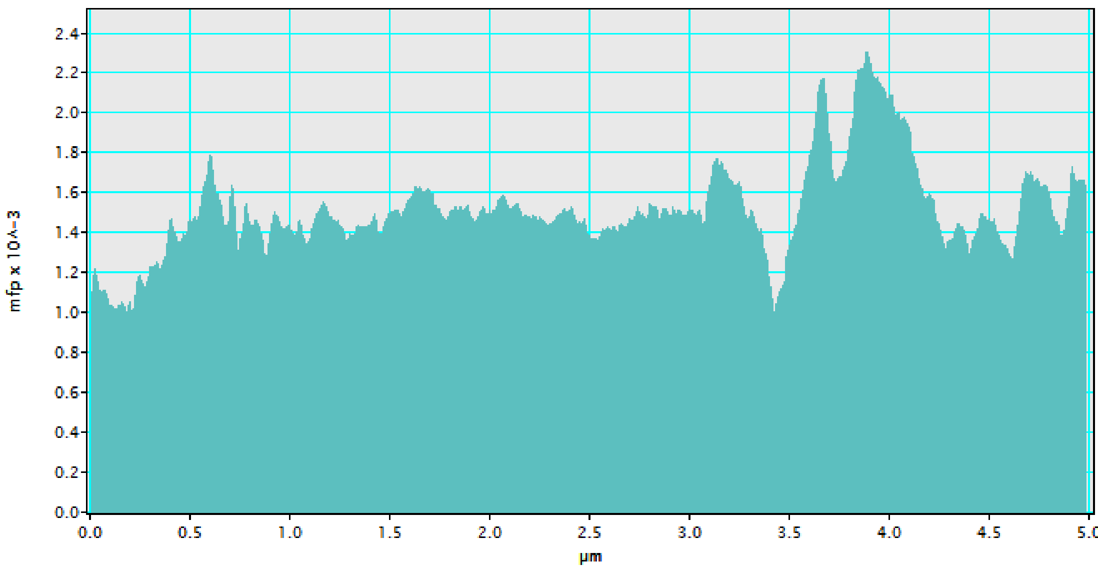

Figure 3-54: Sputter rate of in MFP per minute.

The unevenness of the obtained sputter rate corresponds to the nature (grain structure) of PZT and randomly appearing diffraction contours.

3.8.2.4. Double Cross Section of PZT 3

To determine the thickness of the PZT 3 lamella a DCS is prepared. The images in Figure 3-55 below should validate that the thickness is measured in the same area. With the relative thickness information of the t/λ method the mean free path can be calculated.

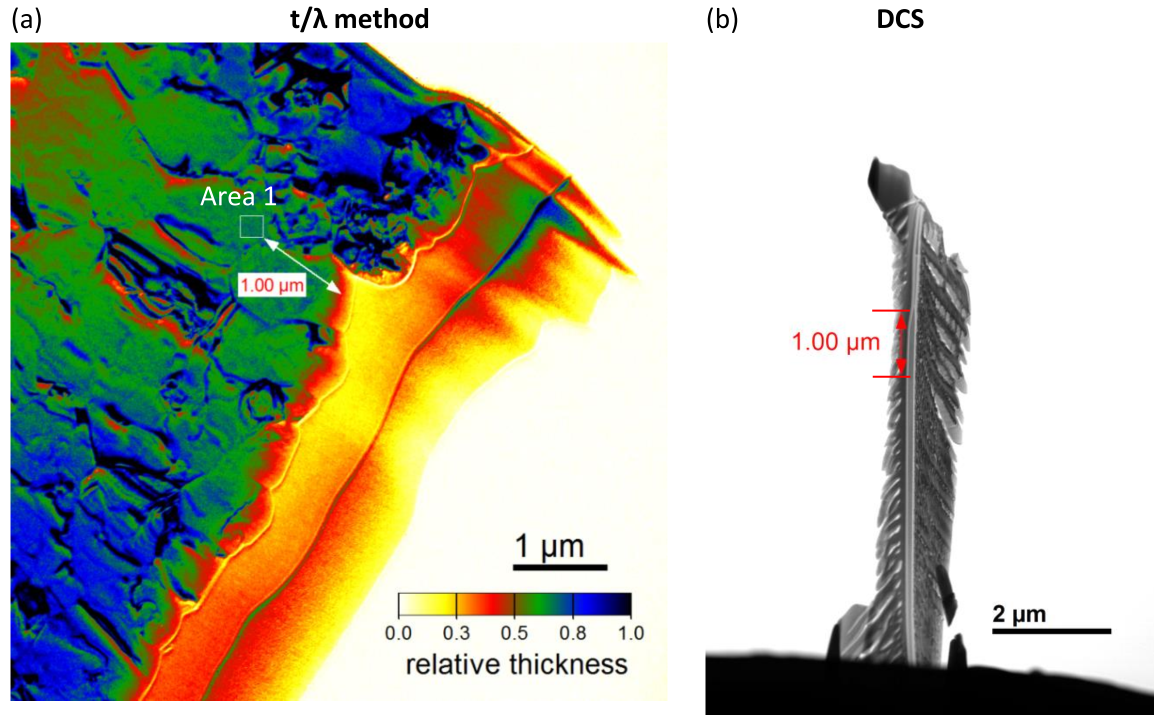

Figure 3-55: (a) PZT 3 after 240 min NanoMill® treatment. Window Size: 0.23 x 0.23 µm. (b) DCS of PZT 3.

Table 3-12 shows the relative thickness of the lead zirconate titanate lamella after the one step milling procedure.

t/λ method

Table 3-12: Relative thickness of PZT 3 Area 1.

Relative thickness
r /MFP
0.66 ± 0.02

Table 3-13: Absolute[10] thickness of PZT 3 Area 1.

Absolute thickness
t / nm
83 ± 3

DCS

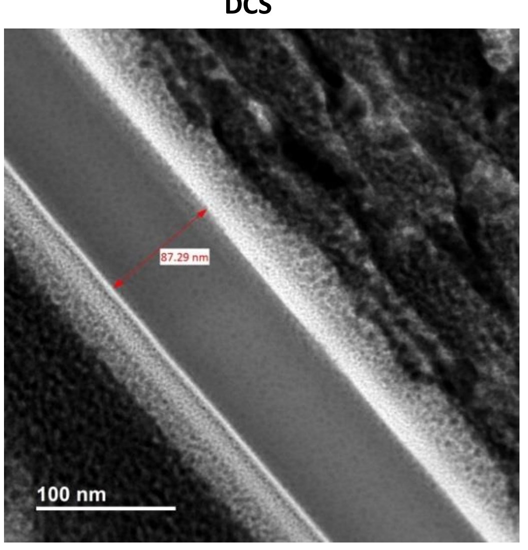

Figure 3-56: Absolute thickness measurement of PZT 3.

Experimental λ determination

With the obtained thickness from the DCS of 87.3 nm, the relative thickness value (0.66 MFP) from the PZT 3 and equation $\lambda = t/ln\left(\frac{I}{I_0}\right)$ a mean free path of λ_{PZT} = 132.3 nm. This experimental value differs 5.5 % from the theoretical MFP.

[10] λ_{PZT} = 125 nm CM20 (E_0= 200 keV, β = 3.63 mrad)

4. Conclusion

The main goal of this thesis is the determination of the sputter rate of silicon carbide and lead zirconate titanate with a given set of parameters for a treatment in a NanoMill® by Fischione. In addition, also the handling and special properties of the NanoMill® are main themes in this work.

The NanoMill® gives the opportunity of a fast and gentle post-treatment of FIB lamellae by low energy argon ion milling. An enhancement in TEM sample quality can be achieved with the NanoMill® by cleaning the surface and reducing preparation artefacts. For longer process times even the sample thickness can be reduced.

Iterative experiments have been performed to determine the milling rate of silicon carbide and lead zirconate titanate. Knowing the sputter rate of a material for a given set of parameters is crucial for the post-treatment with the NanoMill®.

Beside these experimental procedures the considerations of the geometry in the NanoMill® and the lamella position on the grid are crucial for an optimal post-treatment. Therefore, a closer look was taken at the TEM transfer grid dimensions and the alignment of the lamella on the finger to ensure the most advantageous setting. The outcome has been information on the best sample position and most favourable grid geometry. For obtaining the absolute sputter rate a closer look was taken onto experimental mean free path determination and thickness determination by double cross sectioning the TEM lamellae.

	Sputter rate nm/h
Silicon carbide	13 ± 1
Lead zirconate titanate	39 ± 2

It is crucial to point out, that the obtained sputter rates are only valid for the parameter set used in this thesis.

In conclusion, the findings about the geometry and the sputter rate of this work may lead to an optimized NanoMill® post-treatment for FIB prepared TEM lamellae.

Bibliography

[1] J. Ayache, L. Beaunier, J. Boumendil, G. Ehret, and D. Laub, *Sample Preparation Handbook for Transmission Electron Microscopy: Methodology*. Springer New York, 2010.

[2] D.B. Williams and C.B. Carter, *Transmission Electron Microscopy: A Textbook for Materials Science*. Springer US, 2009.

[3] J. Ayache, L. Beaunier, J. Boumendil, G. Ehret, and D. Laub, *Sample Preparation Handbook for Transmission Electron Microscopy: Techniques*. Springer New York, 2010.

[4] T. Schuhrke, M. Mandl, J. Zweck, and H. Hoffmann, 'Investigation of surface amorphization of Silicon wafers during ion-milling', *Ultramicroscopy*, vol. 41, p. 429, 1992.

[5] A. Barna, B. Pécz, and M. Menyhard, 'Amorphisation and surface morphology development at low-energy ion milling', *Ultramicroscopy*, vol. 70, no. 3, pp. 161–171, Jan. 1998.

[6] J.P. McCaffrey, M.W. Phaneuf, and L.D. Madsen, 'Surface damage formation during ion-beam thinning of samples for transmission electron microscopy', *Ultramicroscopy*, vol. 87, no. 3, pp. 97–104, Apr. 2001.

[7] Fischione Instruments, Ed., 'NanoMill® TEM Specimen Preparation System - Instruction Manual'. 2012.

[8] G. Brown, *The Physics and Technology of Ion Sources*, Second, Revised and Extended Edition. WILEY-VCH, 2004.

[9] Kimball Physics Inc., 'Yttria-Coated Iridium Cathods'. Jun-2016.

[10] Petrignani, A., van der Zande, J.W., Cosby, P.C., Hellberg, F., Thomas, R.D., and Larsson, M., 'Vibrationally resolved rate coefficients and branching fractions in the dissociative recombination of O2+', *J. Chem. Phys.*, vol. 122, no. 14302, 2005.

[11] El-Kareh, B., *Fundamentals of Semiconductor Processing Technology*. 1995.

[12] S. Ghalab, 'Metal Cluster Sputtering under reactive Ion Bombardment investigated by TOF-SNMS-Laser-System', 2005.

[13] R. Behrisch, *Sputtering by Particle Bombardment I*. Springer-Verlag Berlin, 1981.

[14] M.J. Süess, E. Mueller, and R. Wepf, 'Minimization of amorphous layer in Ar+ ion milling for UHR-EM', *Ultramicroscopy*, vol. 111, no. 8, pp. 1224–1232, Jul. 2011.

[15] K.M. Rabe, C.H. Ahn, and J. Triscone, *Physics of Ferroelectrics: A Modern Perspective*. Springer Berlin, 2007.

[16] Y. Wang, W. Chen, B. Wang, and Y. Theng, 'Ultrathin Ferroelectric Films: Growth, Characterization, Physics and Applications', *Materials*, vol. 7, Sep. 2014.

[17] K. Iakoubovskii, K. Mitsuishi, Y. Nakayama, and K. Furuya, 'Thickness measurements with electron energy loss spectroscopy', *Microsc Res Tech*, vol. 71, pp. 626–631, Aug. 2008.

[18] R.F. Egerton, *Electron energy-loss spectroscopy in the electron microscope*. New York: Plenum Press, 1986.

[19] T. Ghosh, M. Bardhan, M. Bhattacharya, and B. Satpati, 'Study of inelastic mean free path of metal nanostructures using energy filtered transmission electron microscopy imaging', *J. Microsc.*, Mar. 2015.

[20] Gatan, Inc., 'DigitalMicrograph EELS Analysis User's Guide'. May-2002.

[21] R.F. Egerton and S. C. Cheng, 'Measurement of local thickness by electron energy-loss spectroscopy', *Ultramicroscopy*, vol. 21, no. 3, pp. 231–244, Jan. 1987.

[22] Enabling Science and Technology through and European Electron Microscopy, 'Double Cross section of FIB prepared semiconductor samples'. 2012.

[23] FELMI ZFE, 'TEM "double cross section" (Grid 3mm, lamella 5x10µm)', Jun-2015. [Online]. Available: https://www.youtube.com/watch?v=jy07QT4EmTA.

[24] Fischione Instruments, Inc., 'Model 1040 NanoMill ® TEM specimen preparation system - Specimen configuration'. Jul-2012.

[25] E. Montoya, S. Bals, M.D. Rossell, D. Schreyvers, and G. van Tendeloo, 'Evaluation of Top, Angle, and Side Cleaned FIB Samples for TEM Analysis', *Microsc. Res. Tech.*, vol. 70, pp. 1060–1071, 2007.

[26] Semicore Equipment, Inc., 'Sputter yield reference'. [Online]. Available: http://www.semicore.com/reference/sputtering-yields-reference. [Accessed: 26-Nov-2015].

[27] SPECS Surface Analysis and Computer Technology, 'Useful Information and Facts about the Practice of Sputtering'. [Online]. Available: http://www.specs.de/cms/upload/PDFs/IQE11-35/sputter-info.pdf. [Accessed: 26-Nov-2015].

[28] W.Y. Ching, Y. Xu-N, P. Rulis, and L. Ouyang, 'The Eletronic Structure and Spectroscopic properties of 3C, 2H, 4H, 6H, 15R and 21R polymorphs of SiC', *Mater. Sci. Eng.*, vol. 422, pp. 147–156, Apr. 2006.

[29] R. Strobel, 'Einmal Hightech bleifrei, bitte', *ZEIT ONLINE*, Nov. 2009.

[30] P.M. Martin, 'Physics of Thin Films: Piezoelectric and Ferroelectric Properties', *Vac. Technol. Coat.*, Apr. 2012.